Ceramics	Electron Optics
Education	**MRC**	Materials Liaison Program
Mechanical Behavior	Polymers

FINAL REPORT

GRAIN BOUNDARY CHEMISTRY AND CREEP RESISTANCE OF ALUMINA

Professors M.P. Harmer (P.I.), H.M. Chan (Co-P.I.), J.M. Rickman (Co-P.I.), and Research Assistants/Associates C.M. Wang, J. Cho and M. Drahus

20011003 049

Materials Research Center, MRC
Lehigh University

REPORT DOCUMENTATION PAGE

AFRL-SR-BL-TR-01-

0478

1. AGENCY USE ONLY *(Leave blank)*	2. REPORT DATE	3. REPORT TYPE AND DATES COVERED
	8/10/01	Final Report: 9/1/99 – 3/31/01

4. TITLE AND SUBTITLE	5. FUNDING NUMBERS
Grain Boundary Chemistry and Creep Resistance of Alumina	

6. AUTHOR(S)

Martin P. Harmer
Helen M. Chan
Jeffrey M. Rickman

7. PERFORMING ORGANIZATION NAME(S) AND ADDRESS(ES)	8. PERFORMING ORGANIZATION REPORT NUMBER
Materials Research Center Lehigh University 5 East Packer Avenue Bethlehem, PA 18015-3194	

9. SPONSORING/MONITORING AGENCY NAME(S) AND ADDRESS(ES)	10. SPONSORING/MONITORING AGENCY REPORT NUMBER
Dr. Joan Fuller Air Force Office of Scientific Research 801 North Randolph Street, Room 732 Arlington, VA 22203-1977	F49620-98-1-0117

11. SUPPLEMENTARY NOTES

12a. DISTRIBUTION/AVAILABILITY STATEMENT	12b. DISTRIBUTION CODE
Approved for public release; distribution unlimited.	

13. ABSTRACT *(Maximum 200 words)*

(See attached)

14. SUBJECT TERMS

Keywords: creep, segregation, alumina, EBKD, computer simulation

15. NUMBER OF PAGES
16. Price code

17. SECURITY CLASSIFICATION OF REPORT	18. SECURITY CLASSIFICATION OF THIS PAGE	19. SECURITY CLASSIFICATION OF ABSTRACT	20. LIMITATION OF ABSTRACT
Unclassified	Unclassified	Unclassified	Unlimited

Standard Form 298 (Rev. 2-89)

1. PROGRESS SUMMARY

The Lehigh group has pioneered work on the role of segregating rare earth dopants on the grain boundary structure and tensile creep behavior of alumina. In an attempt to clarify the exact mechanism that controls creep behavior of the doped aluminas, various advanced characterization techniques have been applied including: secondary ion mass spectrometry (SIMS), scanning transmission electron microscopy (STEM), orientation image microscopy (OIM), x-ray absorption studies which include x-ray absorption near edge structure (XANES) and extended x-ray absorption fine structure (EXAFS), and atomistic computer simulation and studies of the creep kinetics. Combined use of high resolution STEM and EXAFS allowed the determination of the dopant grain boundary segregation behavior and the atomic structural environment around the grain boundary segregated dopant ions.

Based on the information obtained, it is postulated that the most logical explanation for the increased creep resistance is that the oversized dopant ions segregate to more energetically favorable grain boundary sites, and block a few critical diffusive pathways. It is also found that creep rates were not influenced by the presence of second phase precipitates, verifying that the creep improvement is a solid solution effect. This mechanism is sufficiently general that it may be applicable to other ceramic systems. In addition, co-doping with ions of disparate sizes resulted in even further enhancement of the creep resistance. Further, model experiments involving co-doping with Fe have been devised which will directly compare the effectiveness of the other dopant ion on the inhibition of transport either along, or away from the alumina grain boundaries.

Based on Lehigh group's findings, **3M** Company has developed a new-generation alumina fiber (Nextel 650), codoped with both Y and Zr, with creep resistance far superior to what was previously attainable (Figure 1).
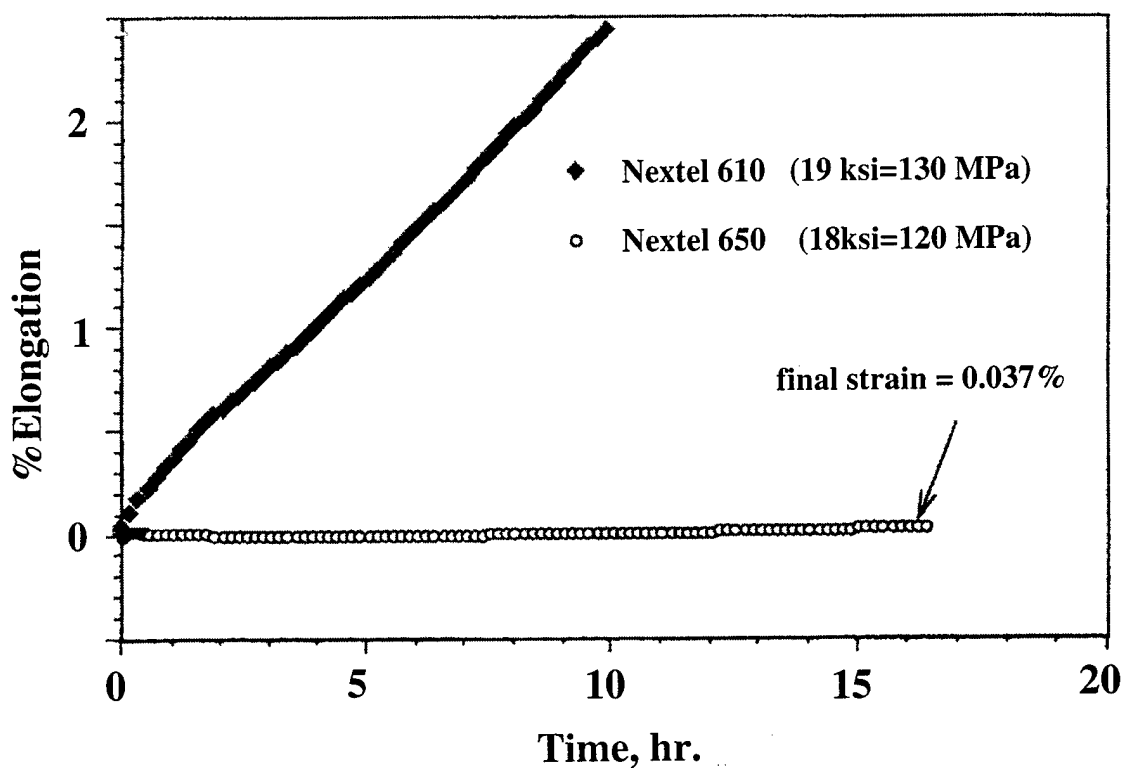
Fig. 1 Comparison of the elongation as a function of time for Nextel 610 fiber (traditional) and Nextel 650 fiber (doped with 1wt % of Y) during creep testing at 1100°C (Courtesy of D. M. Wilson and also see ref.: D. M. Wilson and L. R. Visser, "Nextel 650 Ceramic Oxide Fiber: New Alumina-Based Fiber for High Temperature Composite Reinforcement," *The 24th Annual Conf. Eng. Ceram. and Structures Cocoa Beach, FL 2000.*)

2. ACCOMPLISHMENTS

a) Atomic structural environment around grain boundary segregants

Using EXAFS, the Lehigh group was the first to establish the atomic structural environment around the grain boundary segregated Y and Zr in alumina. It has been found that Y and Zr at 100 ppm concentration in α-Al_2O_3 occupy grain boundary sites with well defined nearest neighbor cation-oxygen bond lengths, which are similar to those in their parent oxides. However, the next nearest neighbor cation-cation distances varied considerably from site to site. The dopant (Y, Zr)-O nearest neighbor coordination number was determined to be ~ 30% smaller than that in their parent oxides.

b) Dopant grain boundary segregation behavior

By using high resolution scanning transmission electron microscopy (HRSTEM), the Lehigh group has established that the increasing occupation of α-Al_2O_3 grain boundaries by Y is characterized by three compositional regimes: dilute, saturated, supersaturated, and equilibrium with YAG precipitates. The grain boundary Y equilibrium concentration corresponds to Y grain boundary excess of ~ 3 Y atoms/nm^2, and a supersaturation concentration of ~ 5 Y atoms/nm^2. Also, it has been observed that supersaturation of the grain boundary with dopant seems to lead to some anomalous properties of grain boundary related phenomena. This aspect of the dopant effect is currently under study.

c) Interplay of grain boundary structure and chemistry

HRSTEM and EXAFS measurements indicate that as the grain boundary Y concentration increases gradually from dilute to saturated and finally to supersaturated, the most significant changes in the radial distribution function are the development of well

defined Y-cation peaks. Quantitative fitting of the Y-O shell reveals that accompanying the Y grain boundary supersaturation the Y-O nearest neighbor distance shows no substantial change, while the Y-O coordination number increases. Quantitative fitting of the Y-cation shell gives an Y-cation distance of 3.31 Å. The fitted Y-cation distance is approximately equal to the average Y-Al distance when Y substitutes for Al in α-Al_2O_3 while relaxing the Y-O distance to that in Y_2O_3 and keeping the O-Al distance the same as that in α-Al_2O_3. These observations suggest that the Y grain boundary supersaturation leads to an increased fraction of Y occupying near-boundary substitutional sites in α-Al_2O_3.

Structurally, the Y supersaturated grain boundary is postulated to consist of three layers, a core layer within which the local structural environment around Y is dominated by short range ordering (nearest neighbor shell ordering), and two near-boundary layers within which the Y ions are in substitutional sites.

d) Computer modeling and simulation

The volumes associated with several special grain boundaries in alumina were characterized by a spatially local Voronoi construction in order to identify potential sites for impurity segregation. It has been found that in the case of substitutional sites in a $\Sigma 3$ boundary the degenerate, unimodal size distribution which occurs in the bulk lattice, is replaced by an essentially bimodal distribution of sites with widely disparate sizes. Further, approximately 1/3 of the boundary interstitial sites are larger than these bulk sites. In the case of a $\Sigma 13$ boundary, it has been found that several potential substitutional sites, many larger than the corresponding bulk sites, are available for segregation. A similar situation was found for interstitial sites. These results are consistent with recent experimental evidence suggesting that selective co-doping may provide a more efficient means of filling available space near boundaries, thereby further enhancing creep resistance.

3. PROGRESS REPORTS

3.1   Atomic Structural Environment of Grain Boundary Segregated Y and Zr in Creep Resistant Alumina from EXAFS

By

C. M. Wang, G. S. Cargill III, M. P. Harmer,
H. M. Chan, and J. Cho

PII: S1359-6454(99)00210-4

PERGAMON

ATOMIC STRUCTURAL ENVIRONMENT OF GRAIN BOUNDARY SEGREGATED Y AND Zr IN CREEP RESISTANT ALUMINA FROM EXAFS

C. M. WANG, G. S. CARGILL III, M. P. HARMER†, H. M. CHAN and J. CHO

Materials Research Center, Lehigh University, Bethlehem, PA 18015, U.S.A.

Abstract—Dopants Y and Zr at 100 p.p.m. level (Y or Zr to Al atomic ratio) in ultra-high purity polycrystalline alumina have been found to be mainly segregated to the alumina grain boundaries. The atomic structural environments around the Y and Zr segregants have been investigated by Extended X-ray Absorption Fine Structure (EXAFS). On average, Y ions in α-Al_2O_3 grain boundaries are coordinated by four oxygens, at a distance of 2.30 Å, which corresponds nearly to the Y–O bond length in cubic Y_2O_3, and Zr ions are coordinated by five oxygens at a distance of 2.14 Å, which is approximately the same as the average Zr–O bond length in monoclinic ZrO_2. However, in the EXAFS radial distribution function, the Y-cation and Zr-cation next nearest neighbor shell cannot be clearly identified. These results suggest that Y and Zr at 100 p.p.m. concentrations in α-Al_2O_3 occupy grain boundary sites with well defined nearest neighbor cation–oxygen bond lengths similar to those in their parent oxides but with the next nearest neighbor cation–cation distances varying considerably from site to site. From EXAFS, the Y grain boundary saturation concentration is estimated to be 6.0 atoms/nm^2, which is consistent with the estimate from STEM of 4.4 atoms/nm^2. The differences in the Zr–O and Y–O nearest neighbor distances and coordination numbers in Al_2O_3 grain boundaries are related to the Y–Al and Zr–Al size mismatches. © *1999 Acta Metallurgica Inc. Published by Elsevier Science Ltd. All rights reserved.*

Keywords: EXAFS; Alumina; Grain boundary segregation; Atomic structure; Y and Zr

1. INTRODUCTION

Dopant and impurity grain boundary segregation has been found in both metals and ceramics [1–4]. The grain boundary segregants may have either detrimental or beneficial effects on a material's microstructures and properties. An example of the detrimental aspects of grain boundary segregation is segregation-induced intergranular fracture embrittlement [5]. Beneficial effects of dopant segregation on material properties have been recently demonstrated in two systems. Doping superalloys with a trace amount of Y significantly improves their oxidation resistance [6]. Recently, it has been also systematically established that doping trace amounts of rare-earth oxide (typically 100–1000 p.p.m.) in high purity alumina induces a two to three orders of magnitude increase in the creep resistance [7–10]. A better understanding of the mechanisms by which such impurities influence material properties is the key to further exploiting these effects and for optimizing material properties.

Many efforts have been made over the last few years to correlate microstructural features with properties of rare earth doped high purity alumina. Based on transmission electron microscopy (TEM)

studies of grain boundaries in doped alumina specimens, Lartigue *et al.* [11] postulated that the role of the dopant ions was to modify the grain boundary structure in a manner so as to impede the accommodation of lattice dislocations, and hence limit grain boundary sliding. However, a recent study by Cho *et al.* [12] using Orientation Image Mapping (OIM) found no obvious difference in the distribution of the grain boundary types between undoped and doped alumina. The conclusion of Cho *et al.* is also consistent with a recent TEM survey of grain boundary type distribution in Y-doped alumina [13], where very few special boundary types were found. By using secondary ion mass spectroscopy (SIMS) mapping, Thompson *et al.* [3] have shown that Y and La dopants are segregated to all types of alumina grain boundaries. Motivated by those observations, the same group has proposed that the increased creep resistance in doped alumina be attributed to reduced grain boundary diffusivity caused by blocking of grain boundaries by the segregated oversized dopants [9, 14]. Further evidence in support of this grain boundary blocking model is as follows. (1) The same improvement in creep resistance was observed for dopant levels both above and below the solubility limit, confirming that the phenomenon is a solid solution effect [14]. (2) The creep resistance improvement shows dependence on

---

†To whom all correspondence should be addressed.

the ionic size of the dopant [14]. However, the structural details of the grain boundary with the segregated dopant remain to be established, both theoretically and experimentally. This information is needed for further understanding of the mechanisms by which segregation affects grain boundary related phenomena.

A variety of microscopic and spectroscopic methods have been employed to investigate the structural environment of the grain boundary segregated dopant ions. These methods have included auger electron spectroscopy (AES) [15], X-ray photoelectron spectroscopy (XPS) [16], energy dispersive X-ray spectroscopy (EDS) in a scanning electron microscope (SEM) and in a scanning transmission electron microscope '(STEM) [17, 18], electron energy-loss spectroscopy (EELS), SIMS [3] and extended X-ray absorption fine structure (EXAFS) [19, 20]. AES, XPS, EDS and SIMS have been used mainly to investigate grain boundary segregation concentrations and segregant distribution profiles. STEM measurements by Bruley et al. [17] revealed that in the case of Y and La, the dopant ions were segregated to a narrow region at the alumina grain boundaries. Assuming a segregation layer thickness of ~1 nm, the fraction of cation sites occupied by the impurity ions was determined to be ~9–10%. Attempts also have been made using EELS to investigate the local chemical bonding around the dopant ions in 1000 p.p.m. Y_2O_3 and 500 p.p.m. La_2O_3 doped alumina [17]. The structures of alumina grain boundaries with Ca and Zr segregation have also been investigated using high resolution transmission electron microscopy (HRTEM) [21, 22].

EXAFS is a powerful method for determining the atomic structural environment around impurities, particularly very dilute impurities, and it has been used to probe the local atomic structural configurations around impurities in various oxides and non-oxides [23–25], including Y_2O_3 stabilized ZrO_2 and 300 p.p.m. to 1 mol% Y_2O_3 doped alumina [19, 20]. However, in an earlier study of Y_2O_3 doped Al_2O_3 [19], the Y_2O_3 concentration exceeded the solid solution limit of the α-Al_2O_3, so yttrium aluminum garnet ($Y_3Al_5O_{12}$, YAG), which precipitated as a secondary phase, masked the EXAFS signal from the grain boundary segregated Y ions. To obtain information about the structural environment of grain boundary segregated Y ions, measurements on more dilute yttrium doped alumina samples and more detailed data analysis were needed. Based on previous microscopic investigations, we have established for very dilute concentrations of doping, typically 100 p.p.m., that the Y and Zr ions are mainly segregated to the grain boundaries and that secondary phase precipitation is absent [14, 26]. In this paper, we report an EXAFS investigation of high purity alumina doped with Y_2O_3 at concentrations of 100 and 1000 p.p.m., and ZrO_2 at a nominal concentration of 100 p.p.m., giving information about the atomic structural environment of grain boundary segregated Y and Zr ions. Implications of the present results for the effects of the segregants on grain boundary mediated transport are discussed.

2. EXPERIMENTAL PROCEDURES

2.1. Materials

The samples were ultra-high purity Al_2O_3 doped with either Y_2O_3 or ZrO_2. Y_2O_3 was doped at two levels, 100 and 1000 p.p.m. (Y/Al atomic ratio, hereafter referred to as samples 100Y and 1000Y), and ZrO_2 at 100 p.p.m. nominally (Zr/Al atomic ratio, hereafter referred to as sample 100Zr). The doping process involves dispersing ultra-high purity alumina powder (Sumitomo AKP 53, with an average grain size of 0.3 μm, and purity of 99.995%) in methanol. Y-doping was achieved by adding an yttrium nitrate (99.999%, Aldrich Chemical Co.) methanol solution to the Al_2O_3 slurry. Zr-doping was achieved by ball milling the Al_2O_3 slurry with ZrO_2 grinding media (4.2 mol% Y_2O_3 stabilized tetragonal zirconia, Tosoh U.S.A. Inc., Bridgewater, NJ) for 20 h. All powder processing was conducted in a class 100 clean room environment using acid washed containers. All the doped powders were hot-pressed using graphite dies in vacuum at 45 MPa for 30 min. The hot-pressing temperature for the 100Y powder was 1450°C, for the 1000Y powder was 1475°C, and for the 100Zr powder was 1320°C. The 100Y and 1000Y samples have a relative density higher than 99%, and the 100Zr sample has a relative density of 97%. The 100Zr and 100Y samples show a rather uniform grain size distribution, with the 100Y having an average grain size of ~1.5 μm [Fig. 1(a)], and the 100Zr having an average grain size of ~0.5 μm [Fig. 1(b)]. SEM and TEM reveal no secondary phase precipitates in the 100Y and 100Zr materials. The 1000Y material shows a bimodal grain size distribution, with a coarse grain size of ~5 μm, and fine grain size of ~1 μm. The 1000Y material also has secondary phase precipitates which are mainly in the fine grain size Al_2O_3 regions [Fig. 1(c)]. Figure 2 shows STEM annular aperture dark field images and compositional mapping of the dopants. Both techniques reveal that the dopant is segregated narrowly at the grain boundaries, with a distribution width of less than 2 nm. STEM analysis indicates that the grain boundaries of 1000Y show similar features of Y segregation. Details of the microstructural features of these doped materials have been reported elsewhere [14].

2.2. X-ray absorption measurements

X-ray absorption measurements at the K edges of Y and Zr were made on Beamline X23A2 of the National Synchrotron Light Source (NSLS) at
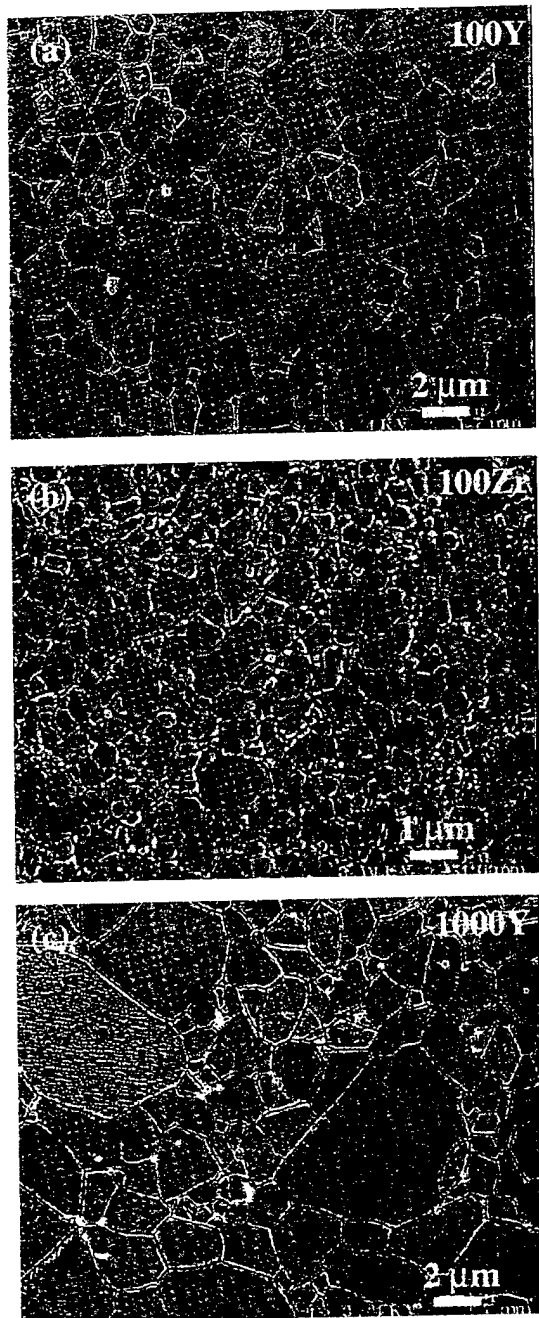
Fig. 1. SEM images of Y-doped and Zr-doped Al_2O_3 samples: (a) 100 p.p.m. Y_2O_3 doped Al_2O_3; (b) 100 p.p.m. ZrO_2 doped Al_2O_3; and (c) 1000 p.p.m. Y_2O_3 doped Al_2O_3. Grain boundaries are visible because of thermal grooving. In (c) some of the YAG precipitates are indicated by arrows.

Brookhaven National Laboratory under normal operating conditions (2.5 GeV, 100–200 mA) and using a Si (311) double crystal monochromator. For bulk materials, the spectra were measured in the fluorescence mode. The incident beam had a cross-section of 3×12 mm^2 and intersected with the specimen surface at 45 deg. An Ar-filled ion chamber was used as the fluorescence detector, posi-

tioned so that the detector window center line also intersected the specimen surface at 45° but was perpendicular to the incident beam direction. Absorption edge jumps in fluorescence were more than 20% of the pre-edge intensity for the 100Y sample and more than 30% for the 100Zr sample (see Fig. 3), so the fluorescence detector was used without filter foils. In order to reduce statistical errors, about 70 spectra were recorded and averaged for the 100Y sample and for the 100Zr sample. For the 1000Y sample only two spectra were collected and averaged to obtain similar statistical accuracy.

Samples of cubic Y_2O_3 powder (purity 99.99%, Alfa, Johnson Matthey Company) and of monoclinic ZrO_2 powder (purity 99.5%, Alfa, Johnson Matthey Company) were measured in transmission mode, and the data were used as standards for the analysis of data from the doped materials. Samples were prepared by encapsulating the powder between pieces of self-adhesive Scotch Magic tape. As a standard for analyzing secondary phase precipitates in the 1000Y material, bulk polycrystalline $Y_3Al_5O_{12}$ (YAG), which includes 5 vol.% Al_2O_3, was also measured in fluorescence mode, but at a detector grazing angle of about 10°. For all the reference samples, at least five spectra were recorded and averaged.

2.3. EXAFS data analysis

For the bulk samples, the fluorescence intensity $I_F(E)$ was normalized by the incident intensity $I_0(E)$ to obtain the absorption spectrum, $\mu(E) = I_F(E)/I_0(E)$. For the powder samples, the transmitted intensity $I_T(E)$ was normalized by the incident intensity $I_0(E)$ to obtain the absorption spectrum, $\mu(E) = -\ln[I_T(E)/I_0(E)]$. A linear function was fitted to the pre-edge region of $\mu(E)$ and was subtracted from $\mu(E)$ in order to isolate the contributions from K-shell absorption, $\mu_K(E)$. The EXAFS function, $\chi(k)$, was extracted from $\mu_K(E)$ using standard procedures [27]: a smooth background, $\mu_0(E)$ was subtracted from $\mu_K(E)$, and then the spectra were normalized by the average value of $\mu_0(E)$ throughout the EXAFS region $\langle\mu_0(E)\rangle$. The values of E greater than the K-absorption edge energy E_0 were converted to values of k

$$k = \sqrt{8\pi^2 m(E - E_0)/h^2} \qquad (1)$$

where m is electron mass and h is Planck's constant. The absorption edge energies were 17.034 keV for Y and 17.998 keV for Zr [28].

The resulting expression for the EXAFS function $\chi(k)$ is

$$\chi(k) = \frac{\mu_K(E) - \mu_0(E)}{\langle\mu_0(E)\rangle}. \qquad (2)$$

The EXAFS distribution function $\Phi_3(r)$ was calculated by Fourier transform of $\chi(k)$
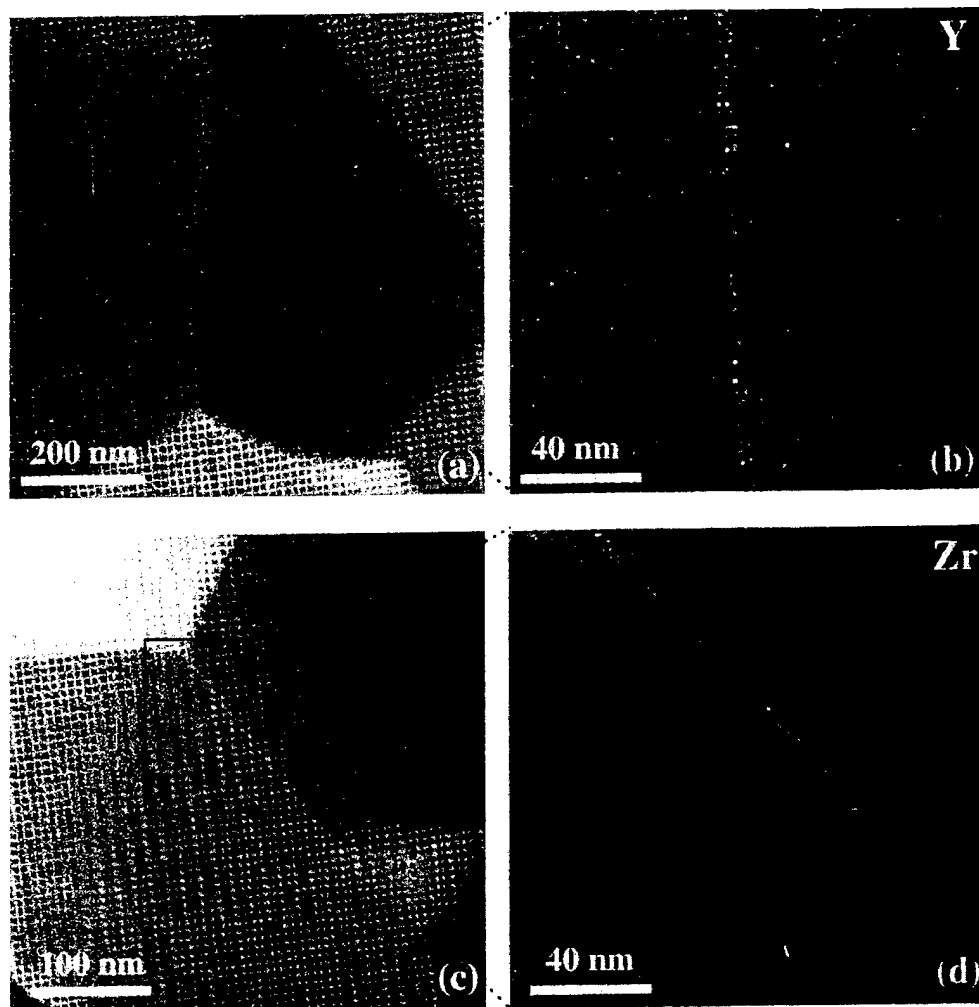
Fig. 2. STEM images, (a) and (c), and EDS maps, (b) and (d), reveal the segregation of the dopants in α-Al$_2$O$_3$ grain boundaries: (a) annular aperture dark field image of 100 p.p.m. Y$_2$O$_3$ doped material and (b) the EDS mapping of Y; (c) annular dark field image of 100 p.p.m. ZrO$_2$ doped material and (d) the EDS mapping of Zr. In the EDS mapping, the electron beam diameter is optimized to 1 nm, and the mapping area is 160 × 160 nm^2 with a total pixel number of 128 × 128.

$$\Phi_3(r) = \int_{k_{min}}^{k_{max}} k^3 \chi(k) \exp(i2kr)\, dk. \tag{3}$$

The nearest neighbor contributions $\chi_{NN}(k)$ were calculated by Fourier transform of $\Phi_3(r)$ with the window functions centered on the nearest neighbor peaks of $|\Phi_3(r)|$ (as shown later in Fig. 6).

The EXAFS spectra were analyzed using the standard EXAFS equation [27]

$$\chi(k) = \sum_j \frac{N_j}{kR_j^2} F_j(k)\, e^{-2\sigma_j^2 k^2}$$

$$e^{-2R_j/\lambda} \sin[2kR_j + \varphi_j(k)] \tag{4}$$

where $F_j(k)$ is the backscattering amplitude from each of the N_j neighboring atoms of type j at distance R_j with a mean square relative displacement σ_j^2, and $\varphi_j(k)$ is the total phase shift experienced by the photoelectron including contributions from both the scatter and absorber. The factor $e^{-2R_j/\lambda}$,

where λ is the photoelectron mean free path, accounts for inelastic scattering.

The average nearest neighbor coordination number, N, the average bond length, R, and the mean squared bond length dispersion, σ^2, around the grain boundary segregated dopant ions were obtained from EXAFS data by data fitting of $\chi_{NN}(k)$ using Win-XAS (version 1.0) software [29] and an *ab initio* multiple scattering EXAFS code (FEFF program, version 7.0) [30]. In this approach, based on the crystallographic data of the model compounds (Table 1), we have calculated the cation–oxygen phase shift and backscattering amplitude functions and have fitted these to the nearest neighbor EXAFS spectra measured for the model compounds. The fitting parameters were S_0^2, the scaling factor which multiplies the theoretical backscattering amplitude and accounts for inelastic scattering; ΔE_0, the adjustment to the absorption edge energy; and σ_j^2, the mean squared bond length dis-
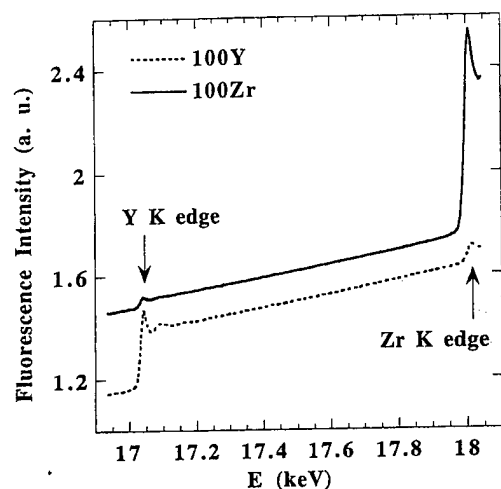
Fig. 3. Typical measurements of X-ray fluorescence intensity for Y and Zr in 100Y and 100Zr, showing that Zr exists as an impurity in 100 p.p.m. Y_2O_3 doped α-Al_2O_3, and also Y exists as an impurity in 100 p.p.m. ZrO_2 doped α-Al_2O_3. The curve for the 100Zr sample has been moved upwards by 0.3 for clarity.
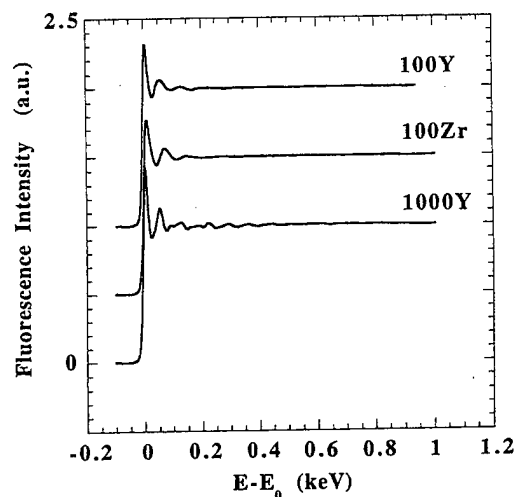

Fig. 4. Normalized X-ray absorption spectra for the doped samples. E_0 is taken as 17.998 keV for Zr and 17.038 keV for Y. For clarity, the curves for 100Y and 100Zr have been moved upwards by 0.5 and 1.0, respectively.

persion. The same values of S_0^2, ΔE_0, phase shifts and backscattering amplitude functions were then used to fit the nearest neighbor EXAFS spectra for the Y- and Zr-doped Al_2O_3 samples. From fitting either Y–O nearest neighbors in Y_2O_3 or Zr–O nearest neighbors in ZrO_2, values obtained for S_0^2 were 0.81, and for ΔE_0 were 0.67 eV.

The fluorescence EXAFS data for the YAG sample were corrected for finite thickness effects using the relationship derived by Jaklevic *et al.* [31] and discussed by Boehme *et al.* [32], together with the absorption coefficients from McMaster *et al.* [28].

3. RESULTS

Figure 3 shows typical measurements of fluorescence intensity as a function of energy for the 100Y and 100Zr samples. The energy range spans the K edges of both Y and Zr. It is interesting to note that the EXAFS signal is very sensitive to the impurity levels. Although the 100Y specimen is nominally doped with only 100 p.p.m. Y, an edge jump at the Zr edge energy can also be seen, indicating that this sample also contains some Zr as an impurity. Based on the edge jump magnitude, the Y:Zr concentration ratio is estimated to be about 100:25. Such a high level of Zr impurity in the 100Y specimen is not expected, since all the raw materials used were ultra-high purity, as indicated in the specimen preparation section. One possible source of the Zr impurity may be surface contamination introduced during machining of the hot-pressed material. However, in the present analysis, we only concentrated on the Y edge in the 100Y specimen.

Similarly, in the 100Zr specimen there is an edge jump corresponding to Y. Based on the edge jump magnitude, Zr:Y = 100:5. Y impurity in the 100Zr specimen is expected, because the Zr dopant was obtained by milling of the alumina slurry with tetragonal ZrO_2 milling media which contains 4.2 mol% Y_2O_3 as stabilizer. This would give a Zr:Y ratio of 100:9, which is roughly consistent with the experimental value of 100:5.

Table 1. Crystallographic data for the model compounds[a]

Compound	Structure	Cation–oxygen bond length (Å)	Coordination number	Ref.
Al_2O_3	Rhombohedral	3×1.852; 3×1.972 average: 6×1.912	6	[33]
Y_2O_3	Cubic	6×2.239; 6×2.289 6×2.273; 6×2.333 average: 6×2.284	6	[34]
$Y_3Al_5O_{12}$	Cubic	4×2.289; 4×2.412 average: 8×2.351	8	[35]
ZrO_2	Monoclinic	1×2.051; 1×2.057; 1×2.151; 1×2.162; 1×2.189; 1×2.220; 1×2.284 average: 7×2.159	7	[36, 37]

[a] Ionic radii (Å): O^{2-}(6): 1.40; Al^{3+}(6): 0.51; Y^{3+}(6): 0.90; Zr^{4+}(7): 0.78, in each case the coordination number is given in parentheses [38].
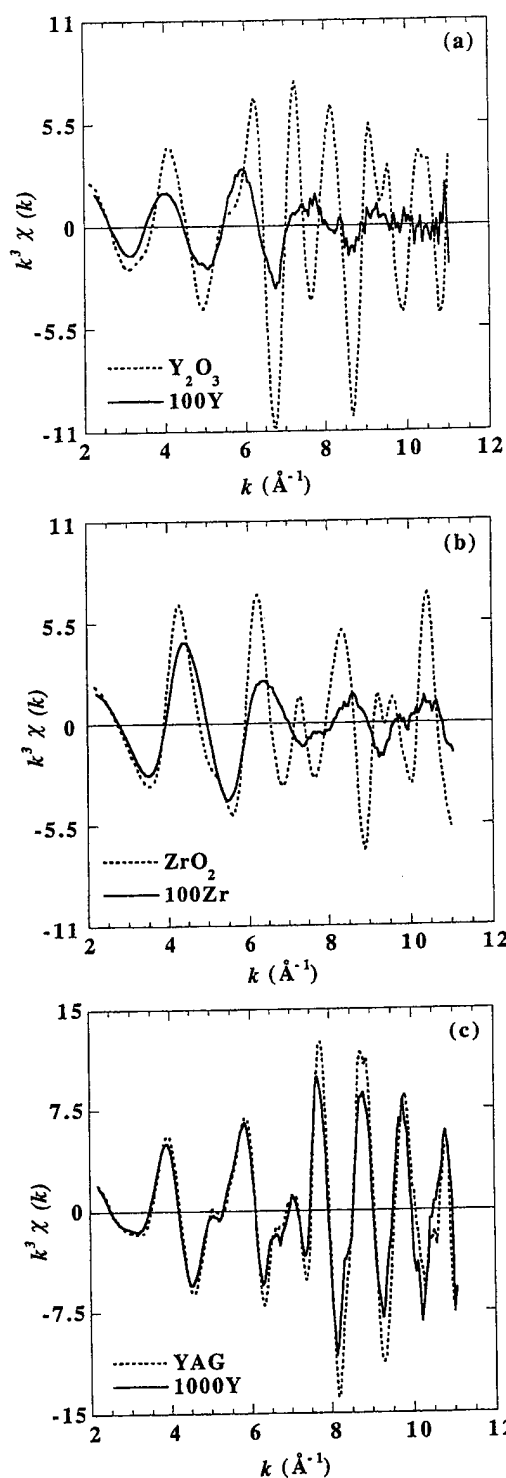
Fig. 5. k^3 weighted $\chi(k)$ EXAFS functions for (a) Y–K edge in 100Y and Y_2O_3; (b) Zr–K edge in 100Zr and monoclinic ZrO_2; and (c) Y–K edge in 1000Y and YAG.

Fig. 6. Fourier transform magnitude $|\Phi_3(r)|$ of the EXAFS spectra in Fig. 5: (a) 100Y and Y_2O_3; (b) 100Zr and monoclinic ZrO_2; and (c) 1000Y and YAG. α represents the distance shift due to the phase shift function in the Fourier transformation. The dashed line window represents the Fourier filtering range for fitting nearest neighbors.

Although the 100Y and 100Zr specimens are nominally doped with 100 p.p.m. Y and 100 p.p.m. Zr, respectively, the edge jump magnitude for Zr in the 100Zr specimen is about three times that for Y in the 100Y speci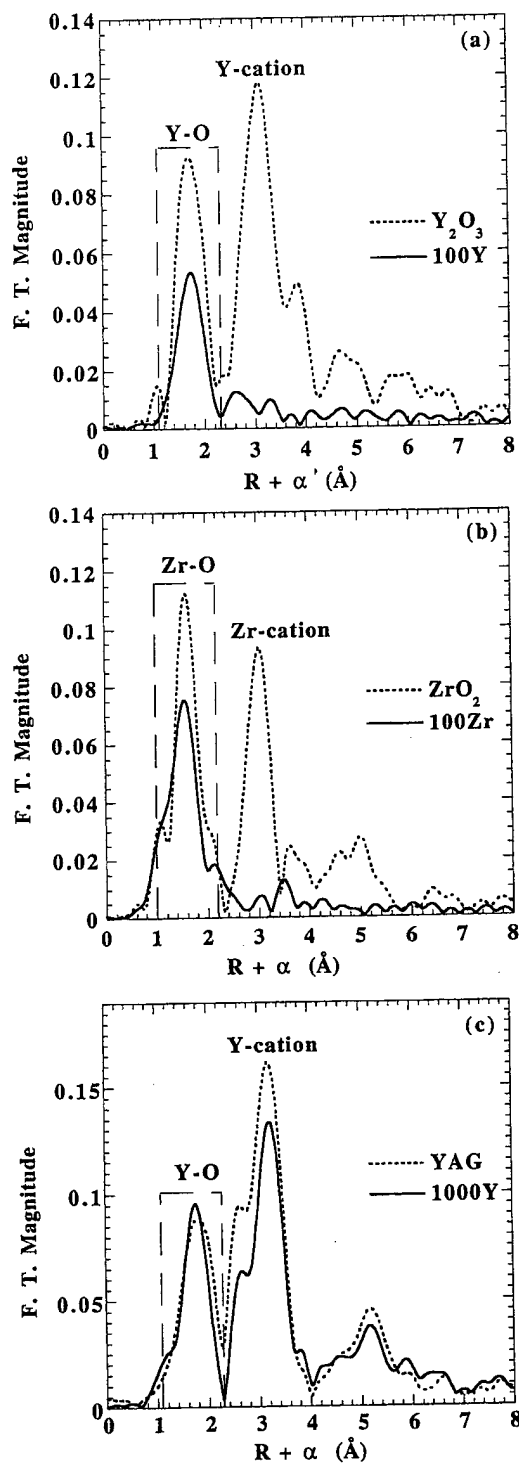men. This indicates that the Zr concentration in the 100Zr specimen is about three times larger than the Y concentration in the 100Y specimen. The actual doping concentration of Y is

Table 2. Fitting results for the doped materials[a]

	100Y Y–O	100Zr Zr–O	1000Y Y–O
Mean radial distance (Å): R	2.30 ± 0.01	2.14 ± 0.01	2.36 ± 0.01
Coordination number: N	4.2 ± 0.5	5.0 ± 0.5	7.5 ± 0.7
Distance dispersion (Å^2): σ^2	0.009 ± 0.001	0.010 ± 0.001	0.008 ± 0.0008

[a] The uncertainties in fitted parameters correspond to a 10% increase in mean square difference between experimental and model $k^3\chi(k)$ functions, when the other parameters are allowed to vary.

expected to be close to the nominal one, because the doping level of Y was obtained by weighing the diluted yttrium nitrate solution. However, the actual Zr doping level may easily differ from the nominal one, because it was only estimated from the time of ball milling.

Figure 4 shows the normalized X-ray absorption spectra for the 100Y, 1000Y, and 100Zr samples. Figures 5(a)–(c) show the Y and Zr $\chi(k)$ EXAFS spectra weighted by k^3 for both the doped alumina materials and the model compounds. The magnitudes of the Fourier transforms $|\Phi_3(r)|$ of the $k^3\chi(k)$ EXAFS functions in Fig. 5 are shown in Fig. 6. Although $|\Phi_3(r)|$ gives the radial distribution around the absorbing atom, the EXAFS phase shift function in the Fourier transformation causes the peaks to be shifted to smaller distances [27]. This is indicated by including a peak shift α symbolically in the ordinate for $|\Phi_3(r)|$ in Figs 6 and 8. Qualitative comparisons of the radial distribution functions for the doped materials and the model compounds indicate that EXAFS in the 100Y [Figs 5(a) and 6(a)] and 100Zr [Figs 5(b) and 6(b)] samples are similarly dominated by the cation–oxygen nearest neighbor (NN) shell; the cation–cation next nearest neighbor (NNN) shell cannot be clearly identified. The radial distribution function for the 1000Y sample shows the same features as the YAG standard sample. The large difference in the radial distribution functions between the 100Y and 1000Y samples, and the very similar radial distribution functions for 1000Y and YAG samples, indicate that most of the dopant in the 1000Y sample is precipitated in the form of YAG, and this is consistent with the estimate from STEM data that ~87% of the total dopant in the 1000Y sample appears as the YAG phase [17]. There are no second phase precipitates in the 100Y and 100Zr samples, so the radial distribution functions for the 100Y and 100Zr reflect the structural environments of dopant sites in alumina grain boundaries, and to some extent in the bulk lattice.

Quantitative fitting of the first shell of the EXAFS data of the 100Y and 100Zr samples gives the average coordination number and the average NN cation–oxygen bond length around the largely grain boundary segregated Y and Zr, and those results are summarized in Table 2. Y–O and Zr–O nearest neighbor $k^3\chi(k)$ function used in fitting for 100Y and 100Zr samples are shown in Fig. 7, in

which the Fourier filtering range for Y–O NN in the 100Y sample is from 1.1 to 2.3 Å, and for Zr–O NN in the 100Zr sample is 1.0–2.2 Å, as shown in Figs 6(a) and (b). Deviations between calculated and experimental $k^3\chi(k)$ functions for the 100Y and 100Zr samples in Fig. 7 are similar to those obtained in fitting Y–O nearest neighbors in 1000Y and Y_2O_3 samples or Zr–O nearest neighbors in ZrO_2, using theoretical phase shifts and backscattering amplitudes in all cases.

The grain boundary segregated Y is coordinated on average by approximately four oxygens at an average distance of 2.30 Å, which is approximately equal to the average Y–O NN bond length, 2.28 Å, in cubic Y_2O_3 (Table 1), but is much larger than the Al–O NN bond length, 1.91 Å, in α-Al_2O_3. However, in both Al_2O_3 and Y_2O_3, the cation is coordinated by six oxygens (octahedral configuration). For the 1000Y sample, fitting gives an average Y–O NN bond length of 2.36 Å, which is approximately equal to that, 2.35 Å, in YAG
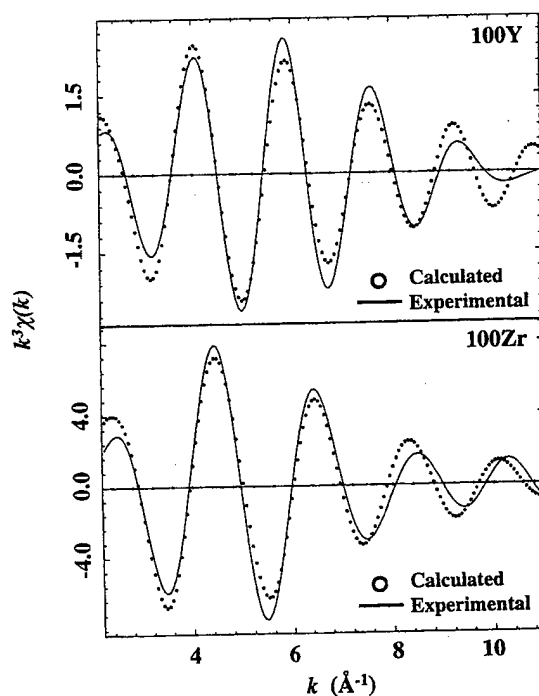

Fig. 7. k^3 weighted nearest neighbor component of $\chi(k)$ for Y in 100Y and Zr in 100Zr and fitted model calculations (open circles). The Fourier filtering range is 1.1–2.3 Å for Y, and 1.0–2.2 Å for Zr.

(Table 2). The grain boundary segregated Zr is coordinated on average by five oxygens at an average Zr–O NN distance of 2.14 Å, which is approximately equal to the average Zr–O NN bond length, 2.16 Å, in monoclinic ZrO$_2$. However, this Zr–O coordination number is smaller than that of the zirconia polymorphs, for which the minimum Zr–O coordination number is 7.

4. DISCUSSION

4.1. Lattice solid solution, grain boundary segregation, and second phase precipitates

In any substitutional doping system with a tendency for dopant grain boundary segregation, if the dopant concentration is above the solid solution limit a secondary phase based on the dopant may precipitate. In this case, the EXAFS signal is expected to be a superposition of contributions from three different environments: dopant precipitated as a secondary phase, dopant segregated to the grain boundaries or other defects (such as dislocation cores), and dopant as a substitutional solute in the host lattice. Owing to the different atomic configurations in these three structures, the EXAFS spectra carry information about the relative proportion of each of these three states of the dopant. Based on this, the solid solution limit of the Y as a dopant in α-Al$_2$O$_3$ can be estimated using the EXAFS $\chi(k)$.

Significant difference in the EXAFS data of 100 and 1000 p.p.m. Y$_2$O$_3$ doped materials, and the striking similarity between EXAFS data for the 1000 p.p.m. data and the YAG data, indicate that Y has a rather low solid solubility in the bulk or in grain boundaries of α-Al$_2$O$_3$. This is consistent with the microstructural evidence that there are many YAG precipitates in the 1000 p.p.m. Y$_2$O$_3$ doped material. If most of the Y atoms are in secondary phase precipitates, their EXAFS contributions will mask those of Y atoms segregated in grain boundaries or located in bulk substitutional sites. Using EXAFS, Loudjani et al. [19] attempted to determine the local atomic structure around Y in 1 mol% Y$_2$O$_3$ doped alumina, but their fitted results were actually dominated by the YAG. Later, Loudjani et al. also studied 300 p.p.m. Y$_2$O$_3$ doped alumina, and they obtained some information not dominated by the YAG phase [20]. They found a radial distribution function with a high Y–oxygen peak, consistent with our result for the 100Y sample. However, their data also showed a small peak attributed to Y–Al neighbors.

The present investigation of more dilute doping, at the level of 100 p.p.m., and with the materials in the grain size range of less than 2 μm, avoids the uncertainties caused by secondary phase precipitates. For the 100Y and 100Zr doped alumina samples, our TEM observations show that at least
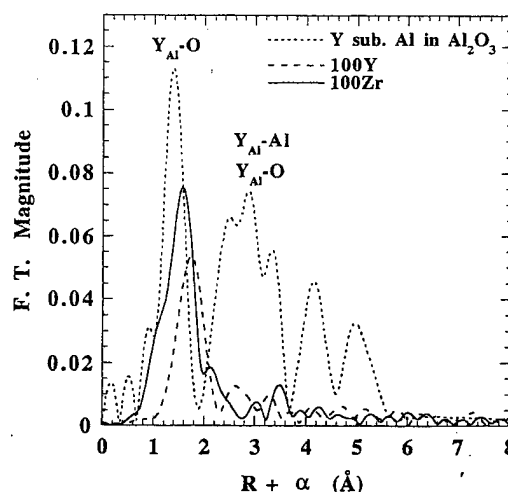

Fig. 8. Comparison of the experimentally obtained radial distribution functions for 100Y and 100Zr samples with that calculated supposing Y substitutes for Al in α-Al$_2$O$_3$ without relaxing the Y$_{Al}$–O bond length. Note the significant Y$_{Al}$–Al and Y$_{Al}$–O next nearest neighbor peaks in the calculated function which are not present in the experimental functions.

99% of the grains are dislocation free. However, in principle, EXAFS spectra from the 100Y and 100Zr samples are still superpositions of two contributions, one from the dopant in substitutional sites of the α-Al$_2$O$_3$ lattice and another from the dopant segregated to the Al$_2$O$_3$ grain boundaries.

Figure 8 is a comparison of the radial distribution functions for the 100Y and 100Zr samples with those calculated for Y in a substitutional cation site in α-Al$_2$O$_3$. For simplicity, the calculation was without relaxation of the Y$_{Al}$–O bond length. The calculated distribution function has next nearest neighbor Y–Al and Y–oxygen peaks which are nearly as strong as the nearest neighbor Y–oxygen peak. Absence of a significant Y–Al peak for the 100Y sample, or a Zr–Al peak for the 100Zr sample, indicates that most of the Y and Zr atoms in these samples are not in bulk substitutional sites, but are grain boundary segregated, so the resulting atomic configurational parameters describe the dopant surroundings in α-Al$_2$O$_3$ grain boundaries.

These results also indicate that the solubility of Y and Zr in the bulk lattice of α-Al$_2$O$_3$ is very low. Available literature data on the lattice solid solution limit of Y and Zr in α-Al$_2$O$_3$ are quite limited. Based on AES analysis, McCune et al. [39] suggested that Y in α-Al$_2$O$_3$ has a solid solution limit of less than 10 p.p.m.

Based on the observation that grain boundary segregated Y only gives a Y–O NN coordination peak as in the 100Y sample [Figs 5(a) and 6(a)], using the $k^3\chi(k)$ functions of the 100Y [Fig. 5(a)], 1000Y [Fig. 5(c)], and YAG standard samples [Fig. 5(c)], the ratio of the Y in the grain boundaries and that precipitated as YAG in the 1000Y sample may be estimated. Based on superposition of grain
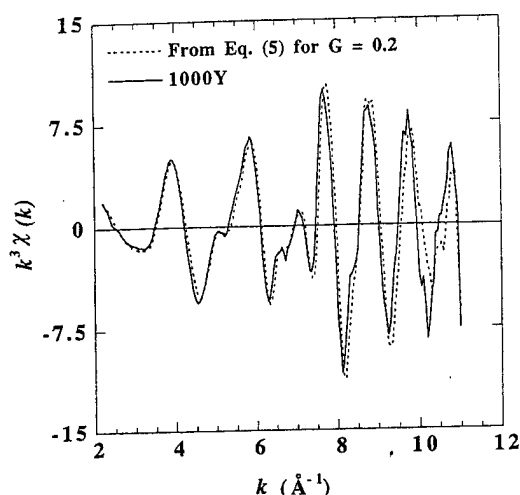
Fig. 9. Comparison of the experimentally obtained $k^3\chi(k)$ function for the 1000Y sample with that obtained by adding together the $k^3\chi(k)$ functions of the 100Y and YAG with $G = 0.2$ in equation (5).

boundary and precipitate contributions for the 1000Y sample, the fraction of the Y segregated in the grain boundaries of alumina in the 1000Y, G, can be obtained from the following equation:

$$Gk^3\chi_{100Y}(k) + (1 - G)k^3\chi_{YAG}(k) = k^3\chi_{1000Y}(k) \quad (5)$$

where $k^3\chi_{100Y}(k)$ is the $k^3\chi(k)$ function for 100Y, $k^3\chi_{YAG}(k)$ is the $k^3\chi(k)$ function for YAG, and $k^3\chi_{1000Y}(k)$ is the $k^3\chi(k)$ function for 1000Y. Equation (5) gives a G value of approximately 0.2, and the nearly exact superposition, shown in Fig. 9, for the simulated $k^3\chi_{1000Y}(k)$ calculated from equation (5) with $G = 0.2$ and the experimental $k^3\chi_{1000Y}(k)$ confirm this value. From this result, we conclude that of the 1000 p.p.m. Y_2O_3 in the 1000Y sample, ~20% is segregated to the grain boundaries (200 p.p.m. in the grain boundaries and this corresponds to Y grain boundary excess of ~6.0 atoms/nm²) and ~80% is precipitated as YAG.

This result is fairly consistent with the estimate from STEM data for the same material that ~130 p.p.m. of the dopant is segregated to the alumina grain boundaries [17]. We calculated the latter value from the grain boundary excess dopant amount given in Ref. [17] and the average grain size of the doped material.

4.2. Grain boundary segregation sites and relaxation around the segregant

It has been proposed that the ionic size mismatch between the solute and the matrix lattice is the dominant driving force for solute grain boundary segregation [2, 4]. The Y and Zr ions are larger than the Al ions, and they show strong tendency for segregating to α-Al_2O_3 grain boundaries. Information about the sites in α-Al_2O_3 grain boundaries occupied by segregants has been sought both from experiments and from theoretical calculations

[17, 20, 40]. Although the Zr and Y have different ionic sizes, the similarity in their EXAFS radial distribution functions [Figs 6(a), (b), and 8] strongly suggests that the Y and Zr have similar environments, at least within the range of the nearest and next nearest neighbors (within 3 Å). Both distribution functions show prominent cation–oxygen nearest neighbors but no well defined more distant neighbors. This implies that the Y and Zr are indeed similarly and mainly segregated to the alumina grain boundaries. The most plausible sites in the grain boundary of α-Al_2O_3 for the segregants Y and Zr are the substitutional Al ion sites. If Y and Zr substitute for Al ions in the Al_2O_3 grain boundaries, this requires relaxation of the oxygen ions around the segregants. The present results indicate that the oxygens surrounding the Y and Zr are completely relaxed to the same bond lengths as in Y_2O_3 and ZrO_2. This corresponds to the nearest neighbor oxygen atoms around the yttrium moving outward by 19%, and to those around the zirconium moving outward by 13% with respect to the normal Al–O distance.

Calculations of cation–oxygen relaxation have been reported for both bulk and grain boundary sites. Ching et al. [41] have conducted an ab initio calculation in which an yttrium replaces an aluminum ion in a supercell of α-Al_2O_3 containing 120 atoms. They found that the nearest neighbor oxygen atoms around the Y moved outward by 8%. This is less than half the relaxation indicated by the present EXAFS measurements if they are interpreted as Y substituting for Al in the grain boundary of α-Al_2O_3. Cho [40] has also treated the substitution of Al by La and Yb in the basal twin boundary of α-Al_2O_3. The results confirm that large cation–oxygen relaxation can occur for rare earth dopants in Al_2O_3 grain boundaries.

A good way to view the difference between grain boundary substitutional sites and bulk lattice substitutional sites may be to observe that in the undoped grain boundary some cation sites are locally compressed and some are locally dilated, whereas in the bulk lattice all cation sites are identical. In the grain boundary, the misfitting dopants, which have larger ionic sizes than Al, preferentially occupy the larger sites, so only small local distortions are required to obtain the ideal nearest neighbor distances, like those in the parent oxides. Larger, higher energy distortions would be required in the bulk. The grain boundary sites are energetically favored compared with the bulk substitutional sites, which makes solubility of the dopants in the grain boundaries much higher than in the Al_2O_3 bulk.

4.3. Coordination numbers

The reduced cation–oxygen coordination numbers for the grain boundary segregated Y ($N = 4.2$) and Zr ($N = 5.0$) ions obtained from the EXAFS measurements are believed to be significant. We

estimate uncertainties in these coordination numbers to be only ± 0.5, as shown in Table 2. In the perfect lattices of α-Al$_2$O$_3$ and Y$_2$O$_3$, Al and Y each have six oxygen nearest neighbors, and in the polymorphs of zirconia, each Zr has at least seven oxygen nearest neighbors. In this section, we first discuss generally the reduced cation–oxygen coordination number for grain boundary segregated Y and Zr compared with their parent oxides and with α-Al$_2$O$_3$. We then discuss the difference in the grain boundary cation–oxygen coordination numbers between Y and Zr.

We believe that the smaller cation–oxygen coordination numbers of the grain boundary segregated Y and Zr, compared with those in their parent oxides and in α-Al$_2$O$_3$, are related to the intrinsic structure of alumina grain boundaries [42]. Both theoretical modeling and STEM energy-loss near-edge structure (ELNES) studies of a near $\Sigma 11$ grain boundary in α-Al$_2$O$_3$ have established that in this boundary some Al ions are coordinated by only four O atoms [43–45]. Similar results have also been obtained by ELNES analysis of more general grain boundaries in 0.1 mol% ZrO$_2$ doped alumina [21]. Apparently, distortions in cation arrangements in α-Al$_2$O$_3$ grain boundaries, which optimally join together adjacent misoriented crystalline grains, are accommodated by reduced cation–oxygen coordination. The presently observed overall low oxygen coordination number around the grain boundary segregated Y and Zr seems to be consistent with these theoretical models and ELNES observations of grain boundaries in pure and doped α-Al$_2$O$_3$.

In considering the reduced cation–oxygen coordination numbers in α-Al$_2$O$_3$ grain boundaries, it may be useful to think of the grain boundary as being formed by bringing together the free surfaces of two misoriented grains. On the clean, free surfaces, Al ions will, on average, have reduced oxygen coordinations of about 4.5, consisting of three oxygen atoms shared with other Al ions within the bulk, and one or two non-bridging oxygen atoms. When the free surfaces are brought together, with rotations or displacements to accommodate the grain-to-grain misorientation, some of the Al atoms adjacent to the boundary will have a cation–oxygen coordination less than six, and some will have more than six. The undercoordinated sites may be the energetically preferred sites for Y or Zr to substitute for Al.

In α-Al$_2$O$_3$ and MgO-doped α-Al$_2$O$_3$, the thermal grooving induced grain boundary dihedral angles are $\sim 110°$, which implies that the grain boundary energy is approximately equal to the air-exposed α-Al$_2$O$_3$ surface energy [46]. This suggests that the atom coordination in the grain boundary may be similar to that in the free surface, which may retain its cation–oxygen under coordination. However, for a free surface, it is likely that additional oxygen is added by chemisorption from the air, typically as

hydroxyl attachments. We recognize that this discussion is quite speculative. Further experimental studies, combining HRTEM, STEM and EXAFS, together with modeling and simulation calculations, are needed to develop a detailed structural picture of dopant segregation in grain boundaries.

We note that Loudjani et al. [20] have used EXAFS to determine the oxygen coordination number around the Y in 300 p.p.m. Y$_2$O$_3$ doped alumina. They found that the nearest oxygen coordination number around the Y to be only about 2.7 (with a Y–O distance of 2.32 Å). They also noticed an additional shell of oxygen at 2.85 Å with a coordination number of 1.7. Adding those two shells together gives a total Y–O coordination number of 4.4, which is within the range we have obtained, although the second shell Y–O distance is larger than we obtained.

The experimentally observed difference in the cation–oxygen coordination numbers for Y and Zr may be due to differences in the ionic sizes and valences between Y and Zr. Since Y is larger than Zr, and both are larger than Al, large local distortions or structural modifications will be required if Y or Zr replace Al in a grain boundary, the more so for Y than for Zr. To allow relaxation of cation–oxygen nearest neighbor distances to those which are energetically favorable for the larger cations, while retaining a local cation concentration of at least 50% Al, local removal of oxygens, or introduction of oxygen vacancies, may be required. This would lead to a reduced cation–oxygen coordination number for Y and for Zr, with a larger reduction expected for the larger Y atom, as observed experimentally.

The smaller ionic size of Zr compared with Y might lead to greater substitutional solubility of Zr in the Al$_2$O$_3$ grains. This would give rise to a higher cation–oxygen coordination number for Zr. However, if there were significant substitutional solubility of Zr in the Al$_2$O$_3$ grains, second neighbor Zr–Al contributions would be expected in the Zr EXAFS distribution functions, which are not found in the present experimental results.

The larger ionic valence of Zr, $+4$, compared with that of Y, $+3$, may also play a role in Zr having a larger cation–oxygen coordination number than Y. Simply replacing an Al^{3+} ion by a Zr^{4+} ion would require a coordination of oxygen around Zr of more than six to maintain local charge neutrality. Similar effects may occur in the grain boundary, leading to Zr^{4+} having a larger cation–oxygen coordination than Y^{3+}.

4.4. Further implications

Based on the present EXAFS results, the atomic structural environment around the grain boundary segregated Y and Zr may be as illustrated schematically in Fig. 10. In this figure, the classic two-dimensional representations of amorphous and crys-

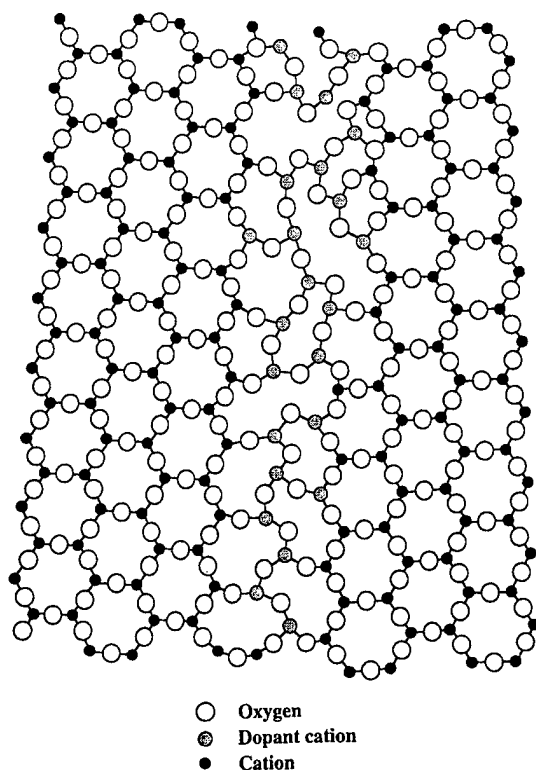○ Oxygen
◎ Dopant cation
● Cation

Fig. 10. A two-dimensional schematic drawing showing that each dopant ion segregated to the grain boundary is coordinated by oxygen nearest neighbors at well defined distances, while the next nearest neighbor distances are changing from site to site. The grain boundary segregated ion concentration and the grain boundary width are exaggerated in this drawing.

talline phases are used, such that the oxygens surrounding each dopant ion are ordered and have fixed bond lengths, while the dopant–cation next nearest neighbors are disordered. However, both the concentration of the dopant segregated to the grain boundary and the dopant distribution width around the grain boundary are exaggerated in this illustration.

Also relevant to the present observations is the equilibrium glassy film in liquid phase sintered silicon nitride. This ~1 nm thick film composed of $Si(N)-O_4$ tetrahedra is sandwiched between the Si_3N_4 crystalline grains [47]. Configurationally, the arrangement of the dopant–oxygen cluster in the alumina grain boundary may be similar to the $Si(N)-O_4$ tetrahedral arrangement in the glass film between silicon nitride grains. In both cases, the cation–oxygen distance is very well defined, while the cation–cation distance is changing from site to site. However, it should be noted that HRTEM observations indicate that grain boundaries of Y and Zr doped alumina have no more than one or two monolayers of disordered material [21].

It would be expected, in a co-doping system, that the larger dopant ions will selectively occupy the larger sites, and the smaller dopant ions will occupy

the smaller sites. In comparison with random substitutional site occupancy, this would give a more efficient filling of the grain boundary free space when co-doping alumina with two dopants having different ionic sizes. This would also provide a structural basis for the synergistic effect of Nd and Zr co-doping improving the creep resistance of alumina, which has been attributed to the co-doping providing more efficient inhibition of grain boundary mediated transport [14].

The complete relaxation of the cation–oxygen bond lengths to that in the parent oxides observed in the EXAFS measurements for the 100Y and 100Zr samples is noteworthy. A complete relaxation of the bond length between the dopant and the oxygen suggests that the grain boundary segregated ions are in stable positions. However, it remains to be established how the segregant may itself modify the grain boundary structure.

5. CONCLUSIONS

EXAFS analysis of Y_2O_3 and ZrO_2 doped ultrahigh purity alumina indicates that dopants at the level of 100 p.p.m. are mainly segregated to the alumina grain boundaries. This is generally consistent with SIMS and STEM studies of the grain boundary segregation behavior of rare earth and ZrO_2 doped alumina. EXAFS data indicate that the grain boundary segregated Y and Zr ions have well defined dopant (Y, Zr)–O nearest neighbor coordinations, but that the dopant (Y, Zr)–cation next nearest neighbor coordination is changing from site to site. The dopant (Y, Zr)–oxygen nearest neighbor bond length in the grain boundary, on average, is fully relaxed to that in the dopant cation parent oxides. However, the dopant (Y, Zr)–O nearest neighbor coordination number is ~30% smaller than that in their parent oxides.

It may be speculated that the grain boundary segregated Y and Zr occupy substitutional Al sites in the boundaries. The overall pattern of those local atomic structural features around the grain boundary segregated dopant ions reflects two factors: the intrinsic structural imperfection of the alumina grain boundary and the role of the ionic size mismatch between the dopant and the host lattice. However, it remains to be established to what degree the valence difference between the dopant cation Zr^{4+} and the host cation Al^{3+} influences the local structure.

measurements were made at NSLS, Brookhaven National Laboratory, which is supported by the DoE.

REFERENCES

1. Rittner, J. D. and Seidman, D. N., *Acta mater.*, 1997, **45**, 3191.
2. Li, C. W. and Kingery, W. D., in *Advances in Ceramics, Vol. 10, Structure and Properties of MgO and Al₂O₃ Ceramics*, ed. W. D. Kingery. American Ceramic Society, Columbus, OH, 1984, pp. 368–378.
3. Thompson, A. M., Soni, K. K., Chan, H. M., Harmer, M. P., Williams, D. B., Chabala, J. M. and Levi-Setti, R., *J. Am. Ceram. Soc.*, 1997, **80**, 373.
4. Johnson, W. C., *Metall. Trans. A*, 1977, **8A**, 1413.
5. Hondros, E. D. and Seah, M. P., *Int. metall. Rev.*, 1977, **22**, 262.
6. Gall, M. L., Huntz, A. M., Lesage, B., Monty, C. and Bernardini, J., *J. Mater. Sci.*, 1995, **30**, 201.
7. French, J. D., Zhao, J., Harmer, M. P., Chan, H. M. and Miller, G. A., *J. Am. Ceram. Soc.*, 1994, **77**, 2857.
8. Wakai, F., Nagano, T. and Iga, T., *J. Am. Ceram. Soc.*, 1997, **80**, 2361.
9. Cho, J., Harmer, M. P., Chan, H. M., Rickman, J. M. and Thompson, A. M., *J. Am. Ceram. Soc.*, 1997, **80**, 1013.
10. Lartigue, S., Carry, C. and Priester, L., *J. Phys. (Paris)*, 1990, **C1(51)**, 985.
11. Lartigue, S., Priester, L., Dupau, F., Gruffel, P. and Carry, C., *Mater. Sci. Engng*, 1993, **A164**, 211.
12. Cho, J., Chan, H. M., Harmer, M. P. and Rickman, J. M., *J. Am. Ceram. Soc.*, 1998, **81**, 3001.
13. Gulgun, M. A., Putlayev, V. and Ruhle, M., *J. Am. Ceram. Soc.*, 1999, **82**, 1849
14. Li, Y., Wang, C. M., Chan, H. M., Rickman, J. M., Harmer, M. P., Chabala, J. M., Gavrilov, K. L. and Levi-Setti, R., *J. Am. Ceram. Soc.*, 1999, **82**, 1497
15. Cook, R. F. and Schrott, A. G., *J. Am. Ceram. Soc.*, 1988, **71**, 50.
16. Taylor, R. I., Coad, J. P. and Brook, R. J., *J. Am. Ceram. Soc.*, 1974, **57**, 539.
17. Bruley, J., Cho, J., Chan, H. M., Harmer, M. P. and Rickman, J. M., *J. Am. Ceram. Soc.*, in press.
18. Clarke, D. R., *J. Am. Ceram. Soc.*, 1980, **63**, 339.
19. Loudjani, M. K., Roy, J. and Huntz, A. M., *J. Am. Ceram. Soc.*, 1985, **68**, 559.
20. Loudjani, M. K., Huntz, A. M. and Cortes, R., *J. Mater. Sci.*, 1993, **28**, 6466.
21. Kaneko, K., Gemming, T., Tanaka, I. and Mullejans, H., *Phil. Mag. A*, 1998, **77**, 1255.
22. Kaplan, W. D., Mullejans, H., Ruhle, M., Rodel, J. and Claussen, N., *J. Am. Ceram. Soc.*, 1995, **78**, 2841.
23. Tang, C., Georgopoulos, P. and Cohn, J. B., *J. Am. Ceram. Soc.*, 1982, **65**, 625.
24. Li, P., Chen, I. W. and Penner-Hahn, J. E., *J. Am. Ceram. Soc.*, 1994, **77**, 118.
25. Kavanagh, K. L. and Cargill, G. S. III, *Phys. Rev. B*, 1992, **45**, 3323.
26. Wang, C. M., Cho, J., Chan, H. M., Harmer, M. P. and Rickman, J. M., *J. Am. Ceram. Soc.*, submitted.
27. Teo, B. K., *EXAFS: Basic Principles and Data Analysis*. Springer-Verlag, New York, 1986.
28. McMaster, W. H., Kerr Del Grande, N., Mallett, J. H. and Hubbell, J. H., Compilation of X-ray cross section, Report No. UCRL-50174 Sec. II, Rev. 1, Lawrence Radiation Laboratory, Livermore, CA, May 1969. National Technical Information Service, Springfield, VA.
29. WinXAS 97, version 1.0, written by Thorsten Ressler, available from T. Ressler, E-mail: Ressler@FHI-Berlin.mpg.de.
30. Rehr, J. J., Mustre de Leon, J., Zabinsky, S. I. and Albers, R. C., *J. Am. chem. Soc.*, 1991, **113**, 5135.
31. Jaklevic, J., Kirby, J. A., Klein, M. P., Robertson, A. S., Brown, G. S. and Eisenberger, P., *Solid St. Commun.*, 1977, **23**, 679.
32. Boehme, R. F., Cargill, G. S. III, Weber, W. and Jackson, T., *J. appl. Phys.*, 1985, **58**, 811.
33. Ishizawa, N., Miyata, T., Minato, I., Marumo, F. and Iwai, S., *Acta crystallogr.*, 1980, **B36**, 228.
34. Bonnet, M. and Delapalme, A., *Acta crystallogr.*, 1975, **A31**, 264.
35. Euler, F. and Bruce, J. A., *Acta crystallogr.*, 1965, **19**, 971.
36. Smith, D. K. and Newkirk, H. W., *Acta crystallogr.*, 1965, **18**, 983.
37. Howard, C. J., Kisi, E. H., Roberts, R. B. and Hill, R. J., *J. Am. Ceram. Soc.*, 1990, **73**, 2828.
38. Shannon, R. D., *Acta crystallogr.*, 1976, **A32**, 751.
39. McCune, R. C., Donlon, W. T. and Ku, R. C., *J. Am. Ceram. Soc.*, 1986, **69**, C196.
40. Cho, J., Ph.D. thesis, Lehigh University, 1998.
41. Ching, W. Y., Xu, Y. N. and Ruhle, M., *J. Am. Ceram. Soc.*, 1997, **80**, 3199.
42. Exner, M. and Finnis, M. W., *Mater. Sci. Forum*, 1996, **207–209**, 225.
43. Kenway, P. R., *J. Am. Ceram. Soc.*, 1994, **77**, 349.
44. Hoche, T., Kenway, P. R., Kleebe, H. J., Ruhle, M. and Morris, P. A., *J. Am. Ceram. Soc.*, 1994, **77**, 339.
45. Mo, S. D., Ching, W. Y. and French, R. H., *J. Am. Ceram. Soc.*, 1996, **79**, 627.
46. Handwerker, C. A., Dynys, J. M., Cannon, R. M. and Coble, R. L., *J. Am. Ceram. Soc.*, 1990, **73**, 1371.
47. Kleebe, H. J., Cinibulk, M. K., Tanaka, I., Bruley, J., Vetrano, J. S. and Ruhle, M., in *Tailoring of Mechanical Properties of Si₃N₄ Ceramics*, ed. M. J. Hoffmann and G. Petzow. Kluwer Academic, Dordrecht, 1993, pp. 259–274.

3.2 Structural Features of Y-Saturated and Supersaturated Grain Boundaries in Alumina

By

C. M. Wang, G. S. Cargill III, M. P. Harmer, and H. M. Chan,

STRUCTURAL FEATURES OF Y-SATURATED AND SUPERSATURATED GRAIN BOUNDARIES IN ALUMINA

C. M. WANG, G. S. CARGILL III, H. M. CHAN and M. P. HARMER†

Materials Research Center, Lehigh University, Bethlehem, PA 18015, USA

Abstract—Grain boundary segregation of Y in α-Al_2O_3 and evolution of the structural environment around the Y atoms have been investigated using high resolution STEM and EXAFS. The stages of incorporation of Y atoms by α-Al_2O_3 grain boundaries, on average, are characterized by three composition regimes: (I) dilute to saturated; (II) supersaturated [where the degree of supersaturation is determined by the nucleation barrier for $Y_3Al_5O_{12}$ (YAG)]; and (III) equilibrium with YAG precipitates. The average Y grain boundary concentration in equilibrium with YAG precipitates has been determined to be ~1/4 equivalent monolayer, and the maximum supersaturation concentration has been determined to be ~1/2 equivalent monolayer. EXAFS revealed that accompanying the supersaturation of grain boundaries with Y is an increasing Y–O nearest neighbor coordination number and, simultaneously, a significantly increased degree of ordering of Y with respect to Al ions beyond nearest neighbor O. This Y–Al distance is the same as that for Y absorbed on the free surface of α-Al_2O_3, and the same as that expected for the Y–Al distance when Y substitutes for Al with the Y–O distance relaxed to that in Y_2O_3. This compositional and structural information has led to a clearer picture of how the grain boundary segregated Y concentration influences grain boundary structure. For dilute Y concentrations, Y ions preferentially fill sites in the grain boundary core which have well defined order only within the nearest neighbor shell of oxygens. As the Y concentration increases, Y begins to occupy near-boundary sites, forming two near-boundary layers, each adjacent to a grain surface. The near-boundary layer has nearest neighbor ordering extending at least to nearest neighbor cations. Nucleation of the YAG phase leads to the depletion of Y from these partially ordered layers. © 2000 Published by Elsevier Science Ltd on behalf of Acta Metallurgica Inc. All rights reserved.

Keywords: Grain boundaries; Creep; Segregation; EXAFS; Oxides

1. INTRODUCTION

Doping of trace amounts of rare earth elements or of Zr in high purity alumina or in superalloys significantly affects the materials' microstructures and properties [1–5]. In the case of alumina doped with Y, the creep resistance increases by two orders of magnitude [4, 5]. High resolution scanning transmission electron microscopy (HR-STEM) and high resolution secondary ion mass spectroscopy (HR-SIMS) have established that the dopant Y ions are mainly segregated to the alumina grain boundaries [5–7]. This is consistent with the result showing that, based on auger electron spectroscopy (AES) analysis, the solubility of Y in the bulk lattice of α-Al_2O_3 is < 10 p.p.m. [8, 9]. The mechanism by which the creep resistance is improved by the dopant has been postulated to be a reduced grain boundary diffusivity, which may be caused by the oversized dopant ions blocking critical diffusing paths along the grain boundaries [3–5]. Segregation of Y in alumina grain boundaries also modifies alumina grain growth and intergranular fracture, which are yet to be fully characterized [10].

Effects of a dopant on a material's behavior are normally described in terms of the relationship between the affected properties and the overall doping concentration. However, a dopant may appear in more than one form, for example as a lattice solid solute, as a grain boundary segregant, and as a component of precipitates. In such cases, it is important to identify the form of the dopant that dominantly influences the material's properties. For example, the improved creep resistance in Y doped alumina is mainly related to the segregation of the Y in the alumina grain boundaries, rather than to the presence and number of YAG precipitates [11, 12].

Classically, partition of the dopant between grain boundary and bulk lattice sites is described by the McLean equation [13]

---

† To whom all correspondence should be addressed.

$$\frac{C_{\text{BL}}}{C_{\text{GB}}} = \exp\left(\frac{\Delta G}{RT}\right) \equiv \frac{1}{\beta} \qquad (1)$$

where C_{GB} and C_{BL} are the dopant grain boundary and bulk lattice solid solution concentrations (defined as the ratio of sites occupied by the dopant and the cation sites), ΔG is the free energy of segregation, and $\beta = \exp(-\Delta G/RT)$ is the grain boundary enrichment factor. For equiaxed polycrystalline materials, the grain boundary area per unit volume is inversely proportional to the grain size. The number of grain boundary sites per unit volume therefore decreases with increase of the grain size. For a constant dopant concentration, with the increase of grain size, the dopant grain boundary and lattice solid solution concentrations increase. Upon saturation of both the grain boundary sites and the lattice solid solution, the excess dopant may appear as a second phase precipitate.

Terwilliger and Chiang [14] and Colbourn et al. [15] have observed, for fine grain-sized polycrystalline materials, that partition of the dopant between grain boundary and lattice solid solution deviates from the McLean equation. They observed for a constant dopant concentration that the dopant grain boundary concentration increases linearly with increasing grain size. They concluded that the interaction of the dopant in the grain boundary caused the grain boundary to be preferentially saturated and the lattice solid solubility to be reduced.

Bae and Baik have observed that initiation of abnormal grain growth in alumina is related to the saturation of grain boundaries with Si and Ca [16, 17]. Cook and Schrott also studied grain size dependence of Ca segregation to alumina grain boundaries [18]. In the 500 p.p.m. Y doped alumina, Gruffel and Carry have observed that there exists a critical grain size at which the grain boundary Y concentration is saturated, and that the alumina grain growth behavior is thereafter modified [19]. It is known that the creep strain rate generally decreases with the increase of the grain size with a power law dependence. However, in 500 p.p.m. Y and 500 p.p.m. Mg co-doped alumina, Lartigue et al. [20] have reported that there is a critical grain size above which the creep strain rate shows a plateau as the grain size increases. Lartigue et al. have postulated that this strain plateau is related to enhanced grain boundary diffusion resulting from dopant grain boundary segregation saturation. Recently, Wang et al. have observed for Nd doped alumina that saturation of the Nd in the alumina grain boundaries promotes abnormal grain growth [21].

These observations lead to a common realization, yet to be systematically investigated, that grain boundary mediated mass transport depends on the dopant grain boundary concentration. It has been established, both experimentally and theoretically, that the level of segregation can vary from grain boundary to grain boundary in the same material [18], but there is little direct information on how the grain boundary structure influences segregation. Since segregation may also change the grain boundary structure, grain boundary structure and segregation are intimately connected. For the case of dilute dopant grain boundary concentration (below the dopant grain boundary saturation concentration), Wang et al. have established the local atomic structural environment around the grain boundary segregated Y and Zr in alumina, which is characterized by first shell ordering [22]. Structural evolution accompanying grain boundary composition changes remains to be established.

Motivated by the above considerations and as a continuation of the previous work [22], we have used high resolution STEM and EXAFS to study the evolution of the local atomic structural features around grain boundary segregated Y as the Y grain boundary concentration increases from dilute to saturated, supersaturated, and finally to equilibrium after YAG phase nucleation. The structural parameters around the Y in alumina grain boundaries (with a grain boundary Y concentration both at saturation and supersaturation) are compared with structural information for Y atoms absorbed on the free surface of α-Al$_2$O$_3$. Finally the stability of the dopant supersaturated grain boundaries is discussed in terms of grain boundary energy.

2. EXPERIMENTAL PROCEDURES

2.1. Materials preparation

The materials were ultra high purity Al$_2$O$_3$ doped with Y$_2$O$_3$ at two levels, 100 and 1000 p.p.m. (Y/Al atomic ratio, and the specimens are referred to as 100Y and 1000Y). Details of processing of the 100Y material have been reported in a previous paper [22]. In the case of 1000 p.p.m. Y doping, the sample was processed via a sol–gel route using Boehmite sol and Y-acetylacetonate precursors to ensure an initial molecular degree of mixing [23]. All powder processing was conducted in a class 100 clean room environment using acid washed containers. Figure 1 shows the 100 p.p.m. Y coated α-Al$_2$O$_3$ powder particles which were calcined in air at 700°C for 8 h to decompose the yttrium nitrate (99.999%, Aldrich Chemical Co, Milwaukee, USA). The inset in Fig. 1 is the equilibrium Wulff morphology for α-Al$_2$O$_3$ based on the surface energies of the lowest index planes [24]. The doped powders were hot-pressed using graphite dies in vacuum at 1450°C and 45 MPa for 30 min. Because the grain boundary area is inversely proportional to the grain size, for a constant initial dopant concentration, the grain boundary dopant concentration may be systematically increased by coarsening of the grain size. The as-hot-pressed 100Y sample was annealed at 1475°C in air for times ranging from 15 to 50 h.

Figure 2 shows the grain size distributions of the as-hot-pressed and 40 h annealed 100Y samples.

2.2. STEM analysis of grain boundary Y concentration

Thin foils for STEM analysis were prepared by standard methods, including diamond wheel slicing, thinning, dimpling, and finally ion beam polishing to perforation. To prevent charging during the analysis, a thin carbon film was evaporated on the surface of the thin foils. Quantitative chemical analysis was performed on a Vacuum Generators HB603 dedicated scanning transmission electron microscope operating at 300 keV with a 30 μm virtual objective aperture. The incident probe size was optimized to less than 1 nm and the beam current was about 0.5 nA. Characteristic Al K_α and Y K_α X-ray lines were measured using an Oxford Instruments windowless Si(Li) EDX detector. Net intensities of these lines were determined by background subtraction and characteristic line peak-integration programs with an Oxford Instruments eXL multi-channel analyzer. EDX spectra were quantified using the Cliff–Lorimer equation [25]. The Y to Al atomic sensitivity factor, $k_{Y/Al}$, was found to be 1.25 by using $Y_3Al_5O_{12}$ powder (Alfa Aesar, Ward

Hill, USA) as a standard. The mass absorption and fluorescence were ignored. In order to convert the measured intensity ratio, I_Y/I_{Al}, to a segregant grain boundary excess amount, a square window method is used [26]. The Y grain boundary excess, Γ_Y, which is defined as the number of atoms of solute present per unit area of grain boundary in excess of the amount of solute that would be present if there were no grain boundary, can be calculated as

$$\Gamma_Y = wn_{Al}k_{Y/Al}\left[\left(\frac{I_Y}{I_{Al}}\right)_{GB} - \left(\frac{I_Y}{I_{Al}}\right)_{BL}\right] \quad (2)$$

where w is the width of the electron beam scan area perpendicular to the boundary in nanometers, n_{Al} is the atomic density of Al in α-Al_2O_3, which is equal to 47.1 Al atoms/nm^3, the subscripts GB and BL represent the grain boundary and bulk lattice, respectively.

2.3. X-ray absorption measurements

X-ray absorption measurements at the K edge of Y were made on Beamline X23A2 of the National Synchrotron Light Source (NSLS) at Brookhaven National Laboratory under normal operating con-
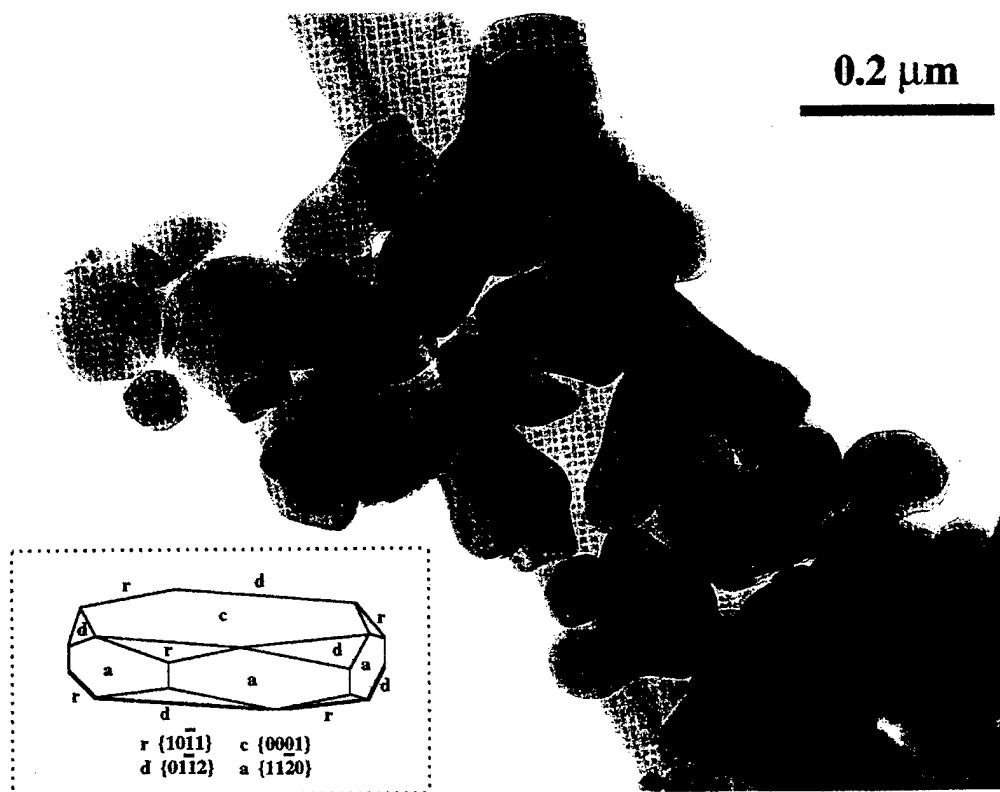

Fig. 1. (a) TEM image showing the α-Al_2O_3 particle morphology and particle size distribution. (b) The predicted equilibrium morphology of α-Al_2O_3 based on the Wulff construction and calculated surface energies [24].

ditions (2.5 GeV, 100–200 mA) and using a Si(311) double crystal monochromator. The spectra were measured in the fluorescence mode for bulk material. The incident beam had a cross-section of $3 \times 20 \, \text{mm}^2$ and intersected with the specimen surface at 45°. An ion chamber was used as the fluorescence detector, positioned such that the detector window centerline also intersected the specimen surface at 45° but was perpendicular to the incident beam direction. In order to reduce statistical errors during data acquisition, for each specimen about 50 spectra were recorded and averaged. The Y coated α-Al₂O₃ powder was also measured in the fluorescence mode using a sample compacted to 56% of theoretical density of α-Al₂O₃.

Samples of cubic Y₂O₃ powder (purity 99.99%, Alfa, Johnson Matthey Company, Ward Hill, USA) were measured in transmission mode, and the data were used as standards for the analysis of data from the doped materials. Samples were prepared by encapsulating the powder between pieces of self-adhesive Scotch Magic tape. As a standard for analyzing secondary phase precipitates in the 1000Y material, bulk polycrystalline Y₃Al₅O₁₂ (YAG), which includes 5 wt% Al₂O₃, was also measured in fluorescence mode, but at a detector grazing angle

Fig. 2. SEM images showing the 100 p.p.m. Y doped alumina (a) as hot-pressed and (b) annealing induced grain growth.

of about 10°. For all the reference samples, at least five spectra were recorded and averaged.

2.4. EXAFS data analysis

The procedures for extracting EXAFS functions and for fitting of the Y–O nearest neighbor shell are the same as those reported in a previous paper [22]. Fitting of the Y–cation next nearest neighbor shell began with a two-shell model structure based on the α-Al₂O₃ structure [Fig. 3(a)]. The model was constructed by substituting a Y atom for an Al atom in α-Al₂O₃ and letting all of the six Al–O $(3 \times 1.85 \, \text{Å}, 3 \times 1.97 \, \text{Å})$ bond lengths in α-Al₂O₃ be increased to the ideal average Y–O bond length in Y₂O₃ $(6 \times 2.284 \, \text{Å})$, while keeping the O to next nearest neighbor Al ion distances the same as those in α-Al₂O₃ and also preserving the α-Al₂O₃ structural frame, as drawn in Fig. 3(b). In this model structure, Y has six O ions as nearest neighbors and seven Al ions as next nearest neighbors. Geometrically, the Y–Al distances are found to be $1 \times 2.89 \, \text{Å}, 3 \times 3.04 \, \text{Å}$, and $3 \times 3.61 \, \text{Å}$. Based on this model and single scattering, the radial distribution function around the substitutional Y ion was calculated using FEFF code. When a Y ion is absorbed on an α-Al₂O₃ grain surface, the Y ion is adjacent to only half of the α-Al₂O₃ bulk lattice. Thus, each Y ion absorbed on the α-Al₂O₃ surface has three Al ions as the next nearest neighbors [Fig. 3(c)]. The scattering amplitudes and phase shift functions were calculated using the FEFF code and were used to fit the Y–cation next nearest neighbor peaks. However, because of difficulties in determining the scaling factor S_0 for the next nearest neighbors, the next nearest neighbor coordination number was not determined.

3. RESULTS

3.1. Y grain boundary segregation behavior

As derived in the Appendix, for the dilute doping regime, the grain boundary concentration of Y in polycrystalline α-Al₂O₃ is proportional to the product of the initial dopant concentration, C_0, and the average grain size, d. Thus, for samples doped initially with different dopant concentrations, or for samples with the same initial dopant concentration but with different grain sizes, the dopant grain boundary segregation behavior can be quantified through the measured grain boundary excess, Γ, as a function of the parameter dC_0.

Figure 4 shows the measured Y grain boundary excess, Γ, as a function of dC_0. Each data point represents the average measured on ~25 boundaries and the error bar represents the standard deviation for the data. The Y grain boundary concentration shows a linear dependence on dC_0 initially, and the slope is approximately equal to that
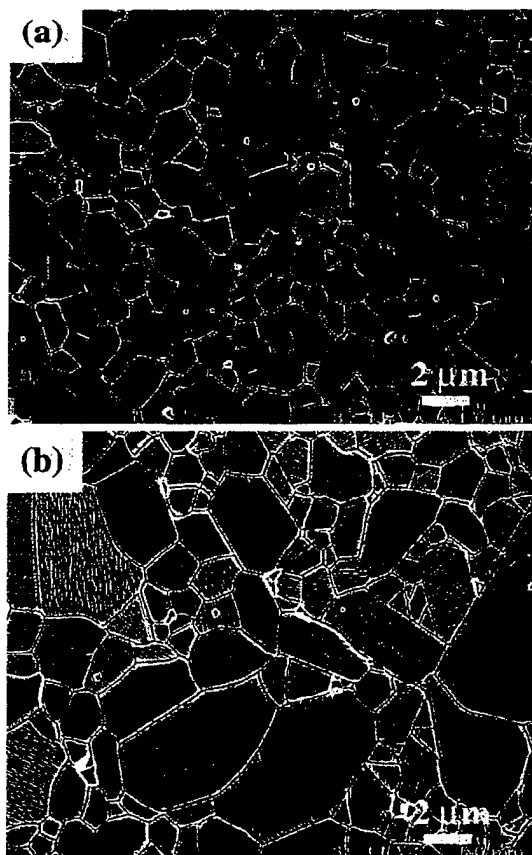
calculated from equation (A4) [the dashed line in Fig. 4(a)]. With increasing dC_0, Γ reaches a peak value of 5.1 ± 0.2 Y atoms/nm², which corresponds to the supersaturation of the grain boundary with the Y ions (region II). In α-Al₂O₃ the cation average density is 47.1 Al atoms/nm³, which corresponds to an Al ion average planar density of 13 Al atoms/nm². The grain boundary Y supersaturation concentration is $\sim 1/2$ equivalent monolayer. Following the supersaturation, Γ drops to a value of $\sim 3.2 \pm 0.8$ Y atoms/nm² and shows no further dependence on dC_0 (region III). It is believed that this constant value of Γ corresponds to the equilibrium concentration of Y in α-Al₂O₃ grain boundaries when the YAG phase co-exists

with the grain boundary segregated Y. This equilibrium grain boundary Y concentration is $\sim 1/4$ equivalent monolayer. The observed Y grain boundary segregation behavior is consistent with the microstructural observations that no YAG precipitates are seen in samples of which the Y grain boundary concentration is in region I or II, while for region III YAG precipitates are visible. Figure 4(b) shows EDX maps of Y distributions in the grain boundaries representing each of the three regions in Fig. 4(a). The boundary representing region III connects with a YAG precipitate. Along this boundary the Y concentration appears to be non-uniform, as evidenced by the discontinuous intensity distribution along the boundary. The
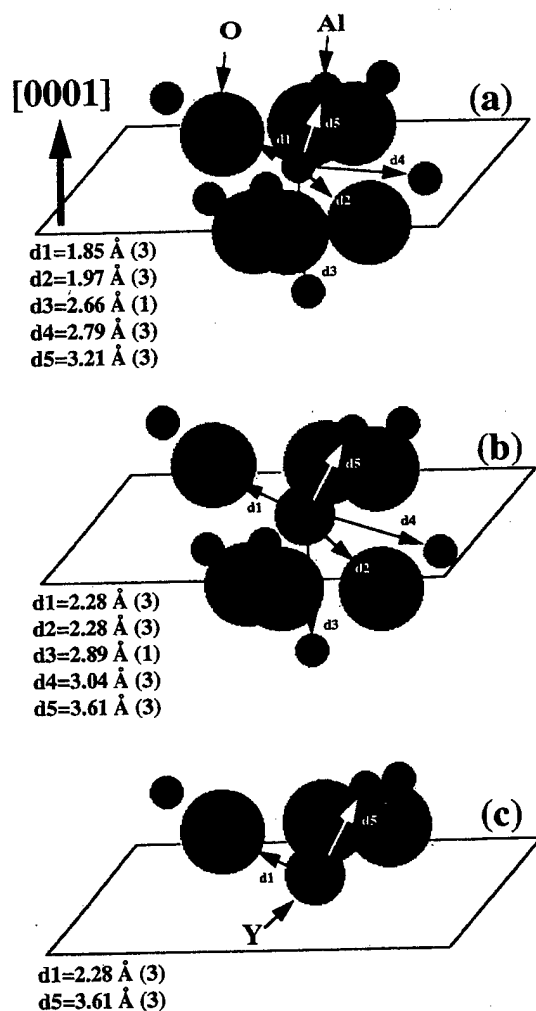

Fig. 3. The atomic arrangements in α-Al₂O₃ show that (a) around Al there are six O ions as nearest neighbors and seven Al ions as next nearest neighbors; (b) substituting Al for Y and making the Y–O distance the same as that in Y₂O₃ while keeping the O–Al nearest neighbor distance the same as that in α-Al₂O₃; and (c) in the case of absorption of Y on the free surface α-Al₂O₃, each Y ion is adjacent only to half of the α-Al₂O₃ bulk lattice, so the Y–Al coordination number is reduced. The free surface is the plane shown below the atoms in (c). The numbers in parentheses represent the number of atoms at each distance.

physical significance of the differences in Y distri-
bution width and intensity in these maps is dis-
cussed in Section 5.

3.2. Fine structural features for grain boundaries supersaturated with Y

Figure 5, as a fingerprint of the standard com-
pounds, shows the experimentally obtained EXAFS
distribution functions around Y in YAG and Y$_2$O$_3$,
which are characterized by large Y–cation next
nearest neighbor peaks. Figure 6 shows the EXAFS
distribution functions of the sample for which the
Y grain boundary concentration is below saturation
(region I of Fig. 4) and of the sample for which the
Y grain boundary concentration is at supersatura-
tion (region II of Fig. 4). Also shown in Fig. 6 is
the calculated EXAFS distribution function for the
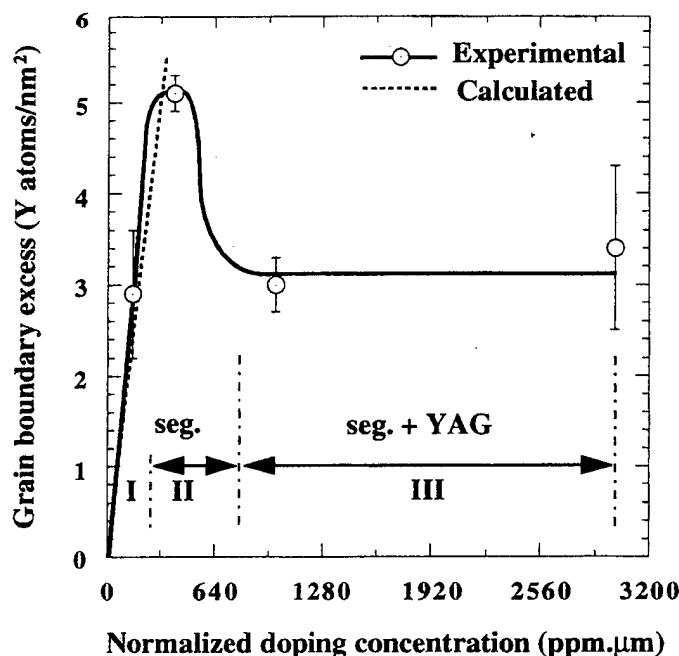
(a)

(b)

Fig. 4. (a) Grain boundary Y excess measured by STEM as a function of the grain size-normalized
doping concentration, which shows three consecutive regions: I, dilute; II, supersaturated; III, equili-
brium. (b) EDX maps showing the Y distribution in a grain boundary which compositionally represents
each region in (a). In the EDX mapping, the electron beam diameter is optimized to 1 nm, and the
mapping area is 160 × 160 nm^2 with a total pixels number of 128 × 128 (seg. stands for segregation).
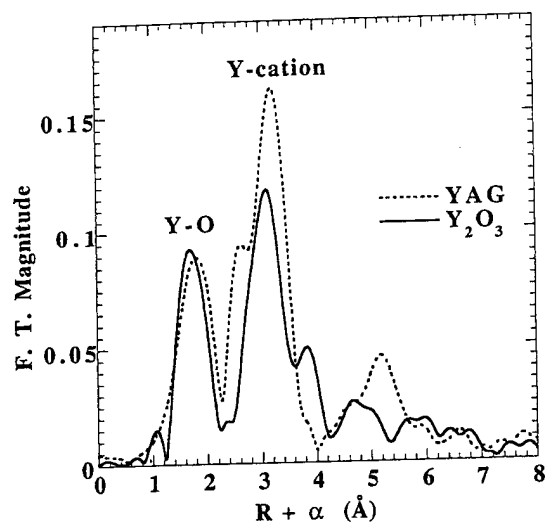
Fig. 5. The experimentally obtained EXAFS distribution functions for YAG and Y_2O_3. Note the significant Y–Y and Y–Al next nearest neighbor peaks.

model structure of Fig. 3(b) which is described in Section 2.4. For clarity, the experimentally obtained EXAFS distribution function from the sample for which the Y grain boundary concentration is at equilibrium with YAG precipitates (region III of Fig. 4) is omitted from Fig. 6, because it is nearly identical to that of the pure YAG phase. Figure 6 clearly reveals that the atomic structural environment around the grain boundary segregated Y depends on the Y grain boundary concentration.

For a dilute grain boundary Y concentration (region I of Fig. 4), the Y–O distance is well defined, while the Y–cation shell cannot be clearly identified in the EXAFS distribution functions, in-
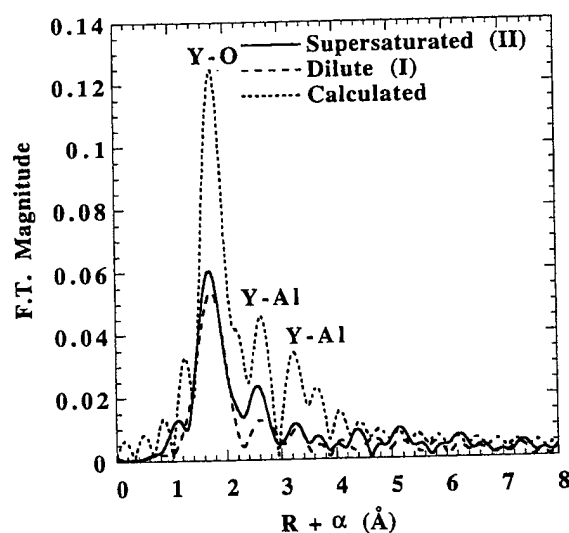
dicating that there is a wide distribution of the Y–cation distances when averaging over all Y sites. This implies that when Y is dilutely segregated at the α-Al₂O₃ grain boundary, atomic ordering around the Y ion is limited to the first shell (the nearest neighbor shell ordering). As the grain boundary Y concentration increases gradually from dilute to saturated and finally to supersaturated (regions I and II of Fig. 4), the most significant feature which evolves in the distribution function is the Y–cation peak, which becomes obviously identifiable, and which, qualitatively, follows the features calculated according to the model structure of Fig. 3(b). Quantitative fitting of the Y–O shell reveals that accompanying the Y grain boundary supersaturation, the Y–O nearest neighbor distance shows no substantial change (Table 2), while the Y–O coordination number increases (Table 2). Quantitative fitting of the Y–cation shell gives a Y–cation distance of 3.31 Å (Table 3). The fitted Y–cation shell distance of 3.31 Å does not appear in the compounds expected to form between Y_2O_3 and Al₂O₃ (Table 1). Instead, the fitted Y–cation distance is approximately equal to the average Y–Al distance when Y substitutes for Al in α-Al₂O₃ while relaxing the Y–O distance to that in Y_2O_3, and keeping the O–Al distance the same as that in α-Al₂O₃ [Fig. 3(b)]. These observations suggest that Y grain boundary supersaturation induces an increased fraction of Y to occupy substitutional sites in α-Al₂O₃.

In region III of Fig. 4 the YAG phase has precipitated. The EXAFS distribution function is dominated by the YAG phase. These data were used in
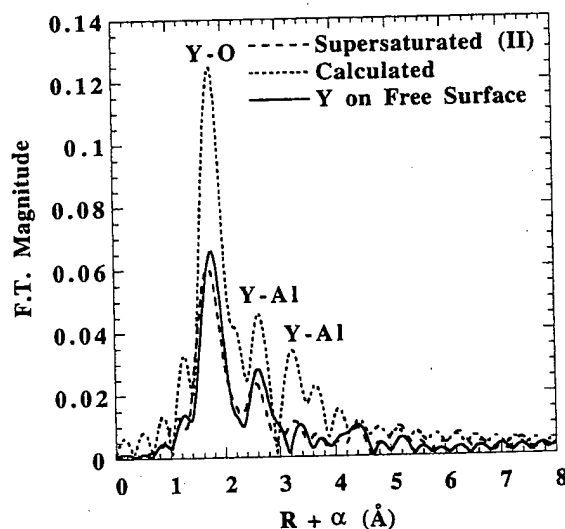

Fig. 6. The EXAFS distribution functions for Y segregated to α-Al₂O₃ grain boundaries at dilute and supersaturated concentration, as well as that calculated according to the model structure of Fig. 3(b).

Fig. 7. The EXAFS distribution functions around Y for the case of Y absorbed on the α-Al₂O₃ powder particle surface (see Fig. 1) and Y segregated to the α-Al₂O₃ grain boundary at a supersaturation concentration, as well as that calculated according to the model structure of Fig. 3(b).

Table 1. Crystallographic data of the model compounds[a]

Composition	Structure	O–Cation × N	Cation–Cation × N	Ref.
$\alpha\text{-}Al_2O_3$	Rhombohedral	Al–O × 6 1.912	Al–Al × 7 2.952	[41]
Y_2O_3	Cubic	Y–O × 6 2.284	Y–Y × 12 3.757	[42]
$Y_3Al_5O_{12}$	Cubic	Y–O × 8 2.351	Y–Al × 10; Y–Y × 4 3.414; 3.677	[43]
$Y_4Al_2O_9$	Monoclinic	Y–O × 7 2.368	Y–Al × 5; Y–Y × 7 3.424; 3.728	[44]
$YAlO_3$	Orthorhombic	Y–O × 12 2.655	Y–Al × 8; Y–Y × 6 3.218; 3.722	[45]

[a] Ionic radii (Å): O^{2-}(6): 1.40; Al^{3+}(6): 0.51; Y^{3+}(6): 0.90, the coordination number is in parentheses [46].

Table 2. Fitting results for the Y–O shell of different Y grain boundary concentrations

	Y concentration	R (Å)	N	σ^2 (Å²)
Grain boundary	Dilute (I)	2.30 ± 0.01	4.2 ± 0.5	0.009 ± 0.001
	Supersat. (II)	2.30 ± 0.01	5.0 ± 0.5	0.01 ± 0.001
	Equi. YAG (III)	2.36 ± 0.01	7.5 ± 0.7	0.008 ± 0.0008
Particle	Surface	2.33 ± 0.01	4.8 ± 0.5	0.008 ± 0.0005

a previous paper to estimate the ratio of the grain boundary segregated equilibrium Y concentration to that which goes to the YAG phase [22].

3.3. Structural environment of Y absorbed on the free surfaces of $\alpha\text{-}Al_2O_3$

Figure 7 shows the EXAFS distribution function around Y when 100 p.p.m. Y was coated on α-Al_2O_3 particle surfaces and annealed at 700°C for 8 h. For comparison the distribution function for Y supersaturated grain boundary [region II in Fig. 4(b)] and that calculated according to the model structure of Fig. 3(b) are also shown in Fig. 7. Qualitatively, when the Y ion is absorbed on the free surfaces of α-Al_2O_3, the distribution function around the Y is similar to that for the Y ion segregated to the α-Al_2O_3 grain boundary at a supersaturated concentration. The EXAFS data indicate that Y absorbed on the free surfaces of α-Al_2O_3 has at least next nearest neighbor order with respect to ions in the subsurface of the α-Al_2O_3 lattice. The fitted Y–O distance is approximately equal to that in Y_2O_3, and the Y–cation distance is about the average of those predicted from the substitutional model [Fig. 3(b)]. Each Y has five O as the nearest neighbors (Tables 2 and 3).

4. DISCUSSION

From EXAFS Wang et al. have established for Y or Zr dilutely segregated to α-Al_2O_3 grain boundaries that the Y and Zr preferentially occupy the grain boundary sites with only short range order (first shell ordering) [22]. The present experimental results show that the range of the structural ordering around Y ions depends on the Y grain bound-

ary concentration, which is direct evidence for the interplay of grain boundary chemistry and grain boundary local structure. Furthermore, the structural environment around Y atoms absorbed on the free surfaces of α-Al_2O_3 is structurally similar to that for Y atoms segregated at α-Al_2O_3 grain boundaries at a concentration corresponding to supersaturation.

To develop a detailed picture of how grain boundary composition may influence grain boundary structure, and vice versa, we first discuss the surface structure of pure α-Al_2O_3, and then the possible structural environment of Y absorbed on the free surface of α-Al_2O_3. Structural evolution around grain boundary segregated Y with respect to the Y grain boundary concentration is then described. In addition, the stability of the Y supersaturated grain boundary is discussed in terms of grain boundary energy.

4.1. The surface structure of $\alpha\text{-}Al_2O_3$

It is well known that the structure of α-Al_2O_3 surfaces differs from that which is expected by truncations of the bulk lattice. Tasker has calculated the structure of pure, clean α-Al_2O_3 surfaces [27]. Tasker has predicted that the type of ion by which a surface is terminated depends on the atomic arrangement in the direction perpendicular to the surface. It was found that a free surface causes

Table 3. Fitting results for the Y–Al shell of Y supersaturated grain boundary and Y on the α-Al_2O_3 particle surface

	Y concentration	R (Å)	σ^2 (Å²)
Grain boundary	Supersat. (II)	3.31 ± 0.01	0.001 ± 0.0005
Particle	Surface	3.31 ± 0.01	0.002 ± 0.0005

relaxation, with the interplanar spacing perpendicular to the surface either expanding or shrinking. For α-Al_2O_3, after the surface relaxation, the surface energies calculated for the five lowest index planes are ordered as [24]

$$\{0001\} < \{10\bar{1}0\} \approx \{10\bar{1}2\} < \{11\bar{2}0\} \approx \{10\bar{1}1\}. \quad (3)$$

The magnitudes of the surface energies determine the equilibrium crystal morphology. It has been predicted that the $\{0001\}$ surface should terminate on Al ions, while the other four listed surfaces should terminate on O ions. Termination of the $\{0001\}$ surface on Al ions is also supported by low-energy electron diffraction (LEED) studies. French and Somorjai [28] and Chang [29] have found that below 800°C, α-Al_2O_3 (0001) has a (1 × 1) structure. Heating the room temperature stable (1 × 1) surface structure in vacuum to > 800°C produces a new ordered 30° rotated ($\sqrt{3} \times \sqrt{3}$) surface structure. Subsequent heating to higher temperature produces an ordered rotated ($\sqrt{(31)} \times \sqrt{(31)}$) surface structure, which is oxygen deficient. However, heating the high-temperature rotated ($\sqrt{(31)} \times \sqrt{(31)}$) surface in oxygen from 1000 to 1200°C restores the low temperature (1 × 1) surface structure. Based on these results, the $\{0001\}$ surfaces of the air atmosphere processed α-Al_2O_3 powder particles are expected to have the stable (1 × 1) structure. The air exposed α-Al_2O_3 particle surfaces are expected to be always covered with oxygen and/or hydroxyls, as schematically drawn in Fig. 8(a). This conclusion is supported by the colloidal behavior of dispersed α-Al_2O_3 suspensions [30].

4.2. Structural environment around Y absorbed on α-Al_2O_3 surfaces

The results in Fig. 7 and the fitted Y–Al distance of 3.31 Å suggest that Y absorbed on the surface of α-Al_2O_3 occupies substitutional Al sites [Fig. 3(b)]. It has been found that absorption of impurities on α-Al_2O_3 $\{0001\}$ surfaces lowers the surface reconstruction temperature [28, 29]. Sol–gel coating of powder particle surfaces with Y and subsequent heating in air at 700°C would likely induce bonding of Y with the surface oxygen. Because Y is much larger than Al, and the overall doping concentration is equal to a surface coverage of only 1/40 monolayer, the Y is not expected to diffuse into the bulk lattice of α-Al_2O_3. The observed long range ordering around the Y ion may be attributed to the ordering of the Y ion with respect to the subsurface α-Al_2O_3 lattice. Because the Y resides on the free surface of α-Al_2O_3, it should be largely unconstrained. This seems consistent with the observation that both the Y–O distance and the Al–O distance are fully relaxed to those in Y_2O_3 and α-Al_2O_3, respectively.

Based on computer simulations, Mackrodt [31]

has predicted that equilibrium coverages of Y on α-Al_2O_3 $\{01\bar{1}2\}$ and $\{10\bar{1}0\}$ surfaces could reach a 1/2 monolayer, which is compositionally equivalent to the compound $YAlO_3$. However, Mackrodt predicted that the $\{0001\}$ surface should not show any tendency for absorbing Y at any temperature above room temperature. The dilute coating of the surface of α-Al_2O_3, ~1/40 equivalent monolayer, would not be expected to lead to the formation of any phase on the surface. The observed Y–cation distance, 3.31 Å, is equal to the average Y–Al distance predicted from the substitutional model of Fig. 3(b).

4.3. Spatial distribution of Y and long range ordering around Y in supersaturated grain boundaries

Comparing with the dilute situation, it is apparent that Y supersaturation in grain boundaries induces longer range ordering around Y ions. This suggests that Y supersaturation leads to an increased fraction of Y ions occupying substitutional cation sites in the α-Al_2O_3 lattice. Obviously, with the increase of Y grain boundary concentration, two types of Y ions may be contributing to the observed increased degree of ordering around Y beyond the nearest neighbor O. The first type are the Y ions which exist as a solute in the α-Al_2O_3 bulk lattice. With the increase of the grain boundary Y concentration, that fraction of Y ions would also be expected to increase, as described by the McLean equation [equation (1)]. The second type is the Y ion that is segregated to the grain boundary but in excess of the Y grain boundary saturation or equilibrium concentration. The segregation behavior shown in Fig. 4 suggests that the second type of contribution is predominantly responsible for the observed long range ordering. The supporting evidence for this is the following.

1. In Fig. 4, with the increase of dC_0, the measured grain boundary Y excess shows a linear dependence on dC_0, and the slope is approximately that calculated from equation (A4). In deriving equation (A4), the solubility of the dopant in the bulk lattice was assumed to be very low and independent of the grain boundary dopant concentration. Therefore, the approximate agreement of the linear slope obtained experimentally would tend to support the validity of these assumptions. Gruffel and Carry have also observed, in Y doped alumina, that the grain boundary Y concentration shows a linear dependence on the average grain size [19].

2. Based on AES study, McCune et al. [8] and Cawley and Halloran [9] have reported that the solubility limit of Y in α-Al_2O_3 lattice is < 10 p.p.m.

3. Both experiments and theory have established that the grain boundary segregation for fine grain-sized polycrystalline materials deviates

from Arrhenius behavior [14, 15]. For attractive interaction of the segregant atoms in the grain boundary, the grain boundary will be preferentially saturated and the lattice solubility therefore reduced.

Based on these considerations, with the increase of Y grain boundary concentration from ~ 3 to ~ 5 Y atoms/nm^2 [see Fig. 4(a)], the structural evolution around the grain boundary segregated Y ion may be suggested as follows.

It would be expected that accommodation of the crystallographic misorientation of two grains will lead to some sites in a grain boundary which are energetically favorable for incorporating oversized dopant ions. The density of the favorable sites in a grain boundary is expected to be determined mainly by the degree of the misorientation of the two grains adjacent to the grain boundary. It has been observed that Y does not segregate either to the basal twin boundary ($\Sigma 3$) or to the rhombohedral twin boundary ($\Sigma 7$) in α-Al₂O₃ [32]. However, Ca segregates to the basal twin boundary in α-Al₂O₃ [33]. At dilute concentrations, the segregants will

preferentially occupy the most favorable grain boundary sites, and filling completely these favorable sites corresponds to saturation of the grain boundary with the dopant. As the number of available Y ions increases, the Y ions apparently enter the near-boundary regions, which contain sites energetically more favorable than those within the bulk lattice. The Y supersaturated α-Al₂O₃ grain boundary may be considered structurally to consist of three layers: a rather disordered core region which accommodates the crystallographic misorientations of the two grains, and a near-boundary layer on each side of the grain boundary core. Yttrium ions in the near-boundary layers are adjacent on one side to α-Al₂O₃ and on the other to the grain boundary core region. Their structural environment may be similar to that for Y absorbed on free surfaces of α-Al₂O₃, as schematically shown in Fig. 8. This three-layer structural model of Y supersaturated grain boundaries provides a qualitative explanation of the experimental results shown in Fig. 7.

The three-layer structural model of the Y supersaturated grain boundaries implies that Y
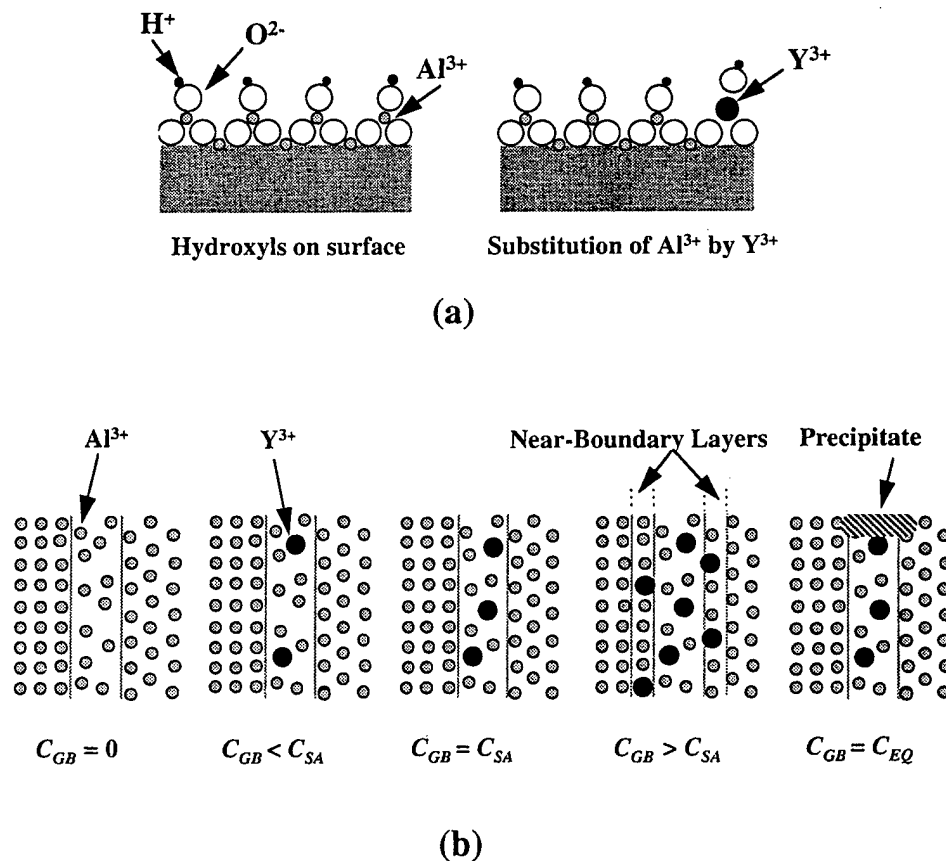

Hydroxyls on surface   Substitution of Al³⁺ by Y³⁺

(a)

$C_{GB} = 0$ $C_{GB} < C_{SA}$ $C_{GB} = C_{SA}$ $C_{GB} > C_{SA}$ $C_{GB} = C_{EQ}$

(b)

Fig. 8. (a) A two-dimensional schematic drawing shows the absorption of Y on the free surface of α-Al₂O₃ and bonding of hydroxyls on the Y ions. (b) Evolution of the atomic structural environment around the Y as the Y grain boundary concentration changes (C_{GB}, dopant grain boundary concentration; C_{SA}, dopant grain boundary saturation concentration; and C_{EQ}, dopant grain boundary equilibrium concentration).

grain boundary supersaturation leads to an increase in the width of the boundary segregation layer in comparison to when boundary Y is at equilibrium concentration. However, it would not necessarily mean that Y grain boundary supersaturation would lead to a widening of the disordered grain boundary core. It may be argued, due to Y having larger ion size than Al, that substituting Al for Y introduces a local distortion or defect around the Y in the near-boundary layers. However, HRTEM observation has not resolved these features. From HRTEM observation, the disordered region of the Y segregated grain boundary is typically only one to two atomic planes wide [10, 32, 34, 35]. However, for these HRTEM observations, it was not determined whether the grain boundary segregant concentration was at supersaturation or the equilibrium concentration. High resolution atomic contrast imaging may be necessary to characterize the dopant concentration dependence of the grain boundary width. It has also been commonly found for liquid phase sintered ceramics that the chemical width of a grain boundary is larger than the structural width determined from HRTEM observation of the structurally disordered region [36, 37].

From Fig. 4, the Y grain boundary supersaturation concentration is ~ 5 Y atoms/nm^2, and the Y grain boundary equilibrium concentration ~ 3 Y atoms/nm^2. With the three-layer model this means at supersaturation $\sim 60\%$ Y ions are in the grain boundary core region, and $\sim 40\%$ Y ions are in the near-boundary layers. Each Y ion in the grain boundary core region has ~ 4.2 O as the nearest neighbors, and the Al ions around the Y are rather disordered [22]. Supposing simple substitution of Y for Al in the near-boundary layers, each of these Y atoms will have six O as nearest neighbors. For Y supersaturated grain boundaries, this would give a Y–O coordination number of $4.2 \times 0.6 + 6 \times 0.4 = 4.9$, which is consistent with the fitted Y–O coordination number for the sample with Y supersaturated at grain boundaries.

The three-layer structural model of Y supersaturated α-Al$_2$O$_3$ grain boundaries is configurationally similar to models established in other systems from computer simulations and experimental observations. The equilibrium glass film of 1 nm in silicon nitride has been characterized as composed of three layers, a disordered core region which is sandwiched between two partially ordered layers in which the SiO$_4$ tetrahedron possesses a certain degree of epitaxial orientation with the silicon nitride grain surface [38]. Keblinski et al. have simulated the fine structural features of an amorphous film sandwiched between two Si grains [39]. They have predicted that partial ordering of the interface between the film and the Si grain surface

would lead the film to be energetically more stable. A diffuse compositional distribution around grain boundaries seems to be a common feature of grain boundaries which are either segregated with a dopant or wet by a glassy film [36]. However, it is not clear how the near-boundary layers affect the grain boundary properties.

4.4. Comparison with computer simulation results

Ching et al. have calculated the structural parameters for the surroundings of a substitutional Y ion in α-Al$_2$O$_3$ using a 120 atom cluster model [40]. They found that the nearest neighbor O atoms around the Y move outward by 8% and the next nearest neighbor Al atoms move inward by 5% of the respective separations in the undistorted lattice. This is in apparent contrast with the present experimental observation that when Y ions substitute for Al ions either on the surface or in the grain boundary region in α-Al$_2$O$_3$, the nearest neighbor O atoms around the Y move outwards by 18%, corresponding to a complete relaxation of the Y–O distance. The next nearest neighbor Al ions around the Y also move outward, instead of inward, such that the O–Al distance remains equal to that in α-Al$_2$O$_3$. In Ching et al.'s calculation, the substitutional Y ion is positioned in the bulk lattice. This may lead to a residual elastic constraint around the Y ion. In the present situation, the Y ions are all situated in the vicinity of the grain boundaries, which may explain the complete relaxation of the Y–O and O–Al bond lengths.

4.5. Stability of the Y supersaturated grain boundaries

The measured Y grain boundary supersaturation concentration is $\sim 1/2$ equivalent monolayer. Assuming that those grain boundary Y ions were indeed distributed on one atomic plane, the Y supersaturated grain boundary would have the stoichiometry YAlO$_3$. However, the grain boundary segregated Y ion is unlikely to reside only on one atomic plane. Also, the EXAFS results for the Y supersaturated grain boundary does not match YAlO$_3$, Y$_3$Al$_5$O$_{12}$, or Y$_4$Al$_2$O$_9$ (see Table 1). Kaplan et al. have observed that Ca segregated in the interface between α-Al$_2$O$_3$ and Al with a Ca excess of $\sim 1/4$ monolayer actually spread over four cation layers [33].

The supersaturation of Y at the α-Al$_2$O$_3$ grain boundaries is related to the nucleation barrier of the YAG phase. The degree of the supersaturation should be determined by the magnitude of the YAG phase nucleation barrier, ΔG. Energetically, a Y supersaturated grain boundary is expected to have a higher grain boundary energy than when the Y grain boundary concentration is at equilibrium.

Based on this consideration, a thermodynamic criterion for nucleation of the YAG phase may be written as:

$$(\gamma_s - \gamma_e) > K\Delta G \qquad (4)$$

where γ_e is the grain boundary energy for Y grain boundary concentration in equilibrium with the YAG phase, and γ_s is the energy for a grain boundary supersaturated with Y ions. K is a geometrical parameter. Nucleation of YAG leads to the depletion of Y in the near-boundary layers. This notion is supported by the STEM mapping of the Y distribution around the grain boundary (Fig. 4). The apparent Y distribution width on the Y map may be affected by both the tilt angle of the boundary plane with respect to the electron beam direction and possible drifting of the specimen during the acquisition of the data. Nevertheless, it is still significant that the boundary which is connected with a YAG precipitate has the narrowest Y distribution width and has an uneven Y distribution along the boundary (Fig. 4). In the study of 1000 p.p.m. Y doped alumina, Gulgun et al. reported that a boundary which connects at each end with a YAG precipitate has no detectable Y level along the boundary [32].

5. CONCLUSIONS

The occupation of α-Al$_2$O$_3$ grain boundaries by Y is characterized by three composition regimes: dilute to saturated, supersaturated, and equilibrium with YAG precipitates. At the dilute concentration, the grain boundary segregated Y ions preferentially occupy sites in the grain boundary core. At supersaturated concentrations, the grain boundary can be divided into three layers, a core layer within which the local structural environment around Y is dominated by short range ordering (nearest neighbor shell ordering), and two near-boundary layers within which the Y ions occupy distorted substitutional sites. The structural environments around the Y ions in the near-boundary layers are similar to the environments for Y absorbed on the free surface of α-Al$_2$O$_3$, which have longer range ordering. The Y–O and O–Al distances around the substitutional Y ion in the near-boundary layer are fully relaxed to those in Y$_2$O$_3$ and α-Al$_2$O$_3$, respectively. The degree of the grain boundary Y supersaturation is determined by the nucleation barrier for the YAG phase. Nucleation of YAG leads to depletion of Y in the near-boundary layers. It is yet to be established how the near-boundary layers affect the grain boundary properties.

REFERENCES

1. Christensen, R. J., Tolpygo, V. K. and Clarke, D. R., *Acta mater.*, 1997, **45**, 1761.
2. Wakai, F., Nagano, T. and Iga, T., *J. Am. Ceram. Soc.*, 1997, **80**, 2361.
3. French, J. D., Zhao, J., Harmer, M. P., Chan, H. M. and Miller, G. A., *J. Am. Ceram. Soc.*, 1994, **77**, 2857.
4. Cho, J., Harmer, M. P., Chan, H. M., Rickman, J. M. and Thompson, A. M., *J. Am. Ceram. Soc.*, 1997, **80**, 1013.
5. Li, Y., Wang, C. M., Chan, H. M., Rickman, J. M., Harmer, M. P., Chabala, J. M., Gavrilov, K. L. and Levi-Setti, R., *J. Am. Ceram. Soc.*, 1999, **82**, 1497.
6. Bruley, J., Cho, J., Chan, H. M., Harmer, M. P. and Rickman, J. M., *J. Am. Ceram. Soc.*, 1999, **82**, 2865.
7. Thompson, A. M., Soni, K. K., Chan, H. M., Harmer, M. P., Williams, D. B., Chabala, J. M. and Levi-Setti, R., *J. Am. Ceram. Soc.*, 1997, **80**, 373.
8. McCune, R. C., Donlon, W. T. and Ku, R. C., *J. Am. Ceram. Soc.*, 1986, **69**, C196.
9. Cawley, J. D. and Halloran, J. W., *J. Am. Ceram. Soc.*, 1986, **69**, C195.
10. Takigawa, Y., Ikuhara, Y. and Sakuma, T., *J. Mater. Sci.*, 1999, **34**, 1991.
11. Cho, J., Wang, C. M., Chan, H. M., Harmer, M. P. and Rickman, J. M., *J. Am. Ceram. Soc.*, submitted.
12. Wang, C. M., Cho, J., Chan, H. M., Harmer, M. P. and Rickman, J. M., *J. Am. Ceram. Soc.*, submitted.
13. McLean, D., in *Grain Boundaries in Metals*. Clarendon Press, Oxford, 1957, pp. 116–149.
14. Terwilliger, C. D. and Chiang, Y. M., *Acta metall. mater.*, 1995, **43**, 319.
15. Colbourn, E. A., Mackrodt, W. C. and Tasker, P. W., *J. Mater. Sci.*, 1983, **18**, 1917.
16. Bae, I.-J. and Baik, S., *J. Am. Ceram. Soc.*, 1997, **80**, 1149.
17. Bae, S. I. and Baik, S., *J. Am. Ceram. Soc.*, 1993, **76**, 1065.
18. Cook, R. F. and Schrott, A. G., *J. Am. Ceram. Soc.*, 1988, **71**, 50.
19. Gruffel, P. and Carry, C., *J. Eur. Ceram. Soc.*, 1993, **11**, 189.
20. Lartigue, S., Priester, L., Dupau, F., Gruffel, P. and Carry, C., *Mater. Sci. Engng*, 1993, **A164**, 211.
21. Wang, C. M., Chan, H. M. and Harmer, M. P., Unpublished research.
22. Wang, C. M., Cargill, G. S. III, Harmer, M. P., Chan, H. M. and Cho, J., *Acta mater.*, 1999, **47**, 3411.
23. Sibold, J., Private communication.
24. Mackrodt, W. C., *Phil. Trans. R. Soc. Lond.*, 1992, **A341**, 301.
25. Cliff, G. and Lorimer, G. W., *J. Microsc.*, 1975, **103**, 203.
26. Alber, U., Mullehans, H. and Ruhle, M., *Ultramicroscopy*, 1997, **69**, 105.
27. Tasker, P. W., in *Advances in Ceramics*, ed. W. D. Kingery, *Structure and Properties of MgO and Al$_2$O$_3$ Ceramics*, Vol. 10. American Ceramic Society, Columbus, OH, 1984, pp. 176–189.
28. French, T. M. and Somorjai, G. A., *J. phys. Chem.*, 1970, **74**, 2489.

29. Chang, C. C., *J. appl. Phys.*, 1968, **39**, 5570.
30. Ducker, W. A., Xu, Z., Clarke, D. R. and Israelachvili, J. N., *J. Am. Ceram. Soc.*, 1994, **77**, 437.
31. Mackrodt, W. C., *Phys. Chem. Minerals*, 1988, **15**, 228.
32. Gulgun, M. A., Putlayev, V. and Ruhle, M., *J. Am. Ceram. Soc.*, 1999, **82**, 1849.
33. Kaplan, W. D., Mullejans, H., Ruhle, M., Rodel, J. and Claussen, N., *J. Am. Ceram. Soc.*, 1995, **78**, 2841.
34. Kaneko, K., Gemming, T., Tanaka, I. and Mullejans, H., *Phil. Mag. A*, 1998, **77**, 1255.
35. Boouchet, D., Dupau, F. and Korinek, S. L., *Microsc. Microanal. Microstruct.*, 1993, **4**, 561.
36. Bobeth, M., Clarke, D. R. and Pompe, W., *J. Am. Ceram. Soc.*, 1999, **82**, 1537.
37. Gu, H., Cannon, R. M. and Ruhle, M., *J. Mater. Res.*, 1998, **13**, 376.
38. Kleebe, H. J., Cinibulk, M. K., Tanaka, I., Bruley, J., Vetrano, J. S. and Ruhle, M., in *Tailoring of Mechanical Properties of Si$_3$N$_4$ Ceramics*, ed. M. J. Hoffmann and G. Petzow. Kluwer Academic, Dordrecht, 1993, pp. 259–274.
39. Keblinski, P., Phillpot, S. R., Wolf, D. and Gleiter, H., *J. Am. Ceram. Soc.*, 1997, **80**, 717.
40. Ching, W. Y., Xu, Y. N. and Ruhle, M., *J. Am. Ceram. Soc.*, 1997, **80**, 3199.
41. Ishizawa, N., Miyata, T., Minato, I., Marumo, F. and Iwai, S., *Acta crystallogr.*, 1980, **B36**, 228.
42. Bonnet, M. and Delapalme, A., *Acta crystallogr.*, 1975, **A31**, 264.
43. Euler, F. and Bruce, J. A., *Acta crystallogr.*, 1965, **19**, 971.
44. Christensen, A. N. and Hazell, R. G., *Acta chem. scand.*, 1991, **45**, 226.
45. Diehl, R. and Brandt, G., *Mater. Res. Bull.*, 1975, **10**, 85.
46. Shannon, R. D., *Acta crystallogr.*, 1976, **A32**, 751.

APPENDIX

A general equation may be derived relating the grain size d, the grain boundary width δ, the dopant grain boundary concentration C_{GB}, the dopant bulk lattice solid solution concentration, C_{BL}, and the overall doping concentration, C_0. For simplicity we use a space filling cube as the basic building block for the bulk structure. Each cube has an edge dimension of d. Assuming that $d \gg \delta$ and that there are no precipitates which contain the dopant ions, from geometry and mass conservation one finds

$$C_{GB} = \frac{d}{3\delta}(C_0 - C_{BL}) \tag{A1}$$

where all concentrations are the fraction of dopant ion with respect to the cation sites in α-Al$_2$O$_3$. Combining equations (1) and (A1) gives

$$C_{GB} = \frac{d}{3\delta + \dfrac{d}{\beta}}C_0. \tag{A2}$$

Written in terms of the dopant grain boundary excess, Γ, this is

$$\Gamma = \frac{2\rho_0 N_{Av}}{W_{Al}} \frac{d\delta(\beta - 1)C_0}{\left(3\delta + \dfrac{d}{\beta}\right)\beta} \tag{A3}$$

where N_{Av} is the Avogadro constant, W_{Al} is the molecular weight of α-Al$_2$O$_3$, and ρ_0 is the theoretical density of α-Al$_2$O$_3$. For Y in α-Al$_2$O$_3$, β has been estimated to be $> 10^4$, and with a grain boundary width of $\delta \sim 1$ nm and an average grain size of $d \sim 1$ μm, equation (A3) can be simplified as

$$\Gamma = \frac{2N_{Av}\rho_0}{3W_{Al}}dC_0. \tag{A4}$$

Equation (A4) is expected to be valid only if there are no second phase precipitates and the dopant has a very low solubility in the bulk lattice.

3.3   Role of Segregating Dopants on the Improved Creep Resistance of Aluminum Oxide

By

J. Cho, C. M. Wang, H. M. Chan, M. P. Harmer,
and J. M. Rickman

PII: S1359-6454(99)00278-5

PERGAMON

ROLE OF SEGREGATING DOPANTS ON THE IMPROVED CREEP RESISTANCE OF ALUMINUM OXIDE

J. CHO, C. M. WANG, H. M. CHAN, J. M. RICKMAN and M. P. HARMER†

Materials Research Center, Whitaker Laboratory, Lehigh University, Bethlehem, PA 18015, U.S.A.

Abstract—Recent studies have demonstrated that p.p.m. levels of rare-earth dopant ions (e.g. Y, La, Nd) wield a beneficial and highly potent influence on the creep properties of alumina. In addition, codoping with ions of disparate sizes (Nd, Zr) resulted in even further enhancement of the creep behavior. In all cases, the dopant ions were found to strongly segregate to grain boundaries. Creep rates were not influenced by the presence of second phase precipitates, verifying that the creep improvement is a solid solution effect. In an attempt to clarify the exact mechanism(s) that controls creep behavior of the doped aluminas, various advanced characterization techniques have been applied including: secondary ion mass spectrometry, scanning transmission electron microscopy, orientation image microscopy, and extended X-ray absorption fine structure as well as atomistic computer simulation and studies of the creep kinetics. Although no definitive mechanism has been established, a logical explanation is that outsize ions segregate to more energetically favorable grain boundary sites, and improve creep resistance by blocking a few critical diffusive pathways. This mechanism is sufficiently general that it may be applicable to other ceramic systems. © 1999 Acta Metallurgica Inc. Published by Elsevier Science Ltd. All rights reserved.

Keywords: Oxides; Interface diffusion; Grain boundaries; Segregation; Creep

1. INTRODUCTION

It has been discovered recently that the addition of trace amounts (<1000 p.p.m.) of rare-earth dopants such as yttrium, lanthanum or neodymium, to fine-grained alumina (1–2 μm grain size) can reduce the creep rate by several orders of magnitude [1–3]. In order to fully exploit this opportunity for developing polycrystalline materials with significantly enhanced creep resistance, over the past several years we have been conducting a comprehensive study aimed at elucidating the underlying mechanism(s) associated with this improved mechanical response. This has included kinetic studies of the tensile creep rate as a function of temperature, applied stress, grain size, dopant type and concentration [3, 4]; detailed microstructural and microchemical analyses of grain boundaries using advanced electron microscopy techniques, high resolution secondary ion mass spectrometry (SIMS) and orientation image mapping [5–7]; a study of the atomic structural environments around Y and Zr segregants using extended X-ray absorption fine structure (EXAFS) [8]; atomistic computer simulation of dopant segregation to surfaces and grain boundaries, and calculations of the migration energy for grain boundary diffusion along grain boundaries with and without segregants [9]. The objective of the present work is to assimilate the findings of these earlier component studies, along with other related studies in the literature, with

a view to identify or at least suggest the underlying scientific mechanism involved. What emerges is a clear correlation between creep retardation and the segregation of solute at the grain boundaries. The exact mechanism is still debatable; however, a role involving site blocking of a few critical diffusive pathways is strongly implied. From that it becomes apparent that there is indeed a realistic potential for tailoring materials with superior creep resistance, guided by a mechanism-based approach.

2. CREEP BEHAVIOR

Work by Carry and Mocellin showed that the addition of Y reduced the strain rate during superplastic deformation of fine-grained, MgO-doped alumina [10]. Independently, French *et al.* [1] demonstrated that Y doping resulted in two to three orders of magnitude improvements in the tensile creep behavior of alumina. Since that time, researchers at Lehigh have extended this study to encompass a wide range of both singly doped, and codoped systems. The specimen preparation and testing procedures have been described in detail elsewhere [1–3], and hence will only be mentioned briefly here. It should be noted, however, that ultrahigh purity starting powders were used throughout, and extreme care was taken to avoid the introduction of impurities (aside from the intended dopant ions). Dog-bone shaped specimens were machined from fully dense, hot-pressed billets. Tensile creep tests were undertaken under various temperatures

---

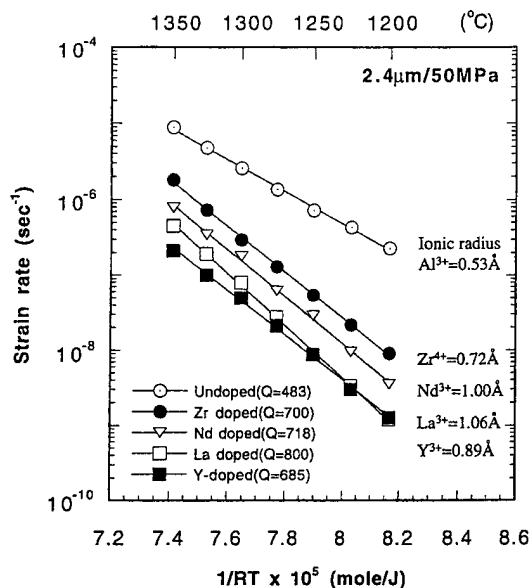†To whom all correspondence should be addressed.

Fig. 1. Arrhenius plot of normalized steady-state creep rates, showing the influence of dopant size on the tensile creep rate for various dopant systems. The plots were normalized to a 2.4 μm grain size. Q is the activation energy (kJ/mol).

and applied stresses [2, 11], with the gauge length established by two SiC flags. A laser extensometer was used to measure strain, and the strain rates were determined from a well-defined steady-state creep regime. The most important findings emerging from this work are described in the following.

2.1. Tensile creep of singly doped aluminas

The steady-state creep rates of various singly doped aluminas are shown in Fig. 1. The dopant levels for the various impurity ions were as follows: Zr (100 p.p.m.), Nd (100 p.p.m.), La (500 p.p.m.), and Y (1000 p.p.m.). Note that for the purposes of comparison, the creep rates were normalized to the same value of grain size ($d = 2.4$ μm) using a grain size exponent of 3. (Experimental results supporting the validity of this procedure are discussed in detail in Section 2.4.) It can be seen that compared to undoped alumina, the creep rates of the Y-, Nd-, and La-doped specimens were reduced by almost two to three orders of magnitude [1–3]. This is a dramatic enhancement in creep resistance, especially considering that earlier studies in the literature have all reported that dopant ions either *increased* the creep rates in alumina, or had little effect [12, 13].

If one considers the influence of dopant ionic size on the creep data, the results show that although the larger rare-earth ions [Y^{3+} (0.89 Å), Nd^{3+} (1.00 Å) and La^{3+} (1.06 Å)] were more effective in inhibiting creep than Zr^{4+} (0.72 Å), the beneficial effect of the impurity ions appears to saturate. Interestingly (see Fig. 1), all the doped systems exhibited significantly higher activation energies than undoped alumina (483 kJ/mol), with the La-

doped system having the highest value (800 kJ/mol). In undoped alumina, quantitative mechanistic analyses of previous diffusional creep and sintering studies have concluded that oxygen grain boundary diffusion is much faster than either aluminum grain boundary diffusion or oxygen lattice diffusion [14]. It has been further concluded that, over the range of temperatures, stresses and grain sizes employed in the current study, boundary aluminum diffusion controls diffusional creep [14]. Furthermore, the value of the activation energy derived from the creep experiments conducted at Lehigh (~468 kJ/mol) [1, 2] was much closer to the published activation energy values for aluminum grain boundary diffusion (~420 kJ/mol) than that for oxygen grain boundary diffusion (~226 kJ/mol) [15, 16]. The issue of whether the creep rate is controlled by grain boundary diffusion or reactions at the interface will be discussed in Section 5.

2.2. Effect of codoping

Given the aforegoing results, where it was shown that beyond a certain size, increasing ionic radius did not result in any further enhancement of the creep behavior, it was decided to test the strategy of codoping [3]. The rationale was based on simple packing considerations, namely that by incorporating ions of differing sizes, it might be possible to block the grain boundary sites more effectively. Figure 2 shows the creep response of alumina codoped with both Nd and Zr (nominally 100 p.p.m. of each dopant ion), and compares it with the corresponding behavior of the undoped and singly doped materials. It can be seen that doping with 100 p.p.m. Zr^{4+} alone, reduced the creep rate by a factor of 15 as compared with undoped alumina. The singly Nd-doped alumina exhibited a
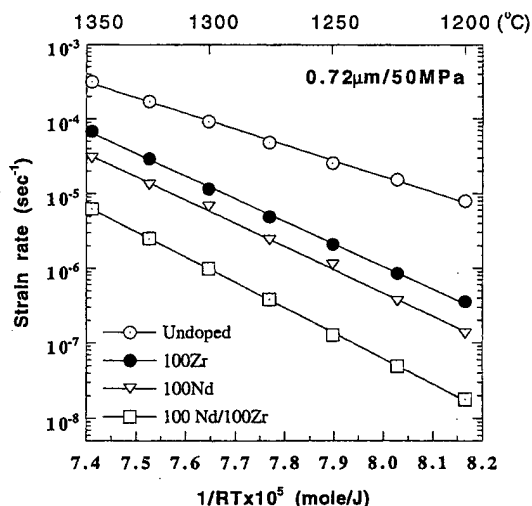

Fig. 2. Arrhenius plot of normalized steady-state creep rates for undoped, 100 p.p.m. Zr-doped, 100 p.p.m. Nd-doped, and 100/100 p.p.m. Nd/Zr-codoped alumina. The plots were normalized to a 0.72 μm grain size.

further reduction in creep rate, but the codoped specimen showed the best creep behavior of all, thus confirming the effectiveness of the codoping approach. In contrast, a Sc/Zr codoped system (1000 p.p.m. Sc/100 p.p.m. Zr) showed similar creep behavior to the singly Zr-doped system [3]. Since the Sc^{3+} ion has a similar ionic radius to Zr^{4+} ($R_{Sc} \sim 0.73$ Å, $R_{Zr} \sim 0.72$ Å), this result is consistent with the premise that a disparity of ionic size is necessary for codoping to have a significant benefit over the singly doped case.

2.3. Solid solution effect

In the original study by French *et al.* [1], it was observed that the 1000 p.p.m. Y-doped alumina contained a small number of YAG ($Y_3Al_5O_{12}$) precipitates. As a result, it was not clear whether the second phase particles played a role in enhancing the creep behavior. To clarify this issue, a series of studies was undertaken whereby the creep rates for alumina containing various dopant ions (Y, La, Nd/Zr) were compared for concentrations both above and below the solubility limit [3, 4]. The creep curves for the La-doped materials are shown in Fig. 3. Note that in this study, the samples were annealed (prior to creep testing) to achieve very similar mean grain size values. As a result, no grain size correction was required in order to directly compare the data. It can be seen that the creep rates for the 100 p.p.m. sample (below solubility limit), and the 500 p.p.m. sample (above solubility limit), are very close. The same general result was obtained in the case of Y doping [4], and Nd/Zr codoping [3]. Taken together, these findings provide very strong evidence that the beneficial influence of rare-earth dopant ions is a solid solution effect, and unrelated to the presence of second phase precipitates. Clearly, it would also be of interest to measure the variation of creep rate with dopant

level for concentrations *below* the solubility limit. Such studies are currently underway.

2.4. Values of inverse grain size exponent (p), stress exponent (n)

In addition to the above described creep studies, values of the (inverse) grain size exponent (p) and stress exponent (n) were evaluated for the various dopant systems. These experiments were deemed pertinent for the following reasons. Firstly, since it was not always possible to creep test samples with the same grain size, an experimentally determined value of the grain size exponent was necessary in order to normalize the creep data for purposes of comparison. Secondly, it was hoped that the values of n and p might yield some insight into the creep mechanism. For the majority of compositions studied (100 p.p.m. Y, 100 p.p.m. La, 100 p.p.m. Nd, 100 p.p.m. Zr), the grain size exponent (p) was determined to be close to 3 [3, 4]. This value is consistent with grain boundary diffusion controlled (Coble) creep. The only exceptions to this result were the Nd/Zr codoped samples (100 p.p.m. Nd/100 p.p.m. Zr, 350 p.p.m. Nd/100 p.p.m. Zr), which showed a grain size exponent of 2. (Note that the above data were derived from creep testing at 1275°C, under an applied stress of 50 MPa.) The change in grain size exponent from 3 (for the Nd and Zr singly doped samples) to 2 (for the Nd/Zr codoped material) was rationalized by arguing that the degree of suppression of grain boundary diffusivity achieved by the codoping was sufficiently great that lattice diffusion (rather than grain boundary diffusion) was now the rate-controlling mechanism [3].

With regard to the stress exponent, however, all the above doped systems exhibited a stress exponent very close to 2 [3, 4]. This result is troubling, in that it is difficult to reconcile with the previously derived value of 3 for the grain size exponent. Instead, $n = 2$ indicates either grain boundary sliding accommodated by the formation of cavities [17], or interface-reaction controlled creep [18]. To date, with the exception of the purely phenomenological equation frequently found in many metal systems by Sherby and Wadsworth [19, 20] which describes superplastic behavior, no theory has been put forward which predicts the observed combination of $n = 2$ and $p = 3$.

3. STRUCTURE AND CHEMISTRY OF GRAIN BOUNDARIES

Even before the discovery of enhanced creep resistance in alumina, it was well known that Y acted as a *reactive element additive*, and improved the oxidation resistance of FeCrTiAl and NiAl alloys [21, 22]. As a consequence, the distribution of Y in polycrystalline alumina had been the subject of a wide variety of analytical techniques [6, 23–29].
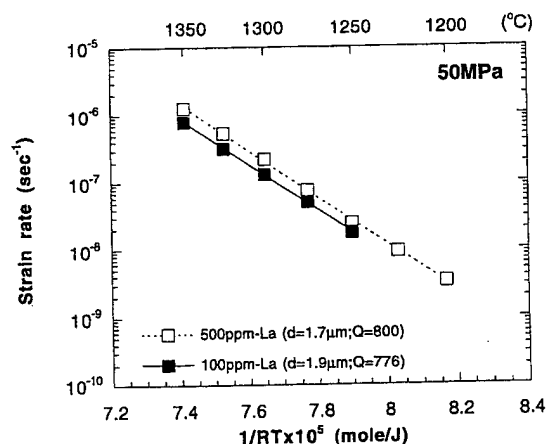

Fig. 3. Comparison of the creep behavior of two La-doped aluminas: 100 p.p.m. La (below solubility limit), 500 p.p.m. La (above solubility limit).

Although the results of these studies consistently indicated that Y segregated to the alumina grain boundaries, what was missing was the ability to correlate directly chemical and microstructural information for a statistically meaningful number of grain boundaries. For example, compositional line profiling using X-ray energy dispersive spectroscopy in the TEM or STEM can probe individual grain boundaries at high spatial resolution, but typically the number of grain boundaries studied is limited. In contrast, the signal from surface techniques such as Auger electron spectroscopy and conventional SIMS is averaged over a large number of grain boundaries, but the link between chemistry and microstructural features is missing. Clearly, in terms of understanding the role of dopant ions on a bulk deformation behavior such as creep, it is desirable to map the segregation behavior over a large number of grains.

It was with this in mind that a collaborative study was undertaken with researchers at the University of Chicago to utilize its unique imaging SIMS capability. The instrument is described in detail in Ref. [30]. Essentially, a focused gallium beam (probe diameter 35 nm) is used to sputter atoms/molecules from the uppermost layers of the specimen surface. Chemical information is derived from analyzing the mass to charge ratio of the secondary ions created by the sputtering process. Two-dimensional elemental distribution maps are subsequently obtained by rastering the beam across the specimen, and recording the signal intensity corresponding to a given chemical species at every position of the beam. In this way, SIMS maps were obtained for both singly doped (Y, La, Nd, Zr) and codoped (Nd/Zr, Sc/Zr) alumina samples [3, 6]. An example of such a map is shown in Fig. 4, which depicts the La map for a sample doped with

Fig. 4. SIMS map showing the La distribution in the as-hot pressed 500 p.p.m. La-doped alumina.

500 p.p.m. La. This result was typical of the singly doped systems, in that the SIMS confirmed that there was localized enrichment of the dopant ion concentration at the alumina grain boundaries [3, 6]. Furthermore, there did not appear to be any gross non-uniformity in segregation behavior, either along a given grain boundary, or from boundary to boundary. SIMS maps of the codoped samples revealed that both dopant ions were segregated to the grain boundaries [3], thus providing support for the contention that codoping may provide a synergistic effect in terms of inhibiting creep.

The advantage of the SIMS mapping lies in its excellent analytical sensitivity (typically at the p.p.m. level), though the lateral resolution is limited by the probe diameter ($\sim$35 nm). In order to gain more insight into the width of the segregation layer, quantitative line profile analyses of grain boundaries in Y- and La-doped alumina were carried out by Bruley *et al.* [5]. These workers found that in both cases, the segregation was confined to a layer thickness less than 3 nm. In addition, the amount of excess solute was found to be similar for both dopants: 9 ± 3 and 10 ± 2 at.%, for Y and La, respectively. Note that in no instance was any evidence of a continuous grain boundary phase detected.

Most recently, high-resolution STEM has been used to generate compositional maps of the dopant concentration in the grain boundary region. The work was carried out in a dedicated STEM (VG HB603) at 300 kV. Very high spatial resolutions can be achieved in this instrument because the probe size is only of the order of 2 nm (even taking into account beam broadening). Figure 5 shows a STEM high-resolution X-ray map taken from 1000 p.p.m. Y-doped alumina, and the corresponding intensity profile. The map clearly shows a distinct segregation layer, which is enriched in Y. The corresponding result for an alumina sample doped with 500 p.p.m. La is shown in Fig. 6. As in the previous case, there is solute enrichment at the grain boundary, but note also the evidence for a corresponding depletion in Al.

Observation of the segregation behavior of the rare-earth ions led Lehigh researchers to propose that the beneficial effect on creep resulted from an inhibition of grain boundary diffusion due to a site-blocking effect. This view is also supported by results from a recent creep study of rare-earth doped alumina by Yoshida *et al.* [31]. An alternative school of thought, however, is that the addition of dopant ions modifies the grain boundary structure. Based on a series of detailed TEM studies of grain boundaries in crept alumina specimens (Mg doped and Mg/Y codoped), Lartigue and co-workers [32–35] postulated that the role of the dopant ions was to limit grain boundary sliding by impeding the accommodation of lattice dislocations. Further, these workers reported evidence that dop-
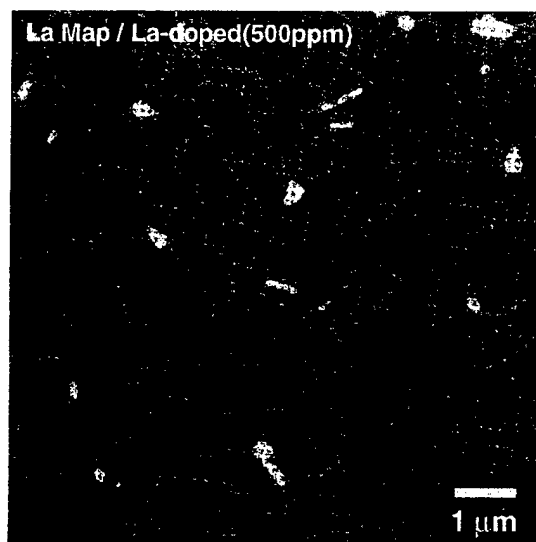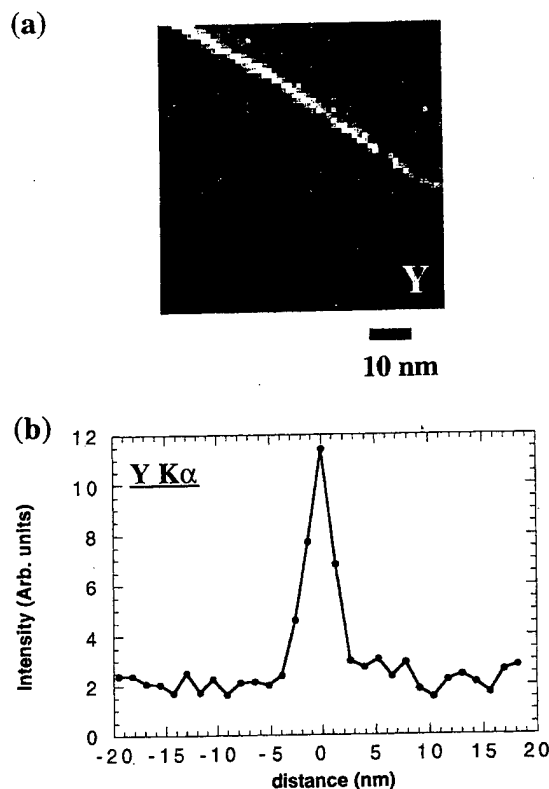
(a)

10 nm

(b)

Fig. 5. STEM high-resolution X-ray map taken from 1000 p.p.m. Y-doped alumina: (a) Y map; (b) the corresponding intensity line profile across the boundary that appears in (a).

ing favors the formation of special boundaries, i.e. coincidence site lattice (CSL) and/or coincidence axis direction (CAD) boundaries, which in turn leads to improved creep resistance [36, 37]. In an effort to distinguish between these two models, Cho and co-workers used electron backscattered Kikuchi diffraction (EBKD) (also called OIM) to characterize the grain boundaries in both undoped and doped alumina [4, 7]. A comparison of the misorientation angle histograms for pure alumina, and alumina doped with 1000 p.p.m. Y is given in Fig. 7. It can be seen that Y-doping does not result in a significant difference in the misorientation distribution. Further, the study showed that the proportion of CSL boundaries in the Y-doped sample was very low (1–5%), and that there was little difference between the doped and undoped alumina. The EBKD results for the Y doping were representative of all the dopant systems tested (La, Nd, Zr, Nd/Zr) in that, for each system, the number of CSL boundaries detected was only a very small fraction of the total and there was no discernible difference in boundary fractions when compared with the undoped alumina. The very low frequency of CSL boundaries in Y-doped alumina was also confirmed by the TEM study of Gülgün *et al.* [38]. These findings provided strong evidence in support of the site-

blocking model, although clearly, subtle modifications of the grain boundary structure due to the presence of the rare-earth ions cannot be completely excluded.

To this end, work is in progress using EXAFS to study the local environment of the dopant ions at the alumina grain boundaries. In brief, preliminary EXAFS analyses of Y_2O_3 and ZrO_2 doped alumina indicate that dopants at the level of 100 p.p.m. are mainly segregated to the alumina grain boundaries. On average Y ions in the grain boundaries are coordinated by four oxygens at a distance of 2.3 Å, which corresponds to the Y–O bond length in cubic Y_2O_3, and Zr ions are coordinated by five oxygens at a distance of 2.14 Å, which is approximately the same as the average Zr–O bond length in monoclinic ZrO_2. From EXAFS, the Y grain boundary saturation concentration is estimated to be 6.0 atoms/nm^2, which is consistent with the estimation from STEM of 4.4 atoms/nm^2 [8].

4. COMPUTER SIMULATION OF SEGREGATION AND TRANSPORT

In light of the results of the mechanical, microstructural and microchemical studies summarized in the previous sections, and the associated conclusion that grain boundaries probably play a dominant

role in the enhancement of creep resistance in doped oxides, we now begin to systematically characterize and correlate grain boundary structure, chemistry and transport in doped aluminas. For this purpose we employ atomistic computer simulation to model idealized, periodically repeated bicrystals containing special, CSL boundaries. These boundaries were selected, though not realistic, due to their computational convenience [9]. In this context, simulation is a particularly useful tool that permits the interrogation of boundary structure and chemistry in a simplified description of a "clean" system with a controlled introduction of impurities. We note, however, that given the idealized nature of the systems under consideration, and the vagueness associated with available interionic potentials, our goal is really to obtain generic information which can then be extrapolated to a relatively broad spectrum of boundaries.

As the details of the simulation methodology and a description of the interionic potential are given elsewhere [9], we merely outline here the salient fea-

tures of the procedure employed in this study. In brief, a charge neutral combination of cations and anions is placed on either a perfect or defected lattice in a spatially periodic rectangular (or rhombic) simulation supercell [39], with ionic interactions described by a combination of empirical pair potentials including: (i) a short-range combination of Born–Mayer and attractive van der Waals potentials [40, 41], (ii) a long-range Coulombic interaction, and (iii) an elastic interaction between ionic cores and shells that reflects the electric polarizability of the lattice [42]. The conditionally convergent nature of the summations required to determine the Coulombic interactions was remedied, as usual, by using an Ewald summation [43]. In the case of grain boundary defects, the height of the simulation cell in the direction normal to the boundary was adjusted in order to eliminate, or at least reduce, extended defect–defect interactions (sometimes via extrapolation), while excess volume was introduced through interfacial gaps when appropriate. After constructing the desired perfect crystal or defect,
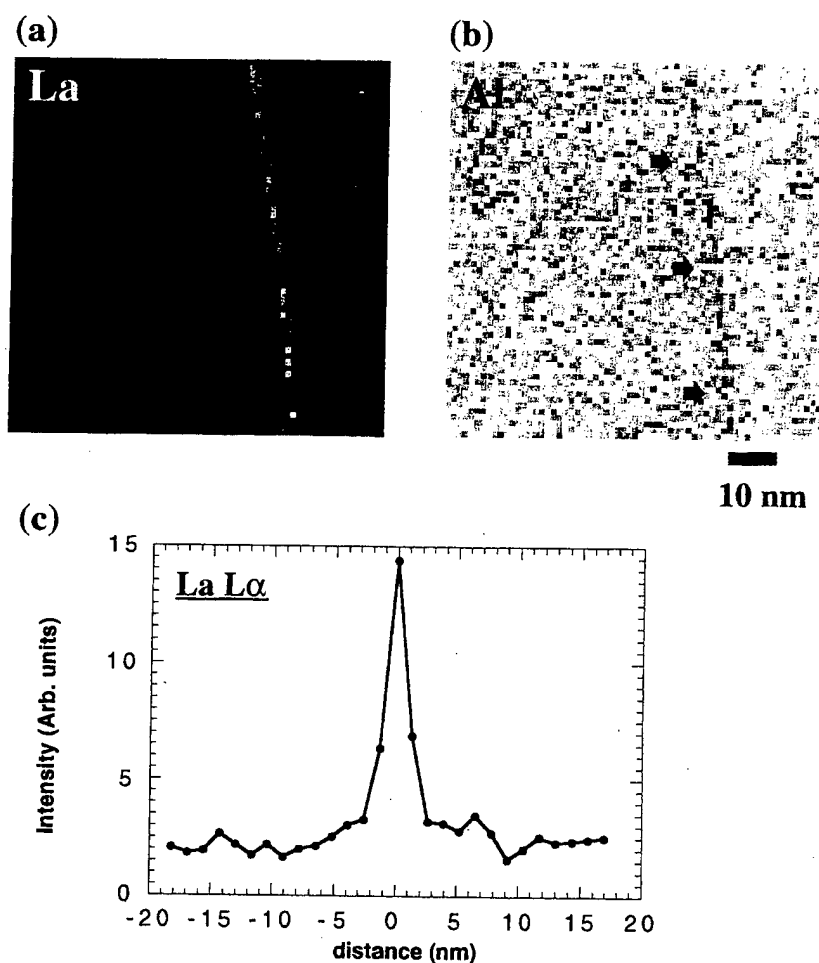
(a)

(b)

10 nm

(c)

Fig. 6. STEM high-resolution X-ray map taken from 500 p.p.m. La-doped alumina: (a) La map; (b) Al map; (c) the corresponding intensity line profile across the boundary that appears in (a).
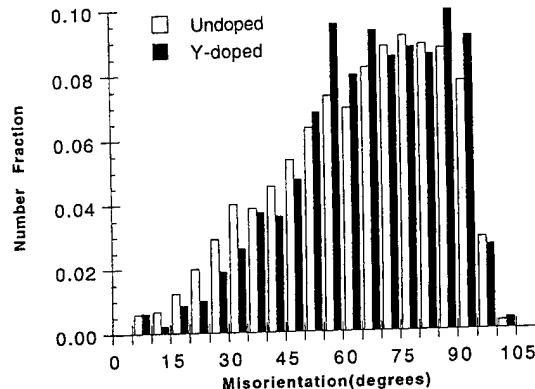
Fig. 7. Misorientation angle histogram for undoped and 1000 p.p.m. Y-doped alumina.

the equilibrium, ground state energy is obtained by employing a conjugate-gradient energy minimization technique [44], wherein the forces calculated at each iteration in the relaxation determine the subsequent configurational evolution of the system. In some cases, we validated our results by comparing these equilibrium energies with those obtained by zero-temperature Monte Carlo (MC) simulation.

An effective strategy for characterizing boundary structure and implicitly, to some degree, boundary chemistry, is to assess the volume associated with grain boundaries. Our approach has been to partition space in a slab of prescribed thickness near a (fully relaxed) boundary using a Voronoi construction [45]. In particular, two measures of interfacial volume were determined, the spatial distribution of cation volume as well as the distribution of void volume. In the cation case, a Voronoi polyhedron can be constructed from the envelope of planes that bisect each line which connects a given cation to its neighboring anions. A similar construction was used for the interstitial case. In both cases, an average "radius" was extracted for each Voronoi cell, yielding a spatially local measure of cell size [9]. As will be seen below, this construction, although complicated by ambiguities in identifying void locations and while not explicitly incorporating local charge considerations, is, nevertheless, quite informative for highlighting potential dopant segregation sites.

For concreteness, we focus here on two prototypical grain boundaries, a Σ3 basal twin, the relatively more ordered structure formed by a 60° rotation about the [0001] axis, and the Σ13 boundary, a relatively disordered structure formed by a 27.8° rotation about the same axis. In order to identify likely segregation sites for oversized dopants, frequency histograms of Voronoi volumes associated with substitutional and interstitial sites for both boundaries were compiled by using the procedure outlined above. The results, presented in Figs 8(a)–(d), indicate, for example, that the effect of the Σ3 boundary is to break the bulk unimodal size distribution of substitutional sites into an essen-

tially bimodal distribution with widely disparate cell sizes. The distribution of interstitial sites is somewhat similar, yet complicated by the fact that both octahedral and (more numerous) tetrahedral sites exist in the bulk region. The lower symmetry of the Σ13 boundary leads to several potential substitutional sites for segregation, some larger than the corresponding bulk sites, as well as some interstitial sites. In addition, by extending this Voronoi analysis to other ionic layers near a given boundary, and calculating a local excess volume per layer [9], it was found that the Σ3 boundary had a relatively localized excess volume, implying that the segregation profile associated with this boundary is likely to be quite narrow. The relative occupancy of these boundary sites by dopant ions in equilibrium can now be estimated by assigning each an energy and associated Boltzmann weight. Indeed, electron microscopy studies have reported essentially no segregation of Y to the basal twin boundary in alumina and some segregation to other boundaries [38], though this observation must be interpreted in view of the fact that the best resolution currently obtainable with these instruments is about 1–2 nm.

It has also been possible to obtain semi-quantitative kinetic information on Al migration at both segregated and unsegregated boundaries via computer simulation. Such information is especially useful given, for example, the paucity of cation boundary diffusion data, and because transport properties in alumina are governed strongly by the presence of impurities [46]. It may also aid in the interpretation of the aforementioned site-blocking model advanced to describe improved creep properties in ceramic oxides. Based on earlier work which characterized bulk cation diffusion [4], we explored the energy surface associated with the migration paths of Frenkel pairs on the Σ3 boundary. This type of defect was selected so that charge compensation effects (i.e. additional vacancies or interstitials) can be ignored. For a given Frenkel pair, three possible migration paths were identified in both the bulk and the twin boundary environments. These paths are illustrated schematically for undoped configurations in Fig. 9 [4]. We note that our approach was somewhat oversimplified in that we did not consider longer range diffusive processes and that we determined only approximate saddle point configurations. This latter approximation was adopted here given the geometric complexities inherent in identifying possible diffusive paths, especially in the presence of dopants. Nevertheless, we believe that the preliminary results presented below are indicative of important trends relating cation diffusion to dopant size.

Generally speaking, the presence of oversized, segregated dopants significantly modify grain boundary diffusion paths. In particular, the migration energies associated with various paths near the twin boundary were found to be lower than the
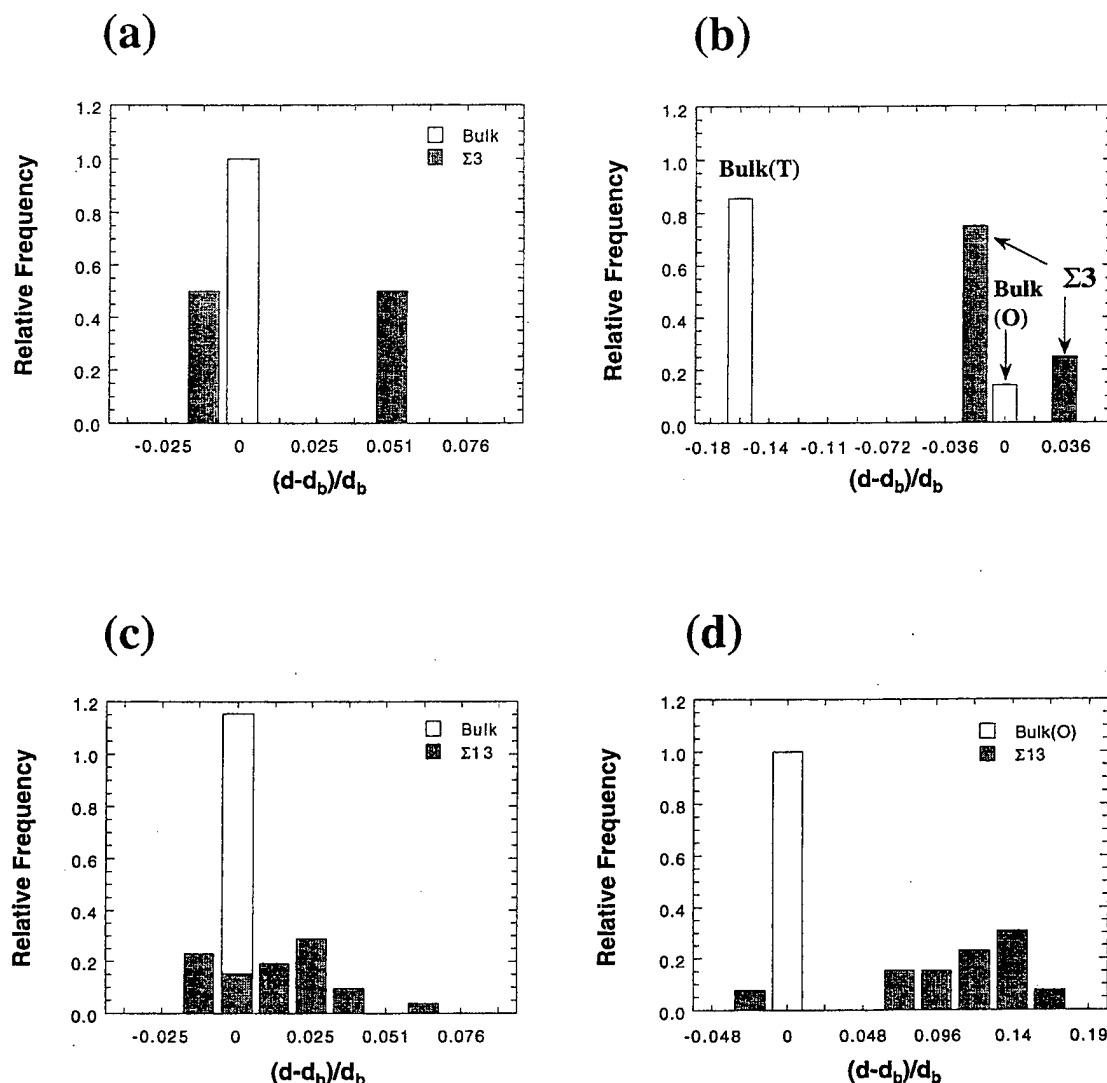
Fig. 8. A Voronoi cell characterization of a boundary plane, as compared to bulk environment: (a) $\Sigma 3$, substitutional; (b) $\Sigma 3$, interstitial; (c) $\Sigma 13$, substitutional; (d) $\Sigma 13$, interstitial. T, tetrahedral site; O, octahedral site; d, Voronoi cell radius; d_b, Voronoi cell radius for the bulk sites.

corresponding bulk paths (by as much as a factor of 5) and, in some cases, increased upon doping with Yb [4]. For example, the energy associated with the fastest unsegregated twin path increased by a factor of 2.75. If, instead, the system were doped with three (larger) La ions, the migration energy became about five to six times higher than the fastest unsegregated path and more isotropic. Further calculations for other boundaries and dopants are currently planned to amplify on these results.

5. DISCUSSION AND CONCLUSIONS

A variety of techniques, both experimental and theoretical have been employed to probe the role of segregating dopants in enhancing the creep behavior of alumina. The first important point which can be made is that because comparable creep behavior

was obtained for dopant levels above and below the solubility limit, the phenomenon is undoubtedly a solid solution effect, and unrelated to the presence of second phase particles. The possible role of the dopant ions in modifying grain boundary properties was highlighted by analytical studies, which revealed that the dopant ions were strongly segregated to the alumina grain boundaries. This result was not unexpected, given their greater size relative to the Al^{3+} ion. In a complementary study, the relation between ionic size and segregation enthalpy was confirmed by atomistic modeling [4]; the results of which underscored the idea that segregation was driven by the elastic strain energy due to size mismatch. Experiments aimed at elucidating the influence of dopant ionic size on the creep behavior revealed that the degree of enhancement saturates at higher ionic radii, suggesting that there is a limi-

tation on the amount of excess solute which can be accommodated at the grain boundaries. This is borne out by the STEM measurements of Bruley *et al.* [5], which showed very similar dopant ion concentrations at the boundaries for Y- and La-doped aluminas. The codoping studies [3] revealed that the addition of two dopant ions of differing size was more beneficial (in terms of the creep behavior) than doping with one type of ion alone. This result was rationalized in terms of greater efficiency of packing for ions with different ionic radii, and again was consistent with the site-blocking role of the dopant ions.

This concept of a volume distribution of cation grain boundary sites, which perhaps could be filled more efficiently by a range of different ions, was explored further by Cho *et al.* using computer simulation [9]. As described earlier (Section 4), these workers showed that for a $\Sigma 3$ boundary, the Voronoi cation and interstitial volumes exhibit an essentially bimodal distribution, with widely disparate sizes. Furthermore, it was generally observed that a significant proportion of the boundary sites was larger than the corresponding bulk sites. The modeling results, therefore, supported the contention that a combination of large and small ions could fill the grain boundary region more efficiently than either ion individually.

From the outset, the contention of the Lehigh researchers was that the primary effect of the rare-earth ions was to inhibit grain boundary diffusion, most likely by 'site blocking' of rapid transport paths. We note that a similar mechanism for diffusive retardation, involving the "clogging" of important boundary paths by segregants, was proposed by others to explain the decrease in boundary diffusivity in Fe that attends Sn segregation [47]. An alternative possibility was raised by the work of Lartigue and Priester [36], however, wherein the deformation behavior was modified because the presence of Mg dopant ions favored the formation of special boundaries. In addition, these workers assessed the role of Y on grain boundary structure in Mg and Y codoped alumina, speculating that the proportion of near CSL boundaries increased after creep deformation [34] as found in metallic systems [48]. In this regard the EBKD results of Cho *et al.* [4, 7] were critical, in that they showed that rare-earth doping had very little influence on either the misorientation distribution, or the frequency of selected CSL boundaries.

As mentioned earlier in Section 2.4, the experimental values of the stress exponent ($n \sim 2$) and (inverse) grain size exponent ($p \sim 3$) are difficult to reconcile, in that they predict different rate-controlling mechanisms. Such apparent contradictions, however, are not uncommon in the creep literature, e.g. see Refs [19, 20, 49], and measurements carried out at Lehigh on undoped alumina also showed similar exponent values [1, 4]. Overall, we are per-
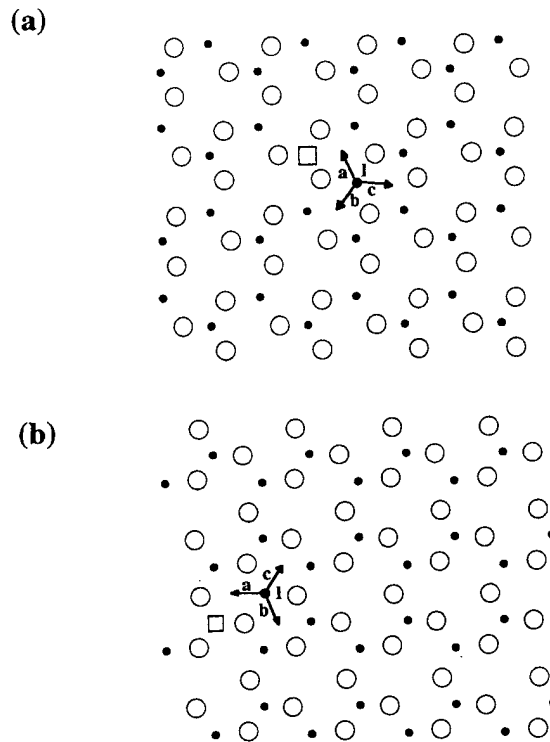

Fig. 9. Schematic diagram for three different migration paths in undoped alumina viewed along the [0001] axis: (a) bulk lattice; (b) (0001) twin boundary plane. (I: interstitial, a, b, c: migration paths, □: vacancy, ○: oxygen, •: aluminum).

suaded that the case for grain boundary diffusion control (vs interface control) is more convincing based on the following. Firstly, the study of Fang *et al.* [50] showed that for Y- and La-doped alumina, the densification kinetics exhibited a grain size exponent of 4, which again is consistent with grain boundary diffusion being the predominant mechanism. Secondly, the observed change in grain size exponent (from $p \sim 3$ to 2) for the singly doped (Nd, Zr) to codoped (Nd/Zr) compositions [3] agrees well with the concept of a transition from grain boundary diffusion to lattice diffusion control. If however, for the sake of argument, the mechanism in the singly doped samples was indeed interface control (with $p = 1$), it would be very difficult to rationalize the subsequent change in grain size exponent. In the absence of definitive evidence to the contrary, therefore, we believe that site blocking of rapid grain boundary diffusion paths by oversized ions is a reasonable model for the observed behavior, and intuitively preferable, because of its more straightforward physical basis.

Clearly, understanding in this area has been impeded by the lack of direct diffusion data on the effect of rare-earth doping on Al^{3+} grain boundary diffusion. However, an ^{18}O tracer study by Le Gall *et al.* [51] suggested that Y doping decreased the diffusivity of oxygen at grain boundaries by two to

three orders of magnitude, raising the question of whether the rare-earth dopant ions have any effect on the *anion* diffusion. Strictly, because the creep rate is determined by the slower ion (on the faster route), any effect on the non-rate-controlling ion would not have an appreciable influence. The implications for oxidation rates, however, which depend on the faster moving species, are far greater; in this regard it would certainly be of interest to extend the simulation work to look into the motion of the oxygen ions.

Taken as a whole, the experimental and theoretical studies paint a reasonably self-consistent picture of outsize ions segregating to more energetically favorable grain boundary sites, and improving creep resistance by blocking a few critical diffusive pathways. As such, the mechanism is not reliant on any material specific defect mechanisms, and would thus seem to be generally applicable to other ceramic systems. The only proviso, however, would be that diffusional creep along the grain boundaries was the rate controlling mechanism. Implicit in the foregoing arguments is that it is the grain boundary diffusion of the Al ions which is being impeded by the rare-earth dopants. In this regard, there are interesting parallels with the reactive element (RE) effect in oxidation. For example, there is evidence that the addition of RE elements such as Y causes a change in mechanism of the scale growth from outward diffusion of aluminum ions, to inward diffusion of oxygen ions [52, 53]. The arguments put forward to explain this behavior are very similar to the one proposed above, namely that the RE cations inhibit the diffusivity of the Al ions at the grain boundary.

Although there is a firm basis for a general, phenomenological understanding of the creep behavior of doped alumina, several outstanding issues remain. For dopant levels below the solubility limit, it is not known whether there is a threshold concentration for creep inhibition, and how the creep behavior depends on dopant concentration. There are also unresolved questions concerning ionic size. The experimental data show both a saturation in the creep effect with increasing atomic size, and the dopant concentration at the grain boundary. Intuitively, however, one might expect a trade-off in terms of more effective blocking by a larger dopant ion, but a lower solubility due to fewer available sites. This in turn suggests that for dopant ions larger than Al^{3+}, there may be a range of ionic size, outside of which, the effect on grain boundary diffusivity is negligible. It is believed that further computer simulation, coupled with ongoing EXAFS studies on the local environment of the dopant ions as a function of concentration and size, may cast light on these issues. There is also the question as to whether a dopant ion which is smaller than the aluminum ion will also be effective in inhibiting creep. Here the lack of suitable trivalent dopant

ions provides an experimental constraint, but fortunately no such limitation exists for the modeling work.

In summary, a comprehensive integrated study has yielded significant progress in understanding the behavior of dopant systems where the creep behavior of alumina is improved. The field, however, is still not at a stage where it would be possible to predict, for a given host system, the optimal dopant ion and dopant level. Many of the obstacles to greater detailed understanding of the segregation and diffusion behavior arise from uncertainties in the structure of general (as opposed to special), grain boundaries in alumina. It is believed that the modeling of such boundaries, and their transport properties, is a fertile and important area for future work.

REFERENCES

1. French, J. D., Zhao, J., Harmer, M. P., Chan, H. M. and Miller, G. A., *J. Am. Ceram. Soc.*, 1994, **77**, 2857.
2. Cho, J., Harmer, M. P., Chan, H. M., Rickman, J. M. and Thompson, A. M., *J. Am. Ceram. Soc.*, 1997, **80**, 1013.
3. Li, Y.-Z., Wang, C., Chan, H. M., Rickman, J. M., Harmer, M. P., Chabala, J. M., Gavrilov, K. L. and Levi-Setti, R., *J. Am. Ceram. Soc.*, 1999, **82**, 1497.
4. Cho, J., Ph.D. thesis, Lehigh University, 1998.
5. Bruley, J., Cho, J., Chan, H. M., Harmer, M. P. and Rickman, J. M., *J. Am. Ceram. Soc.*, in press.
6. Thompson, A. M., Soni, K. K., Chan, H. M., Harmer, M. P., Williams, D. B., Chabala, J. M. and Levi-Setti, R., *J. Am. Ceram. Soc.*, 1997, **80**, 373.
7. Cho, J., Chan, H. M., Harmer, M. P. and Rickman, J. M., *J. Am. Ceram. Soc.*, 1998, **81**, 3001.
8. Wang, C. M., Cargill III, G. S., Harmer, M. P., Chan, H. M. and Cho, J., *Acta Mater.*, in press.
9. Cho, J., Rickman, J. M., Chan, H. M. and Harmer, M. P., *J. Am. Ceram. Soc.*, in press.
10. Carry, C. and Mocellin, A., *Ceram. Int.*, 1987, **13**, 89.
11. Carroll, D. F., Wiederhorn, S. M. and Roberts, D. E., *J. Am. Ceram. Soc.*, 1989, **72**, 1610.
12. Hollenberg, G. W. and Gordon, R. S., *J. Am. Ceram. Soc.*, 1973, **56**, 140.
13. Lessing, P. A. and Gordon, R. S., *J. Mater. Sci.*, 1977, **12**, 2291.
14. Cannon, R. M. and Coble, R. L., in *Deformation of Ceramic Materials, Proc. Symp. on Plastic Deformation of Ceramic Materials*, ed. R. C. Bradt and R. E. Tressler. Plenum Press, New York, 1975, p. 61.
15. Chokshi, A. H. and Langdon, T. G., in *Defect and Diffusion Forum*, ed. F. J. Kedves and D. L. Beke, *Diffusion in Metals and Alloys DIMETA 88*, Vol. 66-9. Sci-Tech Publications, Brookfield, VT, 1990, p. 1205.
16. Paladino, A. E. and Coble, R. L., *J. Am. Ceram. Soc.*, 1963, **46**, 133.

17. Langdon, T. G., *Phil. Mag.*, 1970, **22**, 689.
18. Ashby, M. F. and Verrall, R. A., *Acta metall.*, 1973, **21**, 149.
19. Sherby, O. D. and Wadsworth, J., in *Deformation, Processing, and Microstructure, Proc. ASM Materials Science Seminar*, ed. G. Krauss. American Society for Metals, Metals Park, OH, 1984, p. 355.
20. Sherby, O. D. and Wadsworth, J., *Prog. Mater. Sci.*, 1989, **33**, 169.
21. Przybylski, K., Garratt-Reed, A. J., Pint, B. A., Katz, E. P. and Yurek, G. J., *J. electrochem. Soc.*, 1987, **134**, 3207.
22. Pint, B. A., Martin, J. R. and Hobbs, L. W., *Oxid. Met.*, 1993, **39**, 167.
23. Nanni, P., Stoddart, C. T. H. and Hondros, A. H., *Mater. Chem.*, 1976, **1**, 297.
24. Bender, B., Williams, D. B. and Notis, M. R., *J. Am. Ceram. Soc.*, 1980, **63**, 542.
25. Li, 'C.-W. and Kingery, W. D., in *Structure and Properties of MgO and Al₂O₃ Ceramics*, ed. W. D. Kingery, *Advances in Ceramics*, Vol. 10. American Ceramic Society, Columbus, OH, 1984, p. 368.
26. Loudjani, M. K., Roy, J. and Huntz, A. M., *J. Am. Ceram. Soc.*, 1985, **68**, 559.
27. McCune, R. C., Donlon, W. T. and Ku, R. C., *J. Am. Ceram. Soc.*, 1986, **69**, C196.
28. Tawancy, H. M. and Abbas, N. M., *Scripta metall. mater.*, 1993, **29**, 689.
29. Gruffel, P. and Carry, C., *J. Eur. Ceram. Soc.*, 1993, **11**, 189.
30. Chabala, J. M., Soni, K. K., Gavrilov, K. L. and Levi-Setti, R., *Int. J. Mass Spectrosc. Ion Proc.*, 1995, **143**, 191.
31. Yoshida, H., Ikuhara, Y. and Sakuma, T., *J. Mater. Res.*, 1998, **13**, 2597.
32. Lartigue, S., Priester, L., Dupau, F., Gruffel, P. and Carry, C., *Mater. Sci. Engng*, 1993, **A164**, 211.
33. Lartigue, S. and Priester, L., *J. Am. Ceram. Soc.*, 1988, **71**, 430.
34. Korinek, S. L. and Dupau, F., *Acta metall. mater.*, 1994, **42**, 293.
35. Lartigue-Korinek, S., Carry, C., Dupau, F. and Priester, L., *Mater. Sci. Forum*, 1994, **170–172**, 409.
36. Lartigue, S. and Priester, L., *J. Physique*, 1988, **C5-49**, 451.
37. Priester, L., *Rev. Phys. Appl.*, 1989, **24**, 419.
38. Gülgün, M. A., Putlayev, V. and Rühle, M., *J. Am. Ceram. Soc.*, 1999, **82**, 1849.
39. Rittner, J. D., Udler, D. and Seidman, D. N., *Interface Sci.*, 1996, **4**, 65.
40. Catlow, C. R. W., James, R., Mackrodt, W. C. and Stewart, R. F., *Phys. Rev. B*, 1982, **25**, 1006.
41. Bush, T. S., Gale, J. D., Catlow, C. R. A. and Battle, P. D., *J. Mater. Chem.*, 1994, **4**, 831.
42. Dick, B. G. and Overhauser, A. W., *Phys. Rev.*, 1958, **112**, 90.
43. Allen, M. P. and Tildesley, D. J., *Computer Simulation of Liquids*. Oxford University Press, Oxford, 1987.
44. Press, W. H., Teukolsky, S. A., Vetterling, W. T. and Flannery, B. T., *Numerical Recipes in Fortran: The Art of Scientific Computing*. Cambridge University Press, New York, 1992.
45. Srolovitz, D. J., Maeda, K., Takeuchi, S., Egami, T. and Vitek, V., *J. Phys. F: Metal Phys.*, 1981, **11**, 2209.
46. Cannon, R. M. and Hou, P. Y., in *High Temperature Corrosion and Materials Chemistry*, ed. M. McNallan *et al.* Electrochemistry Society, Pennington, NJ, 1998, in press.
47. Sutton, A. P. and Balluffi, R. W., in *Interfaces in Crystalline Materials*. Clarendon Press, Oxford, 1995, p. 477.
48. Kokawa, H., Watanabe, T. and Karashima, S., *Phil. Mag. A*, 1981, **44**, 1239.
49. Robertson, A. G., Wilkinson, D. S. and Caceres, C. H., *J. Am. Ceram. Soc.*, 1991, **74**, 915.
50. Fang, J., Thompson, A. M., Harmer, M. P. and Chan, H. M., *J. Am. Ceram. Soc.*, 1997, **80**, 2005.
51. Le Gall, M., Huntz, A. M., Lesage, B., Monty, C. and Bernardini, J., *J. Mater. Sci.*, 1995, **30**, 201.
52. Pint, B. A., *Oxid. Met.*, 1996, **45**, 1.
53. Pint, B. A., Garratt-Reed, A. J. and Hobbs, L. W., *J. Am. Ceram. Soc.*, 1998, **81**, 305.

3.4   Modeling of Grain-Boundary Segregation Behavior in Aluminum Oxide

By

J. Cho, J. M. Rickman, H. M. Chan, and M. P. Harmer,

journal

Modeling of Grain-Boundary Segregation Behavior in Aluminum Oxide

Junghyun Cho,* Jeffrey M. Rickman,* Helen M. Chan,* and Martin P. Harmer*,**

Materials Research Center and Department of Materials Science and Engineering,
Whitaker Laboratory, Lehigh University, Bethlehem, Pennsylvania   18015

It is believed that the segregation of oversized dopant ions to grain boundaries in Al_2O_3 hinders grain-boundary diffusion, thereby reducing the tensile creep rate in this system by ~2–3 orders of magnitude. In order to explain this improvement in creep behavior, it is helpful to characterize both the effective cation and interstitial volumes at grain boundaries, because the relative openness of some boundary structures suggests a great accommodation of oversized ions. In this study, the boundary volume is determined by a spatially local Voronoi construction, which highlights cation (Al^{3+}) substitutional sites as well as large interstitial voids. In particular, we examine the spatial distribution of free volume near grain boundaries and, in addition, the dependence of the driving force for segregation on misfit strain in doped Al_2O_3. We interpret our results in light of recent evidence that selective codoping can provide a more efficient means of filling available space near boundaries, thereby further enhancing creep resistance.

I. Introduction

GIVEN their relative mechanical stability and refractory nature, ceramic materials have been used extensively for high-temperature structural applications. However, because of the limited utility of monolithic ceramics in some extreme conditions, ceramic-matrix composites (CMCs) have received considerable attention in recent years. For example, under conditions in which high oxidation resistance at high temperatures is required, ceramic oxides, such as Al_2O_3, are possible candidates for both fiber and matrix materials. In this regime, the creep properties of Al_2O_3 limit its applicability. Given this constraint, it is of interest to identify a subset of Al_2O_3-based oxides having superior creep resistance. We note that significant progress toward this goal occurred when it was discovered that the tensile creep rate of Al_2O_3 decreased by ~2–3 orders of magnitude by the addition of Y_2O_3 or La_2O_3.[1,2]

While the exact mechanism for enhanced creep resistance in these promising doped oxides is not yet known, emerging evidence suggests that grain boundaries play a dominant role in this behavior. One such observation is that oversized cation dopants strongly segregate to grain boundaries. This segregation tendency was highlighted in the work of Li and Kingery[3] and, more recently, in secondary ion mass spectroscopy (SIMS) mapping[4] and dedicated scanning transmission electron microscopy (STEM) studies.[5] Unfortunately, the complexity of grain-boundary geometries, particularly in the presence of dopants, makes it difficult to connect

boundary structure with boundary transport and, ultimately, diffusional creep. Consequently, the interaction between cation (Al^{3+}) grain-boundary diffusion, which is believed to control creep in this study,[1,6,7] and dopant segregants has not been clearly identified. One purpose of this work, therefore, is to characterize systematically and model grain-boundary structure in doped Al_2O_3 in order to connect boundary structure with the propensity for segregation. The long-term goal is to describe grain-boundary transport kinetics in the presence of dopants and, thereby, further elucidate the mechanisms for observed creep behavior.

Specifically, we focus here on the local free volume associated with grain boundaries in order to identify those regions that might accommodate (oversized) segregants. Thus, we use a local Voronoi construction consisting of space-filling polyhedra in the vicinity of grain boundaries under consideration to quantify this volume. For convenience, the grain boundaries selected here are special, coincidence-site lattice (CSL) boundaries with a common [0001] rotation axis, even though we expect to use the results to obtain generic information applicable to a broader spectrum of boundaries. The procedure for generating and relaxing these boundaries is summarized below.

The systematic analysis undertaken here is also useful in understanding certain experimental synergies associated with selective codoping. For example, it has been found that codoping Al_2O_3 with neodymium and zirconium enhances its creep resistance beyond that observed in Al_2O_3 systems singly doped with either ion.[8] This observation has led to the conjecture that, in some circumstances, a combination of large and small ions can fill the grain-boundary region more efficiently than can either ion individually, thereby greatly inhibiting diffusion and creep. In principle, then, the characterization of grain-boundary volume can suggest optimal doping strategies in Al_2O_3 that lead to improved creep resistance.

II. Simulation Methodology

(1) Energetics

Various combinations of interionic potentials are used to describe the energetics of both pure and doped oxides. In particular, the lattice energy, U, of an oxide containing N ions is calculated with a pair potential having two contributions: a short-range combination of Born–Mayer and attractive van der Waals interactions and a long-range Coulombic interaction that together are given by

$$U = \frac{1}{2} \sum_{i=1}^{N} \sum_{\substack{j=1 \\ j\neq i}}^{N} \left[V(r_{ij}) + \frac{z_i z_j}{r_{ij}} \right] \tag{1}$$

where z is the ionic charge, r_{ij} the separation between ions i and j, and $V(r_{ij})$ the short-range interaction

$$V(r_{ij}) = A_{ij} \exp\left(-\frac{r_{ij}}{\rho} \right) - \frac{C}{r_{ij}^6} \tag{2}$$

The empirical parameters A, ρ, and C are determined from fits to perfect crystal data, such as the lattice parameter, elastic constants, and cohesive energy.

Table I. Empirically Fitted Potential Parameters and Shell Constants for α-Al$_2$O$_3$ and M$_2$O$_3$ Systems[†]

Parameter	α-Al$_2$O$_3$	Fe$_2$O$_3$	Yb$_2$O$_3$	Eu$_2$O$_3$	La$_2$O$_3$
$A(+/-)$ (eV)	1460.3	3219.335	991.029	847.868	5436.827
$\rho(+/-)$ (Å)	0.29912	0.2641	0.3515	0.3791	0.2939
$C(+/-)$ (eV · Å^6)	0.0	0.0	0.0	0.0	0.0
$A(-/-)$ (eV)	22764.3				
$\rho(-/-)$ (Å)	0.1490				
$C(-/-)$ (eV · Å^6)	27.879				
Y_+ ($|\vec{e}|$)	1.3830	1.971	−0.278	−0.991	5.149
k_+ (eV · Å^{-2})	92.488	179.58	308.91	304.92	173.90
Y_- ($|\vec{e}|$)	−2.8106				
k_- (eV · Å^{-2})	103.07				

[†]Y = shell charge, k = spring constant. In all cases, cation–cation potential is taken to be purely Coulombic (taken from Catlow *et al.*[9] and Bush *et al.*[29]).

In this study, the potential parameters by Catlow *et al.*[9] are used, as summarized in Table I, wherein only oxygen–oxygen and (repulsive) oxygen–aluminum interactions are considered, and where cutoff radii of 8.0 Å are imposed for both interactions. We note, however, that the long-range, Coulombic potential requires special treatment. Because this interaction falls off rather slowly in space, one can not establish arbitrary cutoff radii, because the summations indicated in Eq. (1) are only conditionally convergent.[10] This problem is remedied, as usual, by using a three-dimensional Ewald summation[11,12] to obtain the relevant contribution to the cohesive energy and associated Madelung constant. We also note the additional complication that a space-charge layer can form near extended defects.[13,14] This effect is not considered explicitly below, because the focus of this study is isovalent cation impurities.

Because defect interactions in ionic crystals depend strongly on the electrical polarization of the lattice, the description above is incomplete, because it does not incorporate the dielectric response of the material. For this purpose, the shell model, used by Dick and Overhauser[15] in their treatment of the dielectric properties of alkali halides, is implemented here. In this idealized model, an ion, *i*, is composed of both core and shell pieces that are connected by an elastic spring contributing an additional quadratic interaction potential

$$V_{sc}^i = \frac{1}{2} k_i (r_{si} - r_{ci})^2 \tag{3}$$

where k_i is a spring constant associated with ion, *i*, and r_{si} and r_{ci} the ionic shell and core positions, respectively. The corresponding shell charges and spring constant are again obtained from the dielectric properties of bulk crystals,[9] as summarized in Table I. While the core and shell positions are taken to coincide initially, the final equilibrium configuration in a defect region often consists of many core–shell displacements, given its lower symmetry relative to the bulk environment, if the associated polarization energy is compensated by decreases in energy elsewhere.

Having evaluated the energy for a given perfect or defect configuration, the equilibrium, ground-state energy is found using the conjugate-gradient technique, wherein forces are calculated at each step in the relaxation.[16] In many cases, we compare these energies with those obtained by zero-temperature Monte Carlo (MC) simulation. These experiments are performed by using a rectangular or rhombic supercell of dimension 1 × 1 × *n*, where *n* is variable, with periodic boundary conditions imposed in three directions (see Table II). As a result, in the case of extended defects, such as surfaces and grain boundaries, a spatially periodic superlattice is constructed, and *n* is adjusted until extended defect–defect interactions have been substantially reduced or eliminated, sometimes using extrapolation. Grain-boundary superlattices have been investigated by others using a similar methodology.[17] The height, *z*, of the simulation cell is also variable, permitting us to adjust the stress component, σ_{zz}. Finally, we are also able to add an excess volume fraction, δ, near an interface by incorporating a gap and then minimizing the total energy with

respect to the distance between two crystals. Given the time-consuming nature of the atomic relaxation procedure, gap optimization is performed, in practice, in the unrelaxed state.

(2) Grain-Boundary Geometry

While grain boundaries can be characterized by various geometric parameters,[18] it is convenient here to classify boundary geometry in terms of a CSL model. The fundamental quantity in this description is the multiplicity, Σ, defined as the volume ratio of the CSL unit cell to that of the original unit cell. For our purposes, Grimmer *et al.*[19] have tabulated all coincidence orientations with multiplicities Σ ≤ 36 for rhombohedral lattices with axial ratios, *c/a*, for corundum-type structures (i.e., 2.696 < *c/a* < 2.765). Among these interfaces, we have selected six basal-plane grain boundaries, namely Σ3, 7, 13, 19, 21, and 31, which are constructed here via rotation around the [0001] axis. From related geometric considerations, one can show that common rotations (in which the same relative orientation of two halves of a bicrystal can be described also by a rotation around the three-fold axis by an angle θ so that $3^{1/2} \tan \theta/2$ is rational)[19] result in the coincidence of a fraction 1/Σ of translation vectors in rhombohedral lattices. We note here that electron backscattered Kikuchi diffraction results for experimentally hot-pressed polycrystalline Al$_2$O$_3$ samples reveal the presence of both Σ3 and Σ13 boundaries, albeit in rather limited proportions.[20]

For the purpose of illustration, Fig. 1 shows the ionic positions associated with a Σ13 boundary, while also highlighting the associated CSL unit cell, and Table II summarizes the salient features of the CSL boundaries used in this study. Finally, we note that, during relaxation to equilibrium, the translations parallel to the boundary plane (i.e., *x*- and *y*-directions) are fixed,[17] and we do not consider explicitly the role of point defects in the possible stabilization of some grain boundaries.[21]

(3) Voronoi Polyhedra

As discussed above, we wish to examine quantitatively the volume associated with grain-boundary regions in the oxides under consideration.[22,23] Our approach has been to partition space in a slab of prescribed thickness near a (relaxed) boundary using a

Table II. Selected CSLs around the [0001] Axis and the Associated 1 × 1 × *n* Simulation Cells Used in This Study

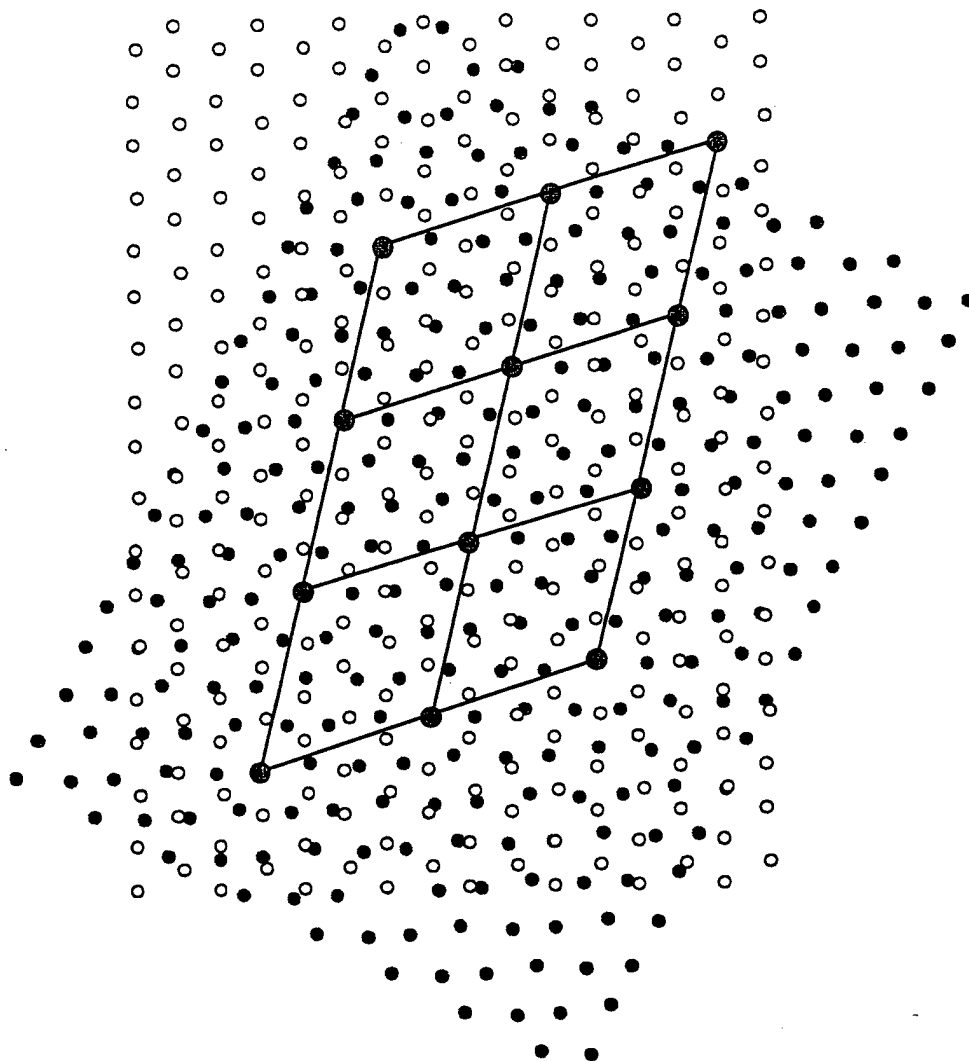| Σ	θ (degrees)	*n*	Number of ions in the simulation cell
3	60.00	4	1920
7	38.21	4	2520
13	27.80	4	3120
19	46.83	2	2280
21	21.79	4	3360
31	17.90	4	7440

Fig. 1. Rotation of two crystals by 27.80° to build a $\Sigma 13$ boundary. This is viewed along the [0001] axis, and the coincidence sites and the corresponding unit cells are indicated. ((O) or (●) = oxygen; (⊛) = coincidence site.)

Voronoi construction.[24,25] In particular, two measures of interfacial volume are determined: the spatial distribution of cation volume and the distribution of void volume, by associating each element of space with either a cation or a void, respectively. In the cation case, a Voronoi polyhedron is constructed from the envelope of planes that bisect each line, which connects the cation to a neighboring anion. Thus, in a bulk environment, each cation is octahedrally coordinated and associated with a cubic Voronoi cell (Fig. 2). Interstices are characterized by a similar procedure. For convenience, in both cases, the average "radius" (the average distance from a cation site to six neighboring faces) of the Voronoi cell is used as a measure of cell size given that the determination of cell volume is rather tedious for general polyhedra.

While this approach is quite useful in that it provides data on the distribution and frequency of possible segregation sites, it is worth noting two limitations. First, this subdivision of space is complicated by ambiguities in identifying void locations in a defect region, by the polarizability of ions in low-symmetry positions and by relatively large ionic relaxations in some cases. Second, it is essentially a geometric description of an interfacial region that does not incorporate explicitly local charge considerations. Nevertheless, as is seen below, the Voronoi construction is quite informative.

### (4) Isovalent Doping of α-Al₂O₃

A more complete picture of the propensity for grain-boundary segregation incorporates the elastic deformation that attends the

introduction of impurities in the boundary region. Such deformations are particularly relevant here, because experimental evidence indicates that oversized isovalent ions, such as yttrium and lanthanum, strongly segregate to grain boundaries, suggesting that the main driving force for segregation is size mismatch (despite reports that yttrium can behave as a donor).[26,27] The strain energy associated with this mismatch has been given in the continuum limit by Eshelby and is proportional to the square of the misfit strain, as given by the square of the difference, Δr, between dopant and host ion radii.[28] In fact, for a related elastically isotropic system, one can write

$$U_s = \frac{6\pi r^3 (\Delta r/r)^2 B}{(1 + 3B/4G)} \qquad (4)$$

where B is the bulk modulus of the solute ion and G the shear modulus of the matrix.

In this study, we consider the interchange of a generic trivalent cation, M, with an aluminum cation. This substitution, which can be performed conveniently in a simulation, might arise in practice, for example, from the reaction

$$\frac{1}{2} M_2O_3 + Al^x_{Al} = M^x_{Al} + \frac{1}{2} Al_2O_3 \qquad (5)$$
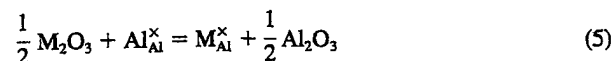
The short-range interaction between dopant and oxygen ions is incorporated in the simulation by using empirical potential parameters obtained by Bush *et al.* for a series of metal oxides, as
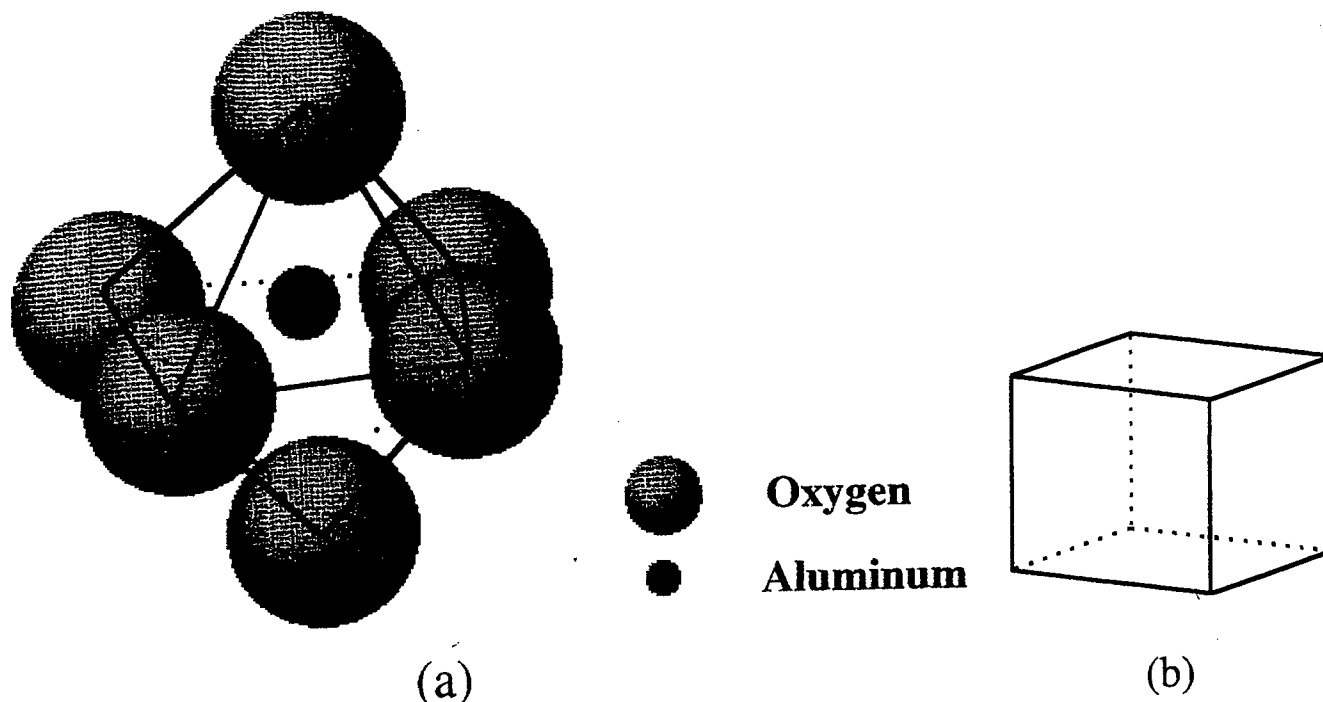
Oxygen

Aluminum

(a)   (b)

Fig. 2. (a) Octahedral environment of oxygen anions for an aluminum cation in bulk. (b) Corresponding Voronoi cell is a cube.

summarized in Table I.[29] Various dopants, ranging in size from iron (0.64 Å) to lanthanum (1.06 Å), are used here. Now, the Langmuir–McLean theory predicts that

$$C_{gb} \approx C_1 \exp\left(-\frac{\Delta H}{kT}\right) \qquad (6)$$

where C_{gb} is the occupation fraction (impurity/host ions) at the grain boundary, C_1 the bulk fraction, and ΔH the segregation enthalpy of interaction between the solute ion and the boundary.[30] We note that, in writing Eq. (6), we have used a dilute solution approximation and also neglected entropic contributions to the free energy. With this definition, then, a negative ΔH implies segregation. Thus, if the strain energy is the main driving force for segregation, ΔH is essentially proportional to

$$-\Delta H = kT \ln\left(\frac{C_{gb}}{C_1}\right) \propto \left(\frac{\Delta r}{r}\right)^2 \qquad (7)$$

In the following section, the validity of this relation is assessed via an identification of favorable boundary sites that most relieve the strain energy. For this purpose, segregation enthalpy is calculated and related to boundary geometry.

III. Results and Discussion

We summarize here the energetic and geometric information obtained from simulation. As indicated above, relaxed, equilibrium structures are obtained primarily via conjugate-gradient energy minimization, and these results are compared, in some cases, with those calculated via the zero-temperature MC method in order to validate the methodology. The data obtained from these two complementary relaxation schemes are presented in Table III for a bulk system, a basal free surface, and an (oxygen-terminated) basal twin boundary. It is worth pointing out that our results for the energies of the perfect crystal, the basal free surface, and point-defect formation energies (such as the Schottky quintet, Frenkel anion, and Frenkel cation) agree very well with previous simulation studies that have used this potential.[9,31]

For the CSL boundaries considered in this study, grain-boundary excess energies (per unit area) are calculated and shown in Fig. 3 as a function of misorientation angle. As is evident from

Table III. Energetic Comparison between Two Energy Minimization Procedures

	Monte Carlo method	Conjugate-gradient method
Perfect lattice (eV/formula unit)	−160.62	−160.62
(0001) Free surface (960 ions) (J/m^2)	2.93	2.92
(0001) Twin boundary (960 ions) (J/m^2)[†]	3.89	3.86

[†]Based on oxygen-terminated twin boundary; twin boundary energy was 3.10 J/m^2 when it was extrapolated to an infinite system to avoid interactions between the two twins.

Fig. 3, the boundary energies lie in the range of ~2.8–3.2 J/m^2, with the Σ3 basal twin boundary having the lowest energy in this series of CSLs. It should be noted that the energy of this Σ3
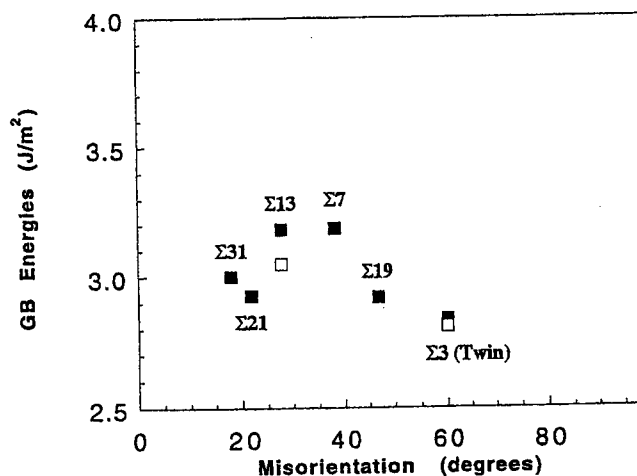

Fig. 3. Grain-boundary energy versus misorientation angle for selected CSLs around the [0001] axis. Twin boundary forms at a misorientation of 60°. ((□) indicates grain-boundary energy with an incorporated gap between two half crystals.)

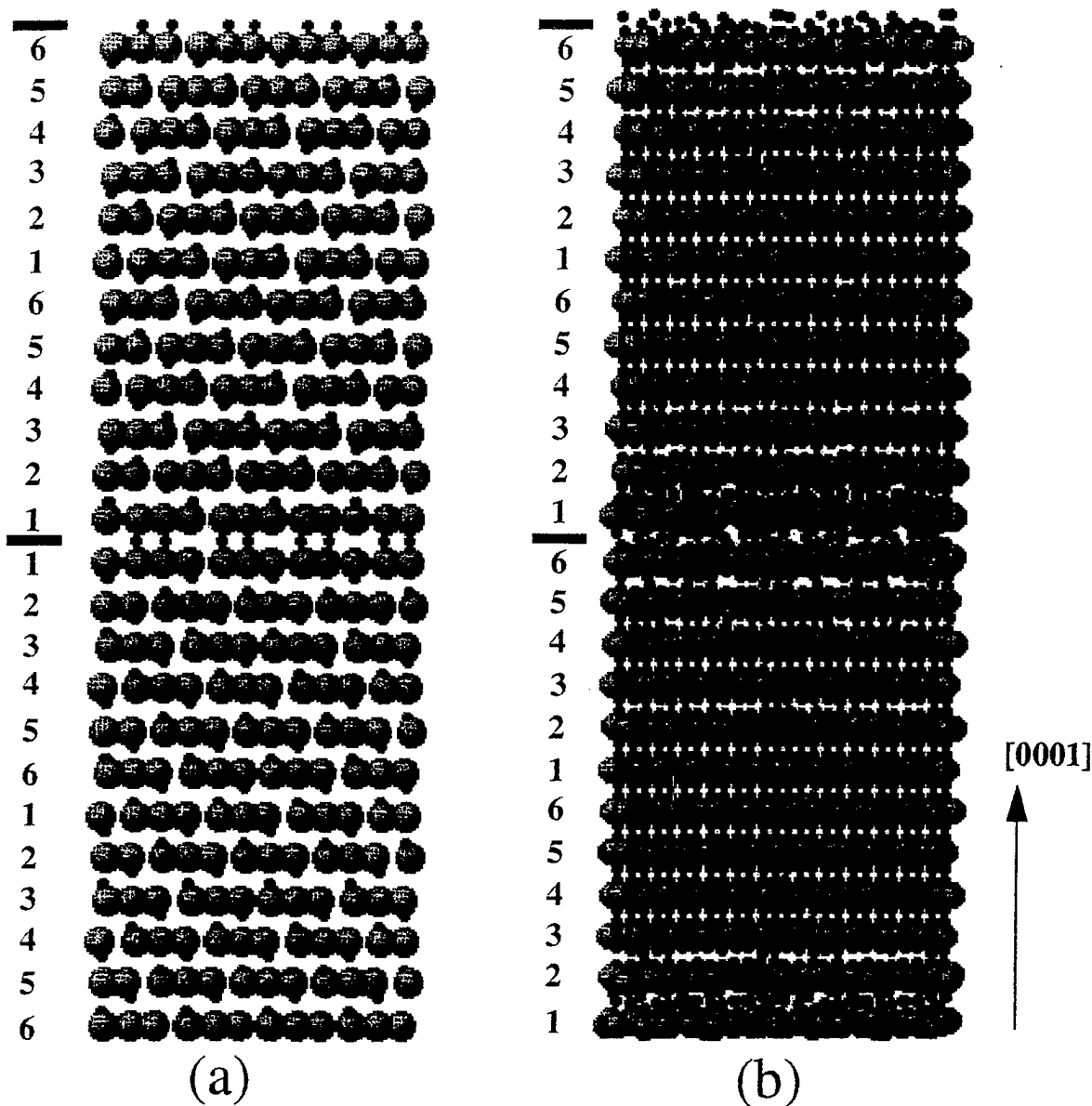**Fig. 4.** Relaxed structures from (a) Σ3 (twin) and (b) Σ13 boundary. Location of boundaries is indicated by a bold line. Number shows the oxygen stacking sequence, and arrow indicates the [0001] direction. ((⊚) = oxygen; (●) = aluminum.)
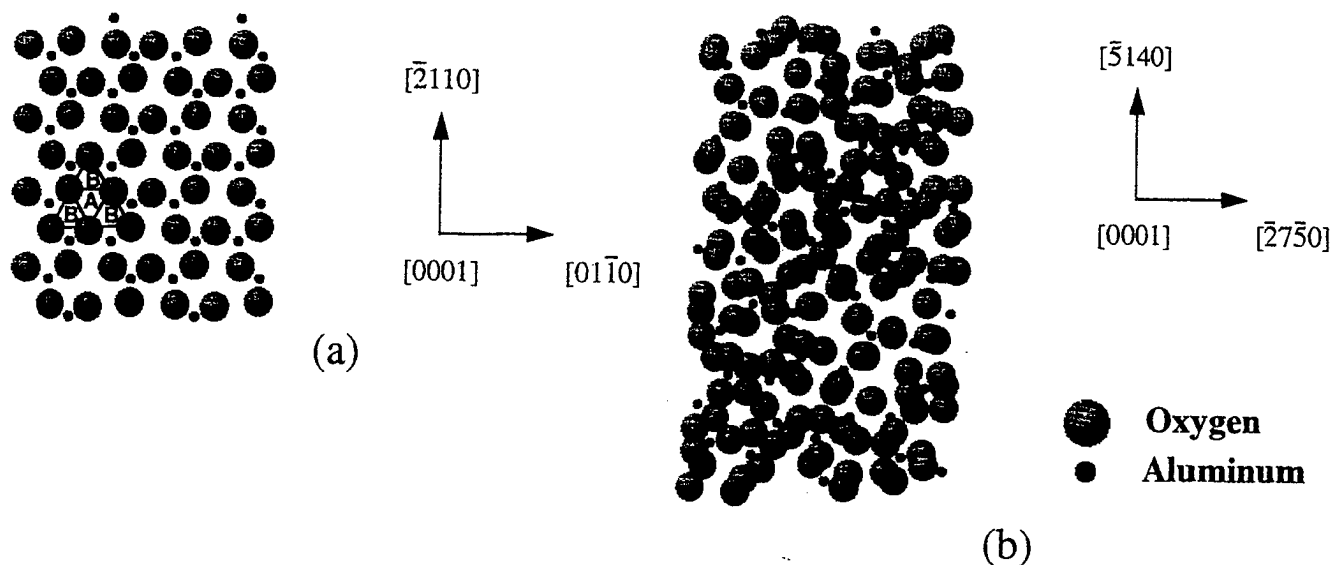

Fig. 5. Same structure as in Fig. 4 focusing on three boundary planes (O–Al–O), as viewed along the [0001] axis: (a) Σ3 boundary voids characterized by the trigonal prisms of A (large) and B (small); (b) Σ13 boundary.
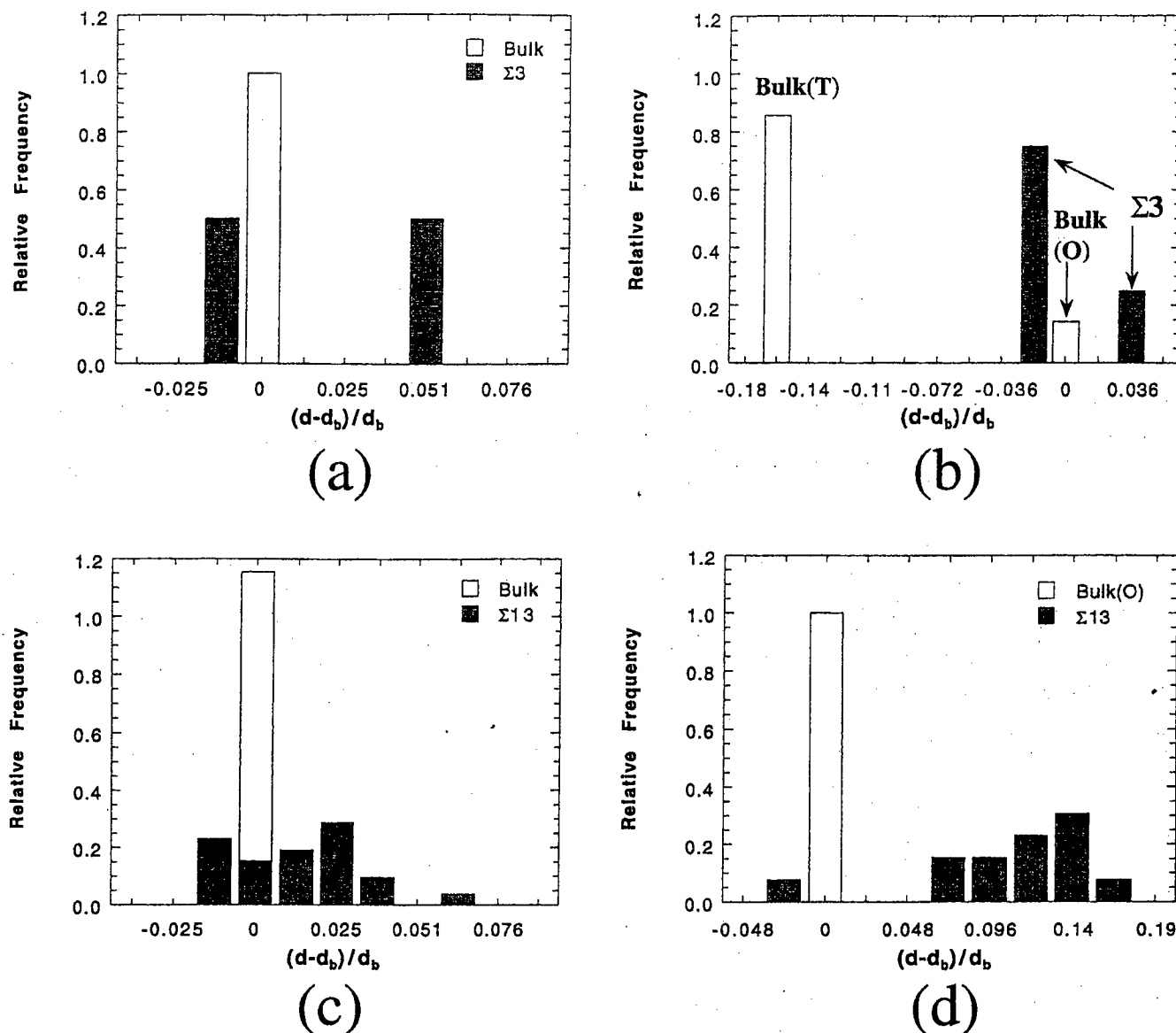
Fig. 6. Voronoi cell characterization of a boundary plane, as compared to bulk environment: (a) $\Sigma 3$, substitutional; (b) $\Sigma 3$, interstitial; (c) $\Sigma 13$, substitutional; (d) $\Sigma 13$, interstitial. (T = tetrahedral site, O = octahedral site, d = Voronoi cell radius, d_b = Voronoi cell radius fo. the bulk sites.)

boundary is lower than that of the corresponding oxygen-terminated basal twin (see Table III), and that, more generally, all of these boundary energies are each less than twice the calculated (0001) surface energy, indicating stability against spontaneous grain-boundary separation.

We note here, as mentioned above, that in-plane (i.e., x and y) boundary translations have not been considered in this study. While such translations can facilitate grain-boundary relaxation in some cases, they are not easily incorporated in this superlattice model, given the two interfaces created per cell. Further, it is often difficult to determine, *a priori*, the optimal displacement vectors associated with relaxation. An alternative to this description is the Mott–Littleton approach, wherein the crystal is divided into region I, surrounding an interface, and an outer region II, modeled as a dielectric continuum.[9] The drawback of this approach is, however, that the usual Ewald summation technique must be modified to account for the loss of periodicity in one direction. Thus, we have adopted the view that the superlattice model is adequate for the segregation studies reviewed here, because, although grain-boundary translation can affect the detailed locations of potential segregation sites, the overall distribution of excess grain-boundary volume is likely to be less sensitive to such translations. The incorporation of grain-boundary sliding into segregation studies is a subject for future work.

Figure 4 shows the corresponding relaxed grain-boundary structures, based for simplicity only on ionic core positions, for both the $\Sigma 3$ and $\Sigma 13$ boundaries. In the former case, the grain-boundary region remains relatively coordinated, with the requisite mirror symmetry across the boundary. By contrast, the latter ($\Sigma 13$) boundary region is more disordered, exhibiting a rumpled structure in the oxygen layers ($\Delta z \approx 1$ Å at plane 1) near the boundary plane. Given this difference in the degree of disorder, these two boundaries serve as prototypes in the discussion below.

Note, however, from Fig. 4(b) that the terminating boundary plane is not easily located, unlike that for the $\Sigma 3$ boundary. Indeed, one might imagine alternative starting configurations, such as, for example, the one obtained by placing the boundary plane between two aluminum layers (i.e., splitting two aluminum layers between oxygen layers). In fact, the relaxation of this configuration yields a different boundary structure with a correspondingly (slightly) higher energy ($\sim 1\%$). This result implies that there can be various metastable local energy minima corresponding to different initial structures. Such minima can, in fact, be artifacts of the simplified potential used here that neglect short-range, cation–cation interactions (see Table I). In any case, we focus on the structure presented in Fig. 4(b), while hoping to identify a global minimum with simulated annealing in future work.
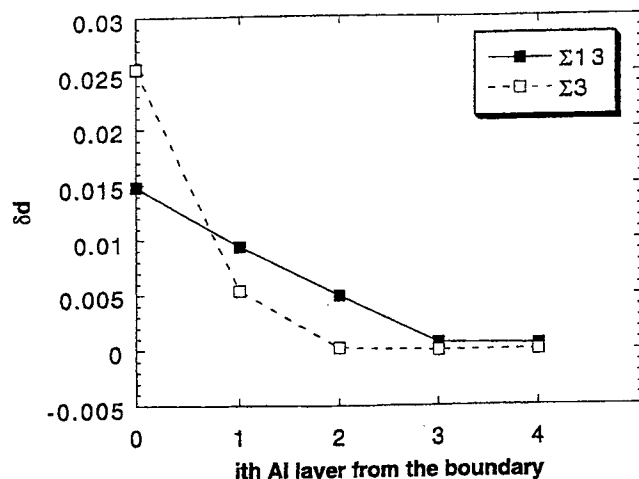
Fig. 7. Excess parameter, δd, a measure of excess volume of large boundary substitutional sites as a function of ith aluminum layer (which increases upon moving away from the boundary). $\Sigma 3$ shows narrow distribution and so approaches the bulk value more quickly.

Fig. 8. Unrelaxed substitutional energy of europium in $\Sigma 13$ boundary as a function of boundary space, showing linear relationship. ($E_{\Sigma 13}$ = unrelaxed substitutional energy at $\Sigma 13$, E_b = unrelaxed substitutional energy in the bulk.)

A somewhat more detailed description of the boundary structure is possible, in some cases, upon viewing several planes along the [0001] axis (Fig. 5). For example, one can view the $\Sigma 3$ boundary interstices in terms of two types of trigonal prisms (located at sites A and B), which have a relative radii of $d/d_b = 1.03$ and 0.986, respectively, where d is the average radius of the trigonal prisms and d_b the radius of bulk octahedral interstitial sites (Fig. 5(a)). However, the disorder associated with the $\Sigma 13$ boundary precludes this simple analysis and leads to several types of interstices of varying size (Fig. 5(b)).

Based solely on geometrical arguments, it is expected that areas of larger interfacial volume can serve as potential sites for dopant segregation. Thus, in order to identify the most likely candidate sites, we compiled a frequency histogram of Voronoi volumes for the $\Sigma 3$ and $\Sigma 13$ boundaries. As is evident in the histogram for substitutional sites (Fig. 6(a)), the $\Sigma 3$ boundary has broken the degenerate, bulk unimodal size distribution into an essentially bimodal distribution of sites with widely disparate sizes. The situation for interstitial sites (Fig. 6(b)) is rather similar, yet complicated by the fact that there are now both octahedral and more numerous tetrahedral bulk sites. It is found that one-fourth of the boundary interstices are larger than these bulk sites. In the case of the $\Sigma 13$ boundary, several potential substitutional sites, many larger than the corresponding bulk sites, are available for segregation in addition to some interstitial sites (see Figs. 6(c) and (d)).

Finally, the Voronoi analysis is extended to layers near each boundary. In Fig. 7, the excess volume available is plotted as a function of ith aluminum layer from the boundary (0 is at the boundary) near the $\Sigma 3$ and $\Sigma 13$ grain boundaries. One measure of this excess volume is the excess parameter, δd, characterized by

$$\delta d = \frac{1}{N} \sum_{i=1}^{N} (d_i - d_b) \times \Theta(d_i - d_b) \qquad (8)$$

where N is total number of sites, d_i (d_b) the average radius of site i (a bulk site), and $\Theta(d_i - d_b)$ a step function. From Fig. 7, it is concluded that, because of the more-localized excess volume associated with the $\Sigma 3$ boundary, segregation is likely to occur near this boundary (within ~2.0 Å), whereas, in the case of the $\Sigma 13$ boundary, a segregant concentration profile likely extends over several layers. Electron microscopy studies have reported essentially no segregation of yttrium to the basal twin boundary, whereas they have detected segregation to other boundaries.[32]

The relevance of the relative excess radius, $(d - d_b)/d_b$, in this segregation study can be seen by examining Fig. 8, which shows the simulation result of unrelaxed substitutional energy (relative to bulk) of europium in the $\Sigma 13$ boundary as a function of $(d - d_b)/d_b$
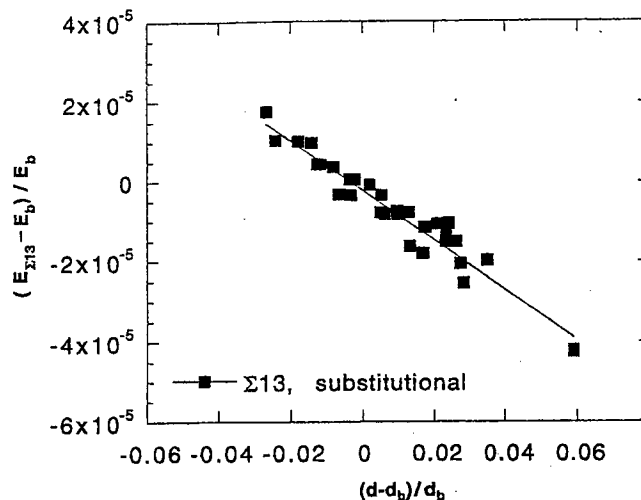
for sites of various sizes. Europium is an intermediate-sized lanthanide ion having a radius of 0.95 Å. The substitutional energy shows a roughly linear relationship with the relative excess radius, indicating the larger volume can more easily accommodate oversized ions. Further, those sites with zero excess radius have nearly zero corresponding excess energies, implying that such sites are essentially bulklike and that the size of the local Voronoi cell is the best indicator of the propensity for segregation. A more complete description must, of course, incorporate ionic relaxation.

Having characterized the volume in boundary regions, we next determine zero-temperature (substitutional) segregation enthalpies, ΔH, for relaxed boundary and bulk sites. Such information can, in principle, be used in an equilibrium statistical mechanical calculation of a segregation profile, although our aim here is only to identify likely segregation sites based on volume and complementary energetic considerations. For this purpose, our results are perhaps best illustrated in the case of the $\Sigma 13$ boundary.

The segregation enthalpy, ΔH, is displayed in Fig. 9 for four dopants (iron, ytterbium, europium, and lanthanum) of varying size as a function of $(\Delta r)^2$ for three types of boundary substitutional sites. These sites, labeled 1, 2, and 3 and ordered based on size, have relative radii, d/d_b, of 1.067, 1.018, and 0.9813, respectively. For type 1 sites, the observed linear relationship suggests that the main driving force for segregation is indeed size mismatch. As the site volume decreases, segregation enthalpy also expectedly increases and is positive for type 3 sites, which are smaller than their bulk counterparts. Similar trends exist for substitutional sites near the boundary. In summary, these results not only indicate which subset of sites are preferred for segregation but also suggest that (1) site exhaustion can lead to a saturation of segregation behavior and that (2) selective codoping schemes can be used to enhance segregation, particularly in the case of the $\Sigma 13$ boundary with its multiplicity of potential sites. The possibility of segregation saturation is consistent with the observation of similar segregation profiles in systems with relatively large ionic impurities, such as yttrium- and lanthanum-doped Al_2O_3,[5] while the advantages of codoping are discussed above in relation to the neodymium-zirconium codoped Al_2O_3 system.[8]

It is of interest to explore the implications of these results for transport processes in ceramic oxides. In particular, it has been shown in preliminary work that the presence of segregating ions near grain boundaries can alter (possibly fast) diffusive paths in interfacial regions.[20,33] We are, in fact, now in the process of correlating these diffusion studies with investigations of the kinetics of creep. Therefore, to the extent that grain-boundary diffusion controls the long-time mechanical response of the material, as exemplified by its creep rate, the propensity for segregation
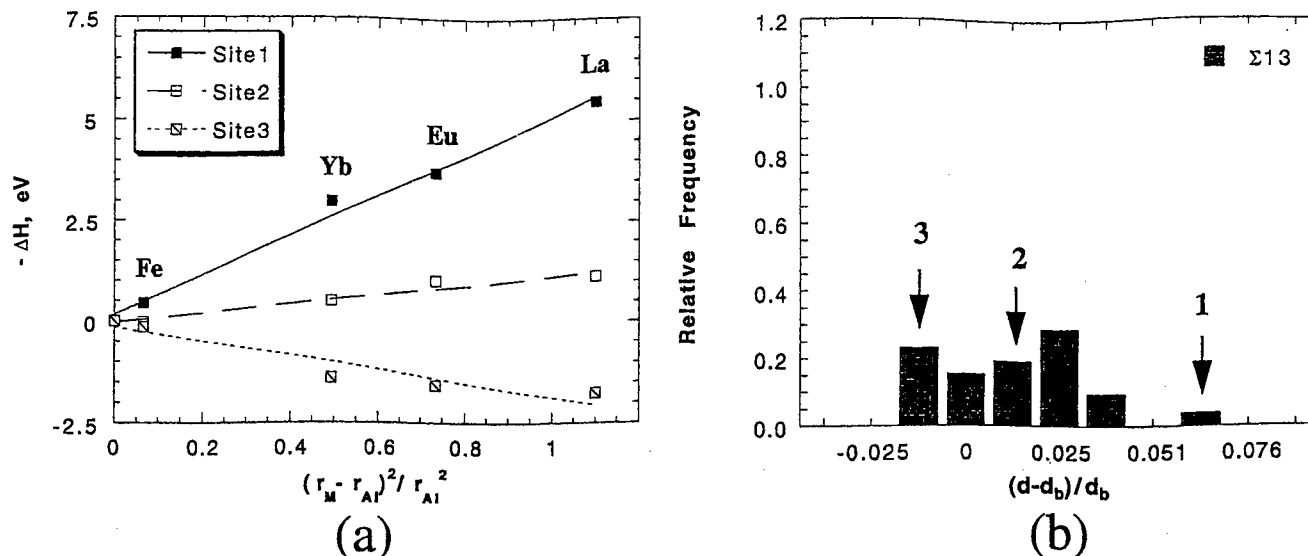
Fig. 9. (a) Segregation enthalpy, ΔH, versus square of the difference in radii for four different dopant ions at three different sites in the same boundary plane of $\Sigma13$. (b) Three different sites representing largest ($d/d_b = 1.067$), intermediate (1.018), and smallest (0.9813), as shown in this histogram.

likely governs this response. From this perspective, one can envision scenarios in which a relatively small impurity concentration at the boundary can substantially improve creep resistance by blocking or modifying a few, critical diffusive pathways. Such synergies in yttrium- and lanthanum-doped Al_2O_3 are described in the Introduction.

Finally, the results of this study of Al_2O_3 grain boundaries correlate roughly with some experimental findings, namely that the largest substitutional sites represent ~4% of the $\Sigma13$ boundary sites, translating to the 5%–10% of dopant coverage found in both SIMS and STEM work.[4,5] It should be noted, however, that our simulations are clearly idealized in certain respects. For example, the present work was performed at 0 K, where vacancy formation is not a factor; whereas, at higher temperatures, the presence of vacancies can alter detailed boundary structure[34] and presumably, therefore, detailed segregation profiles. Also, while general grain boundaries are clearly present in the experimental systems studied to date, we have confined our investigations to a subset of special boundaries given the constraints of spatial periodicity and system size. Thus, we have focused here only on two prototypical special boundaries on the basal plane. A more extensive study of other special boundaries, with a possible extrapolation to general boundaries, is contemplated for future work.

IV. Summary

In this study, the volumes associated with several special grain boundaries in Al_2O_3 were characterized by a spatially local Voronoi construction in order to identify potential sites for impurity segregation. In particular, both the $\Sigma3$ (twin) and the $\Sigma13$ basal boundaries were examined in some detail in order to determine the frequency and spatial distribution of these sites. In conjunction with this geometrical study, a complementary energetic analysis yielded site segregation enthalpies and shed some light on observed experimental behavior. The dependence of enthalpy on ionic radius was examined by simulating ionic size mismatch using a variety of isovalent dopants, and it was found that the strain energy associated with this mismatch contributed significantly to the driving force for segregation.

As indicated above, a better understanding of boundary segregation behavior in polycrystalline Al_2O_3 systems is key to describing the enhancement of time-dependent mechanical properties given that segregation is likely to alter boundary transport. Thus, future efforts are directed at linking segregation to transport properties at grain boundaries and at investigating boundary segregation in codoped Al_2O_3 by using computer simulation. In

this way, one may be able to identify which dopants and which boundaries have the greatest impact on observed creep behavior.

References

[1]J. Cho, M. P. Harmer, H. M. Chan, J. M. Rickman, and A. M. Thompson, "Effect of Yttrium and Lanthanum on the Tensile Creep Behavior of Aluminum Oxide," *J. Am. Ceram. Soc.*, **80** [4] 1013–17 (1997).

[2]J. D. French, J. Zhao, M. P. Harmer, H. M. Chan, and G. A. Miller, "Creep of Duplex Microstructures," *J. Am. Ceram. Soc.*, **77** [11] 2857–65 (1994).

[3]C.-W. Li and W. D. Kingery, "Solute Segregation at Grain Boundaries in Polycrystalline Al_2O_3"; pp. 368–78 in Advances in Ceramics, Vol. 10, *Structure and Properties of MgO and Al_2O_3 Ceramics*. Edited by W. D. Kingery. American Ceramic Society, Columbus, OH, 1984.

[4]A. M. Thompson, K. K. Soni, H. M. Chan, M. P. Harmer, D. B. Williams, J. M. Chabala, and R. Levi-Setti, "Rare Earth Dopant Distributions in Creep-Resistant Al_2O_3," *J. Am. Ceram. Soc.*, **80** [2] 373–76 (1997).

[5]J. Bruley, J. Cho, H. M. Chan, M. P. Harmer, and J. M. Rickman, "Scanning Transmission Electron Microscopy Analysis of Grain Boundaries of Creep-Resistant Yttrium- and Lanthanum-Doped Alumina Microstructures," *J. Am. Ceram. Soc.*, **82** [10] 2865–70 (1999).

[6]R. M. Cannon and R. L. Coble, "Review of Diffusional Creep of Al_2O_3"; pp. 61–100 in *Deformation of Ceramic Materials*, Proceedings of a Symposium on Plastic Deformation of Ceramic Materials (Pennsylvania State University, July 1974). Edited by R. C. Bradt and R. E. Tressler, Plenum, New York, 1975.

[7]A. H. Chokshi and T. G. Langdon, "Diffusion Creep in Ceramics: A Comparison with Metals"; pp. 1205–26 in *Diffusion in Metals and Alloys DIMETA 88*, Defect and Diffusion Forum, Vols. 66–69 (Balatonfüred, Hungary, September 1988). Edited by F. J. Kedves and D. L. Bake. Sci-Tech Publications, Brookfield, VT, 1990.

[8]Y.-Z. Li, C. Wang, H. M. Chan, J. M. Rickman, and M. P. Harmer, "Codoping of Alumina to Enhance Creep Resistance," *J. Am. Ceram. Soc.*, **82** [6] 1497–504 (1999).

[9]C. R. W. Catlow, R. James, W. C. Mackrodt, and R. F. Stewart, "Defect Energetics in α-Al_2O_3 and Rutile TiO_2," *Phys. Rev. B: Condens. Matter*, **25** [2] 1006–26 (1982).

[10]N. W. Ashcroft and N. D. Mermin, *Solid State Physics*. Holt, Rinehart, and Winston, New York, 1976.

[11]P. P. Ewald, "Die Berechnung Optischer und Elektrostatischer Gitterpotentiale," *Ann. Phys. (Leipzig)*, **64**, 253–87 (1921).

[12]M. P. Allen and D. J. Tildesley, *Computer Simulation of Liquids*; pp. 156–62. Oxford Press, Oxford, U.K., 1987.

[13]K. L. Kliewer and J. S. Koehler, "Space Charge in Ionic Crystals. I. General Approach with Application to NaCl," *Phys. Rev. A*, **140** [4A] 1226–39 (1965).

[14]D. M. Duffy and P. W. Tasker, "Space-Charge Regions around Dipolar Grain Boundaries," *J. Appl. Phys.*, **56** [4] 971–77 (1984).

[15]B. G. Dick and A. W. Overhauser, "Theory of the Dielectric Constants of Alkali Halide Crystals," *Phys. Rev.*, **112**, 90–103 (1958).

[16]W. H. Press, S. A. Teukolsky, W. T. Vetterling, and B. P. Flannery, *Numerical Recipes in Fortran: The Art of Scientific Computing*, 2nd ed.; pp. 413–18. Cambridge, New York, 1992.

[17]J. D. Rittner, D. Udler, and D. N. Seidman, "Solute–Atom Segregation at Symmetric Twist and Tilt Boundaries in Binary Metallic Alloys on an Atom-Scale," *Interface Sci.*, **4**, 65–80 (1996).

[18]A. P. Sutton and R. W. Balluffi, *Interfaces in Crystalline Materials*; pp. 3–68. Clarendon, Oxford, U.K., 1995.

[19]H. Grimmer, R. Bonnet, S. Lartigue, and L. Priester, "Theoretical and Experimental Descriptions of Grain Boundaries in Rhombohedral α-Al$_2$O$_3$," *Philos. Mag. A*, **61** [3] 493–509 (1990).

[20]J. Cho, "Role of Rare-Earth Dopants on the Improved Creep Properties of Aluminum Oxide"; Ph.D. Thesis, Lehigh University, Bethlehem, PA, 1998.

[21]D. Wolf, "Energy and Structure of (001) Coincidence-Site Twist Boundaries and the Free (001) Surface in MgO: Theoretical Study," *J. Am. Ceram. Soc.*, **67** [1] 1–13 (1984).

[22]M. F. Ashby, F. Spaepen, and S. Williams, "The Structure of Grain Boundaries Described as a Packing of Polyhedra," *Acta Metall.*, **26**, 1647–63 (1978).

[23]H. J. Frost, "A First Report on a Systematic Study of Tilt-Boundaries in Hard Sphere F.C.C. Crystals," *Scr. Metall.*, **14**, 1051–56 (1980).

[24]J. L. Finney, "Random Packings and the Structure of Simple Liquids I. The Geometry of Random Close Packing," *Proc. R. Soc. London A*, **319**, 479–93 (1970).

[25]D. Srolovitz, K. Maeda, S. Takeuchi, T. Egami, and V. Vitek, "Local Structure and Topology of a Model Amorphous Metal," *J. Phys. F: Met. Phys.*, **11**, 2209–19 (1981).

[26]M. M. El-Aiat and F. A. Kröger, "Yttrium, an Isoelectric Donor in α-Al$_2$O$_3$," *J. Am. Ceram. Soc.*, **65** [6] 280–83 (1982).

[27]M. K. Loudjani, A. M. Huntz, and R. Cortès, "Influence of Yttrium on Microstructure and Point Defects in α-Al$_2$O$_3$ in Relation to Oxidation," *J. Mater. Sci.*, **28**, 6466–73 (1993).

[28]J. D. Eshelby, "The Continuum Theory of Lattice Defects," *Solid State Phys.*, 3, 79 (1956).

[29]T. S. Bush, J. D. Gale, C. R. A. Catlow, and P. D. Battle, "Self-Consistent Interatomic Potentials for the Simulation of Binary and Ternary Oxides," *J. Mater. Chem.*, **4** [6] 831–37 (1994).

[30]D. McLean, *Grain Boundaries in Metals*, Clarendon, Oxford, U.K., 1957.

[31]P. W. Tasker, "Surfaces of Magnesia and Alumina"; see Ref. 3, pp. 176–89.

[32]M. A. Gülgün, V. Putlayev, and M. Rühle, "Effects of Yttrium Doping in α-Alumina: I. Microstructure and Microchemistry," *J. Am. Ceram. Soc.*, **82** [7] 1849–56 (1999).

[33]J. Cho, C. M. Wang, H. M. Chan, and J. M. Rickman, "Role of Segregating Ions on the Improved Creep Resistance of Aluminum Oxide," *Acta Mater.*, in press.

[34]M. P. Harmer, H. M. Chan, J. M. Rickman, J. Cho, and C. M. Wang, "Grain Boundary Chemistry and Creep Resistance of Oxide Ceramics"; pp. 139–44 in *The Science of Engineering Ceramics II*. Edited by K. Niihara, T. Sekino, E. Yasuda, and T. Sasa. Trans Tech Publication Ltd., Aedermannsdorf, Switzerland, 1998. □

3.5 Scanning Transmission Electron Microscopy Analysis of Grain Boundaries in Creep-Resistant Yttrium- and Lanthanum-Doped Alumina Microstructure

By

J. Bruley, J. Cho, H. M. Chan, M. P. Harmer,
and J. M. Rickman

journal

Scanning Transmission Electron Microscopy Analysis of Grain Boundaries in Creep-Resistant Yttrium- and Lanthanum-Doped Alumina Microstructures

John Bruley,[†] Junghyun Cho,[*] Helen M. Chan,[*] Martin P. Harmer,[*] and Jeffrey M. Rickman[*]

Materials Research Center and Department of Materials Science and Engineering, Lehigh University,
Bethlehem, Pennsylvania 18015

High-spatial-resolution analytical electron microscopy using energy-dispersive X-ray (EDX) and electron energy-loss spectrometry (EELS) of yttrium- and lanthanum-doped Al_2O_3 has been conducted to ascertain the level of segregation of these impurities to grain boundaries. Line profile analyses indicate that the segregation is confined to a layer thickness of <3 nm. Similar amounts of excess solute have been observed in both dopant systems: 4.4 ± 1.5 and 4.5 ± 0.9 at./nm^2 for yttrium and lanthanum, respectively. Assuming all the segregant is uniformly distributed within ±0.5 nm of the boundary, this excess corresponds to 9 ± 3 at.% for yttrium-doped Al_2O_3 and 10 ± 2 at.% for lanthanum-doped Al_2O_3. For both dopant systems, examination of the spatially resolved electron energy-loss near-edge structures (ELNES) on the Al-$L_{2,3}$ edge suggests a loss in octahedral symmetry and a slight Al–O bond-length expansion. No significant change is noted in the O-K edge.

I. Introduction

THE controlled doping of ultra-high-purity Al_2O_3 with small amounts (<1000 ppm) of rare-earth elements, such as lanthanum and yttrium, dramatically alters sintering and creep rates in these systems.[1–4] Furthermore, the introduction of similar dopants in many metal alloys reportedly influences their high-temperature oxidation properties.[5] Given these observations, considerable effort has been directed at elucidating the function of dopants in rate-dependent processes in ceramic oxides. Because the dopants under consideration have relatively low solubilities in Al_2O_3, most studies have noted that dopant grain-boundary segregation is generally favorable and have, therefore, focused on the structural and chemical changes at boundaries that attend segregation. In particular, several investigations have identified (a) the misfit strain energy of solute ions and (b) the presence of space-charge layers comprising charged point defects near boundaries as two important factors that correlate with the propensity for segregation as well as boundary transport rates.[6–11]

A consistent picture of boundary segregation is beginning to emerge from studies in Al_2O_3. For example, from measurements of segregation profiles using energy-dispersive X-ray (EDX) with scanning transmission electron microscopy (STEM), Li and Kingery[12] have concluded that the primary driving force for the segregation of isovalent cations is the

strain energy associated with ionic misfit. Recent calculations are consistent with this conclusion.[4,13,14] The impact of a segregant on boundary structure also has been of some interest. Indeed, prompted by recent speculation that yttrium doping enhances the population of special "near coincidence" boundaries in hot-pressed Al_2O_3[1,15] Cho et al.[16] have shown that the grain-boundary structure in Al_2O_3 (as characterized by the frequency of selected coincident lattice site boundaries (CSLs) and the grain-boundary misorientation distribution) is not significantly altered by the addition of yttrium. This observation is also consistent with the TEM work of Gülgün et al.,[17] who studied the same yttrium-doped material as examined in the present work. These researchers have characterized more than 100 grain boundaries in yttrium-doped Al_2O_3, and they have found very few special boundaries. Thus, the beneficial influence of yttrium-doping appears not to be primarily through its effect on the grain-boundary structure. Moreover, yttrium has been found to segregate to all grain boundaries, having a maximum coverage on dense (01$\bar{1}$2) planes. Although a somewhat decreased level of yttrium on the basal (0001) planes is observed (although a significant amount of silicon is present), even apparently "clean" boundaries have shown significant segregation to grain-boundary dislocation cores.

Striking visual evidence of grain-boundary segregation has been provided by other probes. Most notably, Thompson et al.[3] have used scanning ion mass spectrometry (SIMS) mapping to vividly demonstrate the widespread uniformity of grain-boundary segregation of lanthanum and yttrium in doped Al_2O_3. The images indicate qualitatively that segregation is essentially isotropic, with very few boundaries denuded of segregant ions. Although this technique provides elemental maps with parts-per-million sensitivity, it is, unfortunately, not yet sufficiently reliable for quantification. Furthermore, the lateral spatial resolution of SIMS, which is of the order of 0.1 μm, is inadequate for modeling of grain-boundary segregation structures.

The goal of the present work is to use EDX and electron energy loss spectroscopy (EELS) in a dedicated STEM to analyze quantitatively the grain-boundary segregation profiles in the same doped, high-purity aluminas examined earlier.[2–4] Another goal is to investigate the coordination environment of the aluminum and oxygen ions in the vicinity of the boundary, using spectrum-line profiling. This is accomplished by examining the characteristic near-edge structures of the elemental ionization edges. Taken together, this information provides valuable new understanding on grain-boundary structure and chemistry near segregated interfaces in Al_2O_3.

II. Experimental Procedure

The two samples selected for this analysis were processed using procedures described in earlier studies.[2–4] In brief, the first specimen was composed of high-purity commercial Al_2O_3 powder (AKP-53, Sumitomo Chemicals, Tokyo, Japan) doped with 1000 at. ppm yttrium and hot pressed at 1475°C under

vacuum to >99% of theoretical density. An inspection of the sample microstructure indicated the presence of yttrium aluminum garnet (YAG) precipitates and an average Al_2O_3 grain size of 2 ± 1 μm. The second sample was doped with 500 ppm lanthanum, hot-pressed at 1450°C; it also contained second-phase particles. Some isolated elongated grains were observed, and the average grain size of the lanthanum-doped sample was 1.7 ± 0.8 μm. The presence of a second phase in these two systems indicated that the solubility limit of the bulk and grain-boundary regions had been exceeded. The samples were prepared for analytical electron microscopy (AEM) by conventional polishing and dimpling, followed by ion milling.

Analytical microscopy was conducted in dedicated STEMs (Models HB603 and the HB501, VG Microscopes, East Grinstead, U.K.) operated at 300 and 100 keV, respectively. The 300 keV microscope was fitted with a windowless Si(Li) detector (Link Systems, Boston, MA) that enabled the highest spatial resolution and best detection sensitivity for EDX analysis. The 100 keV instrument, fitted with a parallel EELS detector (Gatan, Inc., Pleasanton, CA), was used predominantly for the EELS analysis. In both cases, the machines were operated to provide a beam current of ~0.5 nA with a probe diameter of ~1.0 nm, although these values were not explicitly determined for this study. For a typical foil thickness of ~50 nm, the electron beam broadening for 300 keV electrons was expected to be ~2 nm.[18] Only those boundaries that appeared planar and edge-on to the beam were examined to accomplish the analysis. Two analytical procedures were followed. The first involved acquiring spectral data while simultaneously scanning the probe over a small square area of sample (typically 64 nm^2). The second approach involved data acquisition at discrete points across a line perpendicular to the boundary using digital beam control. EELS "spectrum-lines" were acquired using a custom function[‡] operating within commercial software.

III. Results

(1) Compositional Information

(A) *Yttrium-Doped Al_2O_3:* To ascertain the level of yttrium segregation to grain boundaries in Al_2O_3, we begin by examining a boundary image and its associated EDX spectrum. Figure 1 shows a typical EDX spectrum recorded with the beam located over a grain boundary. Superimposed is the corresponding spectrum from an adjacent region within the grain, recorded under identical conditions. The marked difference in the intensity of the yttrium peaks is evident, indicating that the boundary region is yttrium-rich. Examination of the boundaries using conventional TEM imaging has revealed no evidence of a continuous grain-boundary phase. Figure 2 shows a high-angle annular dark-field (ADF) (or Z-contrast) image of a particular grain boundary; the bright contrast at the boundary confirms the segregation of the (higher atomic number) yttrium ions to the boundary plane. (The ADF inner angle was ~30 mrad.) A bright, second-phase, particle pinning the grain boundary also is present. Comparable data have been recorded at seven other grain boundaries, each indicating similar segregation behavior. No distinction is made here between special and general boundaries.

Quantification of the EDX spectra was accomplished by application of the Cliff–Lorimer equation.[19] The yttrium-to-aluminum atomic sensitivity k-factor for the lines was determined using $Y_3Al_5O_{12}$ powder (Alfa Aesar, Ward Hill, MA) as a standard and found to be k_{YA1} = 0.53. The mass absorption correction factor was estimated to be >0.97 for a 50 nm thick foil and, therefore, neglected. A summary of the analyses is given in Table I. The following simple geometric model was
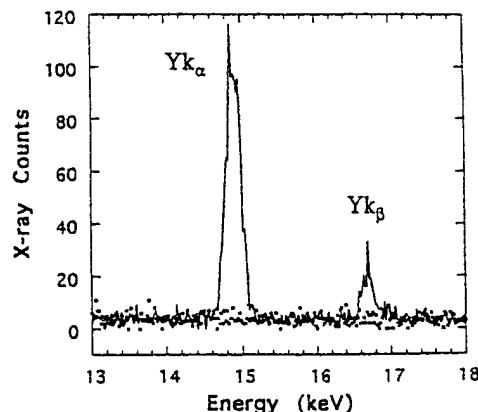
Fig. 1. EDX spectrum taken from grain-boundary region in yttrium-doped Al_2O_3 ((•) data taken from the grain interior).

used to convert the measured intensity ratio, I_i/I_{Al}, to a segregated grain-boundary excess amount. The interaction volume was assumed to be the thickness multiplied by the irradiated area, d^2, where d was the larger dimension of the beam raster or probe size. The area of grain boundary illuminated was the product of d and the foil thickness. The grain-boundary excess (per unit area), Γ_i, of element i is then given by

$$\Gamma_i = d\rho_{Al}k\frac{I_i}{I_{Al}}$$

where ρ_{Al} is the atomic density of aluminum in α-Al_2O_3. The data in the fourth column of Table I represent the amount of yttrium, assuming that it was homogeneously distributed within a 1 nm thick boundary layer. The average yttrium content of the boundary was 4.4 ± 1.5 at./nm^2, which was equivalent to a cation fraction of 9 ± 3 at.%. No other significant level of impurity segregant was detected (sensitivity limit of ~0.5 at.% in 1 nm). Moreover, high-resolution electron microscope (HREM) imaging of the grain boundary (see, for example, Fig. 3), did not reveal a continuous glassy phase.

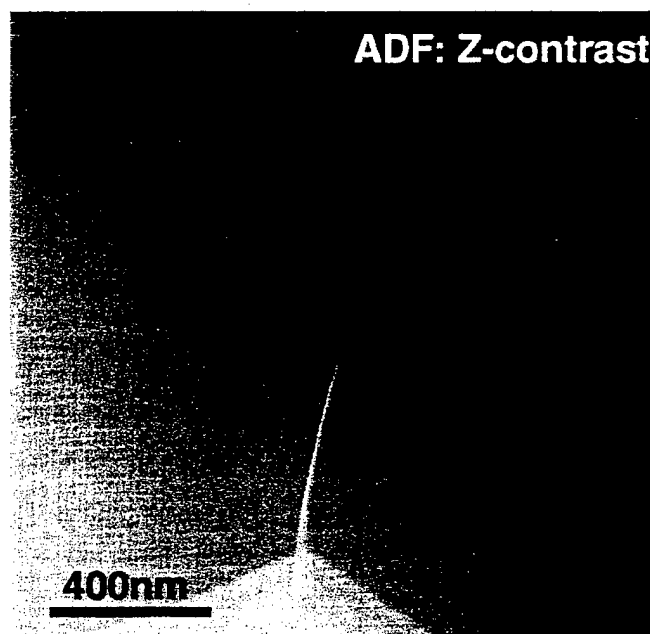Further insight into the segregation behavior at grain bound-

Fig. 2. ADF image of grain-boundary region in yttrium-doped sample. Enhanced brightness corresponds to increased mass thickness associated with yttrium segregation.

Table I. Grain-Boundary EDX Analysis of Yttrium-Doped Al_2O_3

N_Y/N_{Al}	d (nm)	Γ_Y (at./nm²)[†]	ρ_Y/ρ_{Al} in 1 nm[‡]
0.0046	12	2.6	0.06
0.0020	43	4.1	0.08
0.0035	43	7.1	0.13
0.0027	43	5.5	0.12
0.0117	4	2.2	0.05
0.0556	2	5.2	0.11
0.0509	2	4.8	0.10
0.0420	2	4.0	0.08
		⟨4.4 ± 1.5⟩	⟨0.09 ± 0.03⟩

[†]Γ_{Al} on (0006) in α-Al_2O_3 = 10 at./nm². [‡]ρ_{Al} = 47.1 at./nm³.
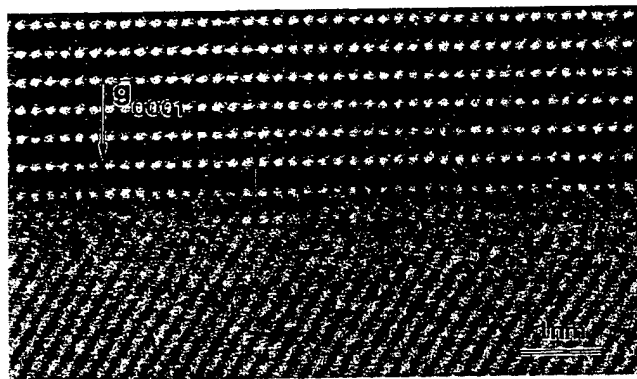

Fig. 3. HREM image of a grain boundary parallel to (0001) plane (note absence of a glassy grain-boundary phase). (Courtesy of M. A. Gülgün and M. Rühle.)
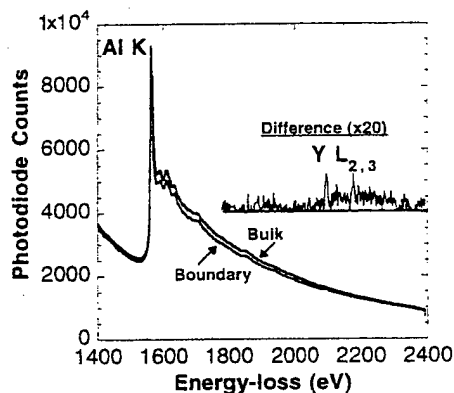

Fig. 4. EELS spectrum of grain boundary in yttrium-doped Al_2O_3. Spatial difference approach used to expose the $L_{2,3}$ edge onset at 2080 eV.

aries has been obtained using EELS. Figure 4 shows an EELS spectrum revealing the onset of the weak Y-$L_{2,3}$ edge at 2080 eV superimposed on an intense background. The Al-K edge onset is located at 1560 eV. Because of the very low signal to background ratio (<0.05), evidence of the yttrium edge is poor. As a consequence, conventional background subtraction procedures, such as power-law fitting, are not feasible. An alternative method involves using the "spatial difference" approach, where the background is simply modeled using a standard spectrum taken under identical conditions from the neighboring Al_2O_3 matrix. The spatial difference is then the residual given by the difference between the boundary and standard spectra. The as-recorded spectrum-line data set can be envisaged in three dimensions with beam position and energy loss plotted on
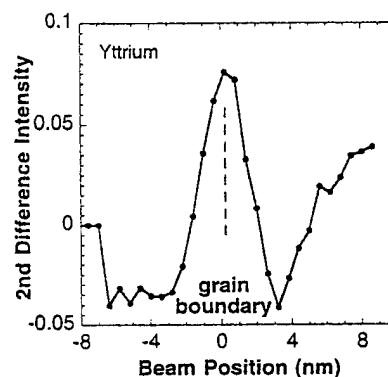

Fig. 5. Profile resulting from application of top-hat filter to spectrum-line data. Individual spectra in the spectrum-line series were normalized to the same intensity within a 50 eV pre-edge window so as to eliminate the effects of grain-boundary grooving on the intensity profile.

the x- and y-axes, respectively, and intensity plotted on the z-axis (see, for example, Fig. 7).

A relatively novel procedure was devised to extract the yttrium segregation profile from the above data, whereby a one-dimensional top-hat filter[20] was passed along the beam position coordinate, and the net counts within a 100 eV energy window centered on 2130 eV was determined. The spectra in the line series were first normalized in a 100 eV wide energy window centered at 2030 eV to minimize the effects of grain-boundary grooving. The optimum choice of the lobe dimensions of the top-hat filter depended on the pixel sample density, the instrumental probe, the counting statistics in the data, and the actual distribution of the segregant. In the limit of high sampling, good statistics, and narrow lobes on the filter, a profile was equivalent to a second derivative of the concentration distribution along the line-profile. Figure 5 represents such a profile generated from the yttrium-edge spectrum-line for a filter that had lobes 3 nm in width. In this case, the resultant width of the profile was probably determined by the spatial resolution of the microscope. The profile clearly illustrated the effectiveness of the filtering technique in revealing the change in yttrium content at the Al_2O_3 boundary.

(B) Lanthanum-Doped Al_2O_3: As in the case of yttrium, lanthanum was segregated at all the boundaries examined. A line profile extracted from a series of EDX spectra taken across one such boundary showed that the lanthanum was localized to a region of full-width half-height equal to 3 nm (see Fig. 6). This width was almost certainly limited by experimental conditions: the probe size was ~1 nm, and beam broadening due to multiple electron scattering was ~2 nm for a 50 nm thick Al_2O_3
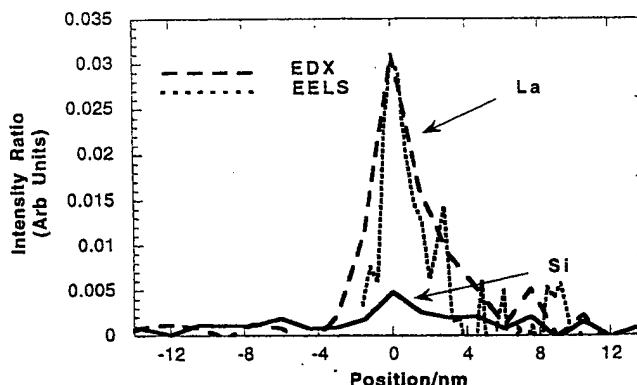

Fig. 6. Comparison of EDX and EELS profiles across boundary of lanthanum-doped Al_2O_3. The full width of the segregant layer is <2 nm.

foil. For the purposes of quantitative analysis, the thin-film lanthanum to aluminum atomic k-factor was determined using a $LaAlO_3$ powder (Alfa Aesar) as a standard. The resulting value was $k_{LaAl} = 0.51$; effects due to absorption and/or fluorescence were ignored. The lanthanum analysis results (for eight separate boundaries) are summarized in Table II. The average lanthanum excess at the boundary was 4.5 ± 0.9 at./nm^2, which is equivalent to 10 ± 2 at.% of the cation population uniformly distributed within a 1 nm thick layer.

In addition to the presence of lanthanum, a small concentration of silicon was segregated to the boundary, as shown in Fig. 6. The amount was estimated to be ~2 at.% within ±0.5 nm of the boundary and was too small to be associated with a continuous siliceous intergranular layer. The line-profile showing lanthanum segregation determined using EELS was slightly narrower than that determined from EDX, i.e., a full-width half-height of 1.5 nm, as compared with 3 nm.

(2) Near-Edge Structure Analysis

In addition to compositional information, EELS is able to provide the density of unoccupied electronic states lying above the Fermi energy, through the fine structures on the ionization edges. The form of the Al-$L_{2,3}$ and the O-K energy-loss near-edge structures (ELNES) can yield insight on the local bonding and coordination of the aluminum and oxygen ions.[21–27] Figure 7 displays a spectrum-line series, consisting of 30 spectra of the Al-$L_{2,3}$ edge recorded along a line perpendicular to the grain boundary. Figure 8 shows the O-K edge series recorded across the same 30 nm long line. In both cases, the data have been processed to remove the smooth power-law background. The boundary plane is readily located at the region corresponding to the reduction in intensity of the aluminum and oxygen edges, most likely due to slight grain-boundary grooving. Preliminary inspection of the oxygen series reveals no grain-boundary-dependent component of the near-edge structure. On the other hand, there is evidence that the shape of the Al-$L_{2,3}$ edge is slightly modified by the presence of the boundary. Specifically, in the boundary region, the initial peak intensity at 79 eV (corresponding to the transition from the $2p$ core state to the $3s$ conduction band), appears somewhat attenuated relative to the remaining ELNES absorption features located at 5 eV above threshold at 83 eV. This modification of the loss spectra is also observed at other boundaries in the lanthanum-doped sample and is similar to preliminary ELNES observations taken from boundaries in the yttrium-doped Al_2O_3. The statistical significance of these qualitative observations has been confirmed using principal components analysis (PCA), which is a matrix transformation tool that results in a list, in order of significance, of series of principal components (eigenvectors) of the original data set.[28] The application of this method has been described previously,[29–31] and, hence, the details are not reproduced here. Finally, to aid in the interpretation of the observed spectral changes in the Al-$L_{2,3}$ ELNES at grain boundaries, the data is compared to the ELNES of two lanthanum aluminate compounds, $LaAlO_3$ and $LaAl_{11}O_{18}$. The Al-$L_{2,3}$ edges of these materials are shown in Fig. 9.
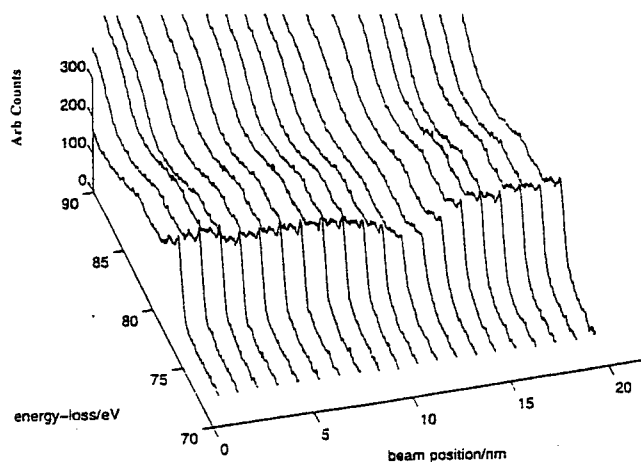

Fig. 7. Spectrum-line of Al-$L_{2,3}$ edge in lanthanum-doped Al_2O_3 after power-law background subtraction. Subtle changes to the edge are discernible in the grain-boundary region.
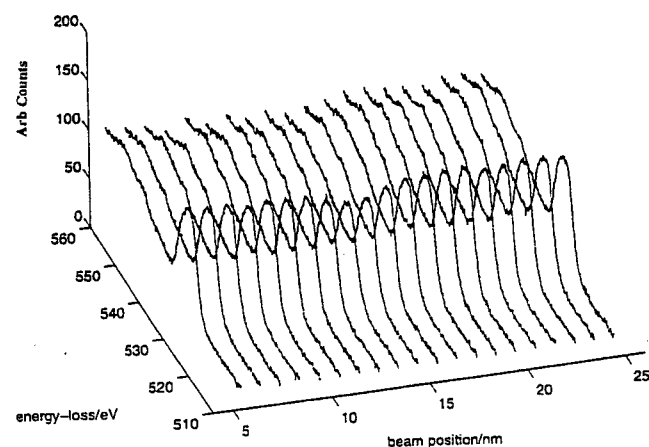

Fig. 8. Spectrum-line of O-K edge in lanthanum-doped Al_2O_3 across same line as in Fig. 7. No changes are observed at the boundary.

IV. Discussion

A comparison of average composition data measured here with those reported by SIMS[3] indicated agreement for the yttrium-doped sample, but a factor of 5 discrepancy for the lanthanum-doped sample (the present study yielding the higher values). This difference was greater than could be accounted for by experimental error alone and, may, in part, have been due to the difference in grain-boundary sampling. For the SIMS technique, data were acquired over micrometer-sized regions containing several grains, whereas, for the AEM measurements undertaken in the present work, only a limited subset of boundaries were present as flat and edge-on to the electron probe. A further possible contribution to the discrepancy could have been inaccuracy of the SIMS calibration. According to Thompson et al.,[3] the amount of segregant was determined by measuring the boundary signal relative to the total signal, collected over a large sample area. This ratio then was multiplied by the nominal concentration of dopant to give the grain-boundary content. If, for any reason, there was a nonuniform distribution of lanthanum within the sample, and the local dopant concentration within the sampled region was higher than the global content, then the grain-boundary content could have been underestimated by a significant factor.

The aforementioned factor of 5 difference between the SIMS and EDX data for lanthanum segregation has implications for modeling the grain-boundary structure. Table III shows the calculated values of the effective layer width of grain-boundary

Table II. Grain-Boundary EDX Analysis of Lanthanum-Doped Al_2O_3

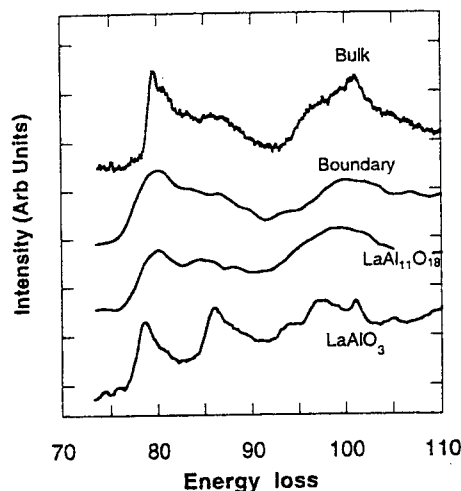| N_{La}/N_{Al}	d (nm)	Γ_{La} (at./nm^2)	ρ_{La}/ρ_{Al} in 1 nm
0.011	8	4.1	0.09
0.010	8	3.8	0.08
0.013	8	4.9	0.10
0.015	8	5.7	0.12
0.015	8	5.7	0.12
0.026	4	4.9	0.10
0.012	5	2.8	0.06
0.047	2	4.4	0.09
		$\langle 4.5 \pm 0.9 \rangle$	$\langle 0.10 \pm 0.02 \rangle$

Fig. 9. Comparison of $Al\text{-}L_{2,3}$ edge spectra from bulk and grain-boundary regions in lanthanum-doped Al_2O_3, bulk $LaAlO_3$, and bulk $LaAl_{11}O_{18}$. (Boundary spectrum was smoothed using a 0.7 eV Gaussian filter.)

second phase ($LaAlO_3$ or $LaAl_{11}O_{18}$) for the various quantification results. A layer thickness of less than the atomic dimension represents the possibility of submonolayer coverage, a situation that leads to difficulties in the computer simulation of boundary segregation. Comparison of these widths with the lattice parameters for the La-Al-O compounds suggests that there is not enough segregant to form a complete unit-cell thickness of any known compound, but there might be enough to form a single plane or two of characteristic structure units.

Another finding of this study, reached by comparing the ELNES structure obtained from the grain-boundary region of the lanthanum-doped samples with that of the two lanthanum aluminates (Fig. 9), is that the $LaAlO_3$ phase is most likely not present. Several observations lead to this conclusion. First, the sharp edge at 86 eV, which is present in the $LaAlO_3$ spectrum, is conspicuously absent in the boundary spectrum. Second, covalent overlap between the Al s and Al d states with the narrow atomic-like La f states leads to the sharp onset of the $Al\text{-}L_{2,3}$ edge in $LaAlO_3$, a feature that is attenuated in the boundary spectrum. However, the edge structure is similar to that of aluminum in the $LaAl_{11}O_{18}$ phase. This finding is consistent with the Al_2O_3–La_2O_3 phase diagram, where the $LaAl_{11}O_{18}$ phase is the most Al_2O_3-rich of the intermediate compounds and would be expected to be the first to form if the solubility limit of La_2O_3 were exceeded. The analytical results are consistent with the formation of up to 1 nm of the aluminum-rich second phase or the equivalent of about one-half of the unit-cell thickness. It is tempting to speculate that grain-boundary saturation of lanthanum corresponds to the formation of a monolayer of characteristic lanthanate structural units.

A simpler picture is that of direct lanthanum substitution for aluminum at the boundary. Such a substitution of the large lanthanum cation (ionic radius of 1.0 Å) might be expected to locally "separate" the (0001) close-packed oxygen basal

planes, thereby decreasing the octahedral symmetry about the smaller neighboring aluminum ions (ionic radius of 0.51 Å). Theory predicts this would lead to mixing of the 3s and 3p final states in the conduction band, which would remove the sharp edge onset characteristic of $Al\text{-}O_6$ structural units. Such a diffuse edge is observed in $\gamma\text{-}Al_2O_3$,[30] inverse spinel,[23] and pure Al_2O_3 grain-boundary structures,[24] and it is a feature characteristic of tetrahedral units. Further evidence of such dilatation is given by the position of the shape resonance at ~100 eV. The energy of this resonance above the Fermi energy has been shown to scale inversely with the square of the average Al–O bond length.[32] Assuming the Fermi energy remains fixed in the middle of the bandgap across the boundary, the resonance for bulk Al_2O_3 is 25.1 eV, whereas that at the boundary is 23.6 eV. According to the inverse quadratic scaling law, this 1.5 eV reduction corresponds to a local 3% Al–O bond-length expansion.

Finally, similar changes in the oxygen data are absent, a result that is somewhat surprising, because some hybridization might have been expected between the O p states with the La f states. An electronic structure model would be needed here to affirm that, with only 10 at.% of segregant, the oxygen density-of-states is unaffected in the boundary region (within the detection sensitivity of the EELS technique).

V. Conclusions

Chemical composition profiles indicate that segregation of yttrium and lanthanum is localized to within ~2 nm of the grain boundary, i.e., about the width of a single unit cell. In both cases, the amount is ~9 at.% within 1 nm of the boundary, which is consistent with the formation of a single layer of aluminum-rich second phase, although none has been confirmed yet. Modification of the $Al\text{-}L_{2,3}$ near-edge structure for the lanthanum-doped sample indicates a significant alteration in the cation bonding with a 3% Al–O bond length expansion. Such changes to the grain-boundary structure and cation-binding energy are consistent with the significant alteration in the diffusional creep properties as reported in the literature.[4,33]

References

[1]S. Lartigue-Korinek and F. Dupau, "Grain Boundary Behavior in Superplastic Mg-Doped Alumina with Yttria Codoping," *Acta Metall. Mater.*, **42** [1] 293–302 (1994).

[2]J. C. Fang, A. M. Thompson, M. P. Harmer, and H. M. Chan, "Effect of Yttrium and Lanthanum on the Final-Stage Sintering Behavior of Ultrahigh-Purity Alumina," *J. Am. Ceram. Soc.*, **80** [8] 2005–12 (1997).

[3]A. M. Thompson, K. K. Soni, H. M. Chan, M. P. Harmer, D. B. Williams, J. M. Chabala, and R. Levi-Setti, "Dopant Distribution in Rare-Earth-Doped Alumina," *J. Am. Ceram. Soc.*, **80** [2] 373–76 (1997).

[4]J. Cho, M. P. Harmer, H. M. Chan, J. M. Rickman, and A. M. Thompson, "Effect of Yttrium and Lanthanum on Tensile Creep Behavior of Aluminum Oxide," *J. Am. Ceram. Soc.*, **80** [4] 1013–17 (1997).

[5]M. L. Gall, A. M. Huntz, B. Lesage, C. Monty, and J. Bernardini, "Self-Diffusion in $\alpha\text{-}Al_2O_3$ and Growth Rate of Alumina Scales Formed by Oxidation: Effect of Y_2O_3 Doping," *J. Mater. Sci.*, **30**, 201–11 (1995).

[6]K. L. Kliewer and J. S. Koehler, "Space Charge in Ionic Crystals. I. General Approach with Application to NaCl," *Phys. Rev. [Sect.] A*, **140** [4] 1226–39 (1965).

[7]M. F. Yan, R. M. Cannon, and H. K. Bowen, "Space Charge, Elastic Field, and Dipole Contributions to Equilibrium Solute Segregation at Interfaces," *J. Appl. Phys.*, **54** [2] 764–78 (1983).

[8]S. K. Tiku and F. A. Kröger, "Effect of Space Charge, Grain-Boundary Segregation, and Mobility Differences between Grain Boundary and Bulk on the Conductivity of Polycrystalline Alumina," *J. Am. Ceram. Soc.*, **63** [3–4] 183–89 (1980).

[9]R. L. Coble, "A Model for Boundary Diffusion Controlled Creep in Polycrystalline Materials," *J. Appl. Phys.*, **34**, 1679–82 (1963).

[10]R. M. Cannon, W. H. Rhodes, and A. H. Heuer, "Plastic Deformation of Fine-Grained Alumina (Al_2O_3): I, Interface-Controlled Diffusional Creep," *J. Am. Ceram. Soc.*, **63** [1–2] 46–53 (1980).

[11]K. R. Venkatachari and R. Raj, "Superplastic Flow in Fine-Grained Alumina," *J. Am. Ceram. Soc.*, **69** [2] 135–38 (1986).

[12]C.-W. Li and W. D. Kingery, "Solute Segregation at Grain Boundaries in Polycrystalline Al_2O_3"; pp. 368–78 in Advances in Ceramics, Vol. 10, *Structure*

Table III.   Thickness of Lanthanum Aluminate Phases for Mean Coverage Measured by SIMS and AEM Techniques

	Thickness (nm)[†]	
	SIMS measurement (2 at.%)	AEM measurement (10 at.%)
$LaAlO_3$ (cubic: a_0 = 3.8 Å)	0.04	0.2
$LaAl_{11}O_{18}$ (hexagonal: a_0 = 5.5 Å, c = 22 Å)	0.2	1.0

[†]Thickness <0.2 nm corresponds to submonolayer coverage.

and Properties of MgO and Al₂O₃ Ceramics. Edited by W. D. Kingery. American Ceramic Society, Columbus, OH, 1984.

[13]M. Exner and M. W. Finnis, "Atomistic Simulation of Grain Boundaries in Alumina," *Mater. Sci. Forum,* **207–209,** 225–28 (1996).

[14]J. Cho, J. M. Rickman. H. M. Chan, and M. P. Harmer, "Modeling of Grain-Boundary Segregation in Aluminum Oxide," *J. Am. Ceram. Soc.,* in press.

[15]D. Bouchet, F. Dupau. and S. Lartigue-Korinek, "Structure and Chemistry of Grain Boundaries in Yttria-Doped Aluminas," *Mater. Sci. Forum,* **207–209,** 205–208 (1996).

[16]J. Cho, H. M. Chan, M. P. Harmer, and J. M. Rickman, "Influence of Yttrium Doping on Grain Misorientation in Aluminum Oxide," *J. Am. Ceram. Soc.,* **81** [11] 3001–3004 (1998).

[17]M. A. Gülgün, V. Putlayev, and M. Rühle, "Effects of Yttrium Doping in α-Alumina: I, Microstructure and Microchemistry," *J. Am. Ceram. Soc.,* **82** [7] 1849–56 (1999).

[18]D. B. Williams, J. R. Michael, J. I. Goldstein, and A. D. Romig Jr., "Definition of the Spatial Resolution of X-ray Microanalysis in Thin Foils," *Ultramicroscopy,* **47,** 121–32 (1992).

[19]J. I. Goldstein, D. B. Williams, and G. Cliff, *Principles of Analytical Electron Microscopy;* p. 155. Edited by D. C. Joy, A. D. Romig, and J. I. Goldstein. Plenum, New York, 1986.

[20]D. B. Williams and C. B. Carter, *Transmission Electron Microscopy;* p. 603. Plenum, New York, 1996.

[21]A. Balzarotti and A. Bianconi, "Electronic Structure of Aluminum Oxide as Determined by X-ray Photoemission," *Phys. Status Solidi B,* **76,** 689–94 (1976).

[22]A. Balzarotti, F. Antonangeli, R. Gilanda, and G. Martino, "Core Excitons in Corundum," *Solid State Commun.,* **44** [2] 275–78 (1982).

[23]J. Bruley, M. W. Tseng, and D. B. Williams, "Spectrum-Line Profile Analysis of a Magnesium Aluminate Spinel/Sapphire Interface," *Microsc., Microanal., Microstruct.,* **6,** 1–18 (1995).

[24]J. Bruley, "Spatially Resolved Electron Energy-Loss Near-Edge Structure

Analysis of a Near Σ = 11 Tilt Boundary in Sapphire," *Microsc. Microanal. Microstruct.,* **4,** 23–39 (1993).

[25]R. Brydson, H. Sauer, W. Engel, and E. Zeitler, "EELS as a Fingerprint of the Chemical Coordination of Light Elements," *Microsc. Microanal. Microstruct.,* **2,** 159–69 (1991).

[26]R. Brydson, H. Sauer, W. Engel, J. M. Thomas, and E. Zeitler, "Coordination Fingerprints in Electron Loss Near-Edge Structures—Determination of the Local Site Symmetry of Aluminum and Beryllium in Ultrafine Minerals," *J. Chem. Soc. Chem. Commun.,* **15,** 1010–12 (1989).

[27]P. L. Hansen, R. Brydson, D. W. McComb, and I. Richardson, "EELS Fingerprint of Al-Coordination in Silicates," *Miscrosc., Microanal., Microstruct.,* **5,** 173–82 (1994).

[28]E. R. Malinowski and D. G. Howery, *Factor Analysis in Chemistry.* Robert E. Krieger Publishing, Malabar, FL, 1989.

[29]S. J. Splinter, J. Bruley, and D. A. Smith. "Decomposition of Electron Energy Loss Spectrum Line Profiles by Target Factor Analysis"; p. 274 in *Proceedings of Microscopy and Microanalysis 95.* Edited by G. W. Bailey, M. H. Ellisman, R. A. Hennigar, and N. J. Zaluzec. Jones and Begell Publishing, New York, 1995.

[30]I. A. Brytov and Y. N. Romaschenko, "X-ray Spectroscopic Investigation of the Electronic Structure of Silicon and Aluminum Oxides," *Sov. Phys. Solid State,* **20** [3] 384–89 (1978).

[31]N. Bonnet, M. Brun, and C. Colliex, "Extracting Information from Sequences of Spatially Resolved EELS Spectra Using Multi-Variate Statistical Analysis," *Ultramicroscopy,* **77** [3] 97–112 (1999).

[32]A. Bianconi, M. Dell'Arriccia, A. Gargano, and C. R. Natoli, *Springer Series in Chemical Physics: EXAFS and Near Edge Structure;* p. 57. Edited by A. Bianconi, L. Incoccia, and S. Stipcich. Springer Verlag, Berlin, Germany, 1983.

[33]Y.-Z. Li, C. Wang, H. M. Chan, J. M. Rickman, M. P. Harmer, J. M. Chabala, K. L. Gavrilov, and R. Levi-Setti, "Codoping of Alumina to Enhance Creep Resistance," *J. Am. Ceram. Soc.,* **82** [6] 1497–504 (1999).　　　□

3.6 Structure of Y and Zr Segregated Grain Boundaries in Alumina

By

C. M. Wang, G. S. Cargill III, H. M. Chan, and M. P. Harmer,

Structure of Y and Zr Segregated Grain Boundaries in Alumina

C. M. Wang, G. S. Cargill III, H. M. Chan, and M. P. Harmer,

Materials Research Center
Lehigh University
Bethlehem, PA 18015

Abstract

Grain boundary segregation of Y and Zr in α-Al_2O_3 and the atomic structural environment around the Y and Zr atoms have been investigated using high resolution STEM and EXAFS. At dilute concentrations, the Y ions in α-Al_2O_3 grain boundaries, on average, are coordinated by 4 oxygens, at a distance of 2.30 Å, which corresponds nearly to the Y-O bond length in cubic Y_2O_3, and Zr ions are coordinated by 5 oxygens at a distance of 2.14 Å, which is approximately the same as the average Zr-O bond length in monoclinic ZrO_2. However, in the EXAFS radial distribution function, the Y-cation and Zr-cation next nearest neighbor shell cannot be clearly identified. These results suggest that Y and Zr at dilute concentrations in α-Al_2O_3 occupy grain boundary sites with well defined nearest neighbor cation-oxygen bond lengths similar to those in their parent oxides, but with the next nearest neighbor cation-cation distances varying considerably from site to site. Grain growth can cause grain boundaries to become supersaturated by Y. In this case, both the Y-O nearest neighbor coordination number and the ordering of Y with respect to Al ions beyond nearest neighbor O are increased. This Y-Al distance is the same as that expected for the Y-Al distance when Y substitutes for Al while relaxing the Y-O distance to that in Y_2O_3. This may indicate that as the Y concentration increases, Y begins to occupy near-boundary sites in planes on each side of the geometrical boundary. In these near-boundary planes, the nearest neighbor ordering extends at least to nearest neighbor cations. Nucleation of the YAG phase leads to the depletion of these partially ordered layers.

Key words: EXAFS, Alumina, Grain Boundary Segregation, Atomic Structure, Y and Zr.

I.   Introduction

Dopant and impurity grain boundary segregation has been found in both metals and ceramics [1-4]. The grain boundary segregants may have either detrimental or beneficial effects on a material's microstructures and properties. An example of the detrimental aspects of grain boundary segregation is segregation-induced intergranular fracture embrittlement [5]. On the other hand, it has long been recognized that doping alumina forming alloys with Y significantly improves their oxidation resistance [6]. More recently, it has been shown that doping trace amounts of rare-earth oxide (typically 100 to 1000 ppm) in high purity alumina induces a 2 to 3 orders of magnitude increase in the creep resistance [7-11] (Fig. 1). A better understanding of the mechanisms by which such impurities influence material properties is key for further exploiting these effects and for optimizing material properties.

Many efforts have been made over the last few years to correlate microstructural features with properties of rare earth doped high purity alumina. Based on transmission electron microscopy (TEM) studies of grain boundaries in doped alumina, Lartigue and co-workers [12] postulated that dopant ions impede the accommodation of intergranular dislocations by decreasing the grain boundary diffusivity, and hence limit grain boundary sliding. Yoshida, Ikuhara, and Sakuma [11] have systematically investigated the role of rare-earth dopants on the creep properties of alumina, and they also postulated that the increased creep resistance is possibly related to decreased grain boundary diffusivity. A recent study by Cho et al. [13] using Orientation Image Mapping (OIM) found no obvious difference in the distribution of grain boundary types between undoped and Y-doped alumina. The results of Cho et al. are consistent with a recent TEM survey of grain boundary type distribution in Y-doped alumina [14], where very few special boundary types were found. By using secondary ion mass spectroscopy (SIMS) mapping, Thompson et al. [3] have shown that Y and La dopants are segregated to all types of alumina grain boundaries. Motivated by those observations, the same group has proposed that the increased creep resistance in doped alumina be attributed to reduced grain boundary diffusivity caused by blocking of grain boundaries by the segregated oversized dopants [9,15]. Further evidence in support of this grain boundary blocking model is as follows: (1) The same improvement in creep resistance was observed for

dopant levels both above and below the solubility limit, confirming that the phenomenon is a solid solution effect [15]. (2) The creep resistance improvement depends on the ionic size of the dopant [15]. However, the structural details of the grain boundaries with the segregated dopant remain to be established, both theoretically and experimentally. This information is needed for further understanding of the mechanisms by which segregation affects grain boundary related phenomena.

A variety of microscopic and spectroscopic methods have been employed to investigate the distribution and structural environment of grain boundary segregated dopant ions. These methods have included auger electron spectroscopy (AES) [16], x-ray photoelectron spectroscopy (XPS) [17], energy dispersive x-ray spectroscopy (EDS) in a scanning electron microscope (SEM) and in a scanning transmission electron microscope (STEM) [18, 19], electron energy-loss spectroscopy (EELS), SIMS [3] and extended x-ray absorption fine structure (EXAFS) [20, 21]. AES, XPS, EDS and SIMS have been used mainly to investigate grain boundary segregation concentrations and segregant distribution profiles. STEM measurements by Bruley et al. [18] revealed Y and La dopant ions were segregated to a narrow region at the alumina grain boundaries. Assuming a segregation layer thickness of ~1 nm, the fraction of cation sites occupied by the impurity ions was determined to be ~9-10%. Attempts also have been made using EELS to investigate the local chemical bonding around the dopant ions in 1000 ppm Y_2O_3 and 500 ppm La_2O_3 doped alumina [18]. The structures of alumina grain boundaries with Ca and Zr segregation have been investigated using high resolution transmission electron microscopy (HRTEM) [22, 23].

EXAFS is a powerful method for determining the atomic structural environment around impurities, particularly very dilute impurities, and it has been used to probe the local atomic structural configurations around impurities in various oxides and non-oxides [24-26], including Y_2O_3 stabilized ZrO_2, and Y_2O_3 and ZrO_2 doped alumina (300 ppm to 1 mol%) [20, 21, 27]. However, in the study of Loudjani et al. [20], the Y_2O_3 concentration of 1 mol% exceeded the solid solution limit of the α-Al_2O_3, so yttrium aluminum garnet ($Y_3Al_5O_{12}$, YAG), which precipitated as a secondary phase, masked the EXAFS signal from the grain boundary segregated Y ions. Their later study with 300 ppm Y_2O_3 doped sample showed Y-O and Y-Al contributions without YAG precipitates

[27]. To obtain information about the structural environment of grain boundary segregated Y ions, measurements on more dilute yttrium doped alumina samples and more detailed data analysis were needed. Based on previous microscopic investigations, we have established for very dilute concentrations of doping, typically 100 ppm, that the Y and Zr ions are mainly segregated to the grain boundaries and that secondary phase precipitation is absent [15, 28]. In this paper, we discuss our recent high resolution STEM and EXAFS investigation of high purity alumina doped with Y_2O_3 at concentrations of 100 and 1000 ppm, and ZrO_2 at a nominal concentration of 100 ppm, giving information about the atomic structural environment of grain boundary segregated Y and Zr ions [29, 30]. Furthermore, because the grain boundary area is inversely proportional to the grain size, for a constant initial dopant concentration, the grain boundary segregated dopant concentration can be increased through increasing the grain size. This makes it possible for the first time to explore the interplay between grain boundary dopant concentration and grain boundary structures [31]. Implications of the present results for the effects of the segregants on grain boundary mediated transport are discussed.

II. Experimental procedures

(1) Materials

The samples were ultra high purity Al_2O_3 doped with either Y_2O_3 or ZrO_2. Y_2O_3 was doped at two levels, 100 ppm and 1000 ppm (Y/Al atomic ratio, hereafter referred to as samples 100Y and 1000Y), and ZrO_2 at 100 ppm nominally (Zr/Al atomic ratio, hereafter referred to as sample 100Zr). The doping process involves dispersing ultra-high purity alumina powder (Sumitomo AKP 53, with an average grain size of 0.3 µm, and purity of 99.995%) in methanol. Y-doping was achieved by adding a yttrium nitrate (99.999%, Aldrich Chemical Co.) methanol solution to the Al_2O_3 slurry. Zr-doping was achieved by ball-milling the Al_2O_3 slurry with ZrO_2 grinding media (4.2 mol% Y_2O_3 stabilized tetragonal zirconia, Tosoh U. S. A. Inc., Bridgewater, NJ) for 20 hours. All powder processing was conducted in a class 100 clean room environment using acid washed containers. All the doped powders were hot-pressed using graphite dies in

vacuum at 45 MPa for 30 min. The hot-pressing temperature for the 100Y powder was 1450 °C, for the 1000Y powder was 1475 °C, and for the 100Zr powder was 1320 °C. The 100Y and 1000Y samples have a relative density higher than 99%, and the 100Zr sample has a relative density of 97%. The 100Zr and 100Y samples show a rather uniform grain size distribution, with the 100Y having an average grain size of ~ 1.5 μm (Fig.2(a)), and the 100Zr having an average grain size of ~ 0.5 μm (Fig.2(b). SEM and TEM reveal no secondary phase precipitates in the 100Y and 100Zr materials. The 1000Y material shows a bimodal grain size distribution, with a coarse grain size of ~5μm, and fine grain size of ~1μm. The 1000Y material also has secondary phase precipitates which are mainly in the fine grain size Al_2O_3 regions (Fig.2(c)). To increase the grain boundary segregated dopant concentration, the 100Y sample is annealed at 1450 for 5 to 50 hours to grow the grains.

(2)   STEM analysis of grain boundary Y concentration

Thin foils for STEM analysis were prepared by standard methods, including diamond wheel slicing, thinning, dimpling, and finally ion beam polishing to perforation. To prevent charging during the analysis, a thin carbon film was evaporated on the surface of the thin foils. Quantitative chemical analysis was performed on a Vacuum Generators HB603 dedicated scanning transmission electron microscope operating at 300 keV with a 30 μm virtual objective aperture. The incident probe size was optimized to less than 1 nm and the beam current was about 0.5 nA. Characteristic Al $K\alpha$ and Y $K\alpha$ x-ray lines were measured using an Oxford Instruments windowless Si(Li) EDX detector. Net intensities of these lines were determined by background subtraction and characteristic line peak-integration programs with an Oxford Instruments eXL multi-channel analyzer. EDX spectra were quantified using the Cliff-Lorimer equation [32]. The Y to Al atomic sensitivity factor, $k_{Y/Al}$, was found to be 1.25 using $Y_3Al_5O_{12}$ powder (Alfa Aesar) as a standard. Corrections due to mass absorption and fluorescence were deemed negligible. In order to convert the measured intensity ratio, I_Y/I_{Al}, to a segregant grain boundary excess amount, a square window method is used [33]. The Y grain boundary excess, Γ_Y, which is defined as the amount of solute present per unit area of grain boundary in excess

of the amount of solute that would be present if there were no grain boundary, can be calculated as

$$\Gamma_Y = wn_{Al}k_{Y/Al}[(\frac{I_Y}{I_{Al}})_{GB} - (\frac{I_Y}{I_{Al}})_{BL}] \qquad (1)$$

where w is the width of the electron beam scan area perpendicular to the boundary in nanometers, n_{Al} is the atomic density of Al in α-Al_2O_3, which is equal to 47.1 Al atoms/nm^3, the subscripts *GB* and *BL* represent the grain boundary and bulk lattice, respectively. The bulk lattice term could be neglected because the Y concentrations in the bulk lattice is below the detect limit.

(3)   X-ray absorption measurements and EXAFS data analysis

X-ray absorption measurements at the K edges of Y and Zr were made on Beamline X23A2 of the National Synchrotron Light Source (NSLS) at Brookhaven National Laboratory under normal operating conditions (2.5 GeV, 100-200 mA) and using a Si (311) double crystal monochromator. For bulk materials, the spectra were measured in the fluorescence mode. The incident beam had a cross section of 3 mm x 12 mm and intersected with the specimen surface at 45 degrees. An Ar-filled ion-chamber was used as the fluorescence detector, positioned so that the detector window center line also intersected the specimen surface at 45 degrees but was perpendicular to the incident beam direction. In order to reduce statistical errors during data acquisition, for each specimen about 70 spectra were recorded and averaged. All the EXAFS experiments were carried out at room temperature.

Samples of cubic Y_2O_3 powder (purity 99.99%, Alfa, Johnson Matthey Company) and of monoclinic ZrO_2 powder (purity 99.5%, Alfa, Johnson Matthey Company) were measured in transmission mode, and the data were used as standards for the analysis of data from the doped materials. Samples were prepared by encapsulating the powder between pieces of self-adhesive Scotch Magic tape. As a standard for analyzing secondary phase precipitates in the 1000Y material, bulk polycrystalline $Y_3Al_5O_{12}$ (YAG), which includes 5 vol% Al_2O_3, was also measured in fluorescence mode, but at a detector grazing angle of about 10 degrees. For all the reference samples, at least five spectra were recorded and averaged.

The details of the procedures for extracting EXAFS functions and for fitting of the Y-O nearest neighbor shell have been described previously [29]. Fitting of the Y-cation next nearest neighbor shell began with a two-shell model structure based on the α-Al_2O_3 structure [30]. The model was constructed by substituting a Y ion for an Al ion in α-Al_2O_3 and letting all of the 6 Al-O (3 x 1.85 Å, 3 x 1.97 Å) bond lengths in α-Al_2O_3 be extended to the ideal average Y-O bond length in Y_2O_3 (6 x 2.284 Å), while keeping the O to next nearest neighbor Al ion distances the same as those in α-Al_2O_3 and also preserving the α-Al_2O_3 structural framework. In this model structure, Y has 6 O ions as the nearest neighbors and 7 Al ions as next nearest neighbors. For this model, the Y-Al distances are found geometrically to be 1 x 2.89 Å; 3 x 3.04 Å; and 3 x 3.61 Å. Based on this two-shell model and single scattering, the radial distribution function around the substitutional Y ion was calculated using FEFF code [34].

III. Results

(1) Y Grain boundary segregation behavior

For a constant initial doping concentration, the grain boundaries segregant excess Γ for unsaturated grain boundaries can be expressed as [30]

$$\Gamma = \frac{2N_{Av}\rho_0}{3W_{Al}}dC_0 \qquad (2)$$

where N_{Av} is the Avogadro constant, W_{Al} is the molecular weight of α-Al_2O_3, ρ_0 is the theoretical density of α-Al_2O_3, d is the grain size, and C_0 is the initial dopant concentration. Equation (2) indicates that the grain boundary concentration of Y in polycrystalline α-Al_2O_3 is proportional to the product of the initial dopant concentration, C_0, and the average grain size, d. Thus, for samples doped initially with different dopant concentration, or for samples with the same initial dopant concentration but with different grain size, the dopant grain boundary segregation behavior can be quantified through the measured grain boundary excess, Γ, as a function of the parameter dC_0.

Fig.3 shows the measured dopant grain boundary concentration as a function of dC_0. Each data point represents the average measured on ~ 25 boundaries and the error bar represents the standard deviation for the data. It was found that with increasing dC_0

that Γ reaches to a peak value of 5.1 $\pm$ 0.2 Y atoms/nm^2, which corresponds to a supersaturation of the grain boundaries with the Y ions. In α-Al$_2$O$_3$ the cation average density is 47.1 Al atoms/ nm^3, which corresponds to an Al ion average planar density of 13 Al atoms/ nm^2. The grain boundary Y supersaturation concentration is ~ ½ equivalent monolayer. Following the supersaturation, Γ drops to a value of ~ 3.2 $\pm$ 0.8 Y atoms/nm^2 and shows no further dependence on dC_0. This constant value of Γ apparently corresponds to the equilibrium concentration of Y in α-Al$_2$O$_3$ grain boundaries when the YAG phase co-exists with the grain boundary segregated Y, which from these data is ~ ¼ equivalent monolayer. Fig. 4 shows EDX maps of Y distributions in the grain boundaries corresponding to the grain boundary which is either supersaturated with the Y ions (Fig.4(a) and (b)) or at equilibrium with YAG phase (Fig. 4(c) and (d)).

(2)   Atomic structural environment around the dopant at a dilute concentration

Fig.5 shows the magnitudes of the Fourier transforms of the $k^3\chi(k)$ EXAFS functions, which describe the radial distribution around the absorbing atom. However, the EXAFS phase shift in the Fourier transformation causes the peaks to be shifted to smaller distances [35]. This is symbolically indicated by including a peak shift α in Fig. 5. Qualitative comparisons of the radial distribution functions for the doped materials and the model compounds indicate that EXAFS in the 100Y and 100Zr samples are similarly dominated by the cation-oxygen nearest neighbor (NN) shell; the cation-cation next nearest neighbor (NNN) shell cannot be clearly identified. The radial distribution function for the 1000Y sample shows the same features as the YAG standard sample. The large difference in the radial distribution functions between the 100Y and 1000Y samples, and the very similar radial distribution functions for 1000Y and YAG samples, indicate that most of the dopant in the 1000Y sample is precipitated in the form of YAG, and this is consistent with the estimate from STEM data that ~ 87% of the total dopant in the 1000Y sample appears as the YAG phase [18]. There are no second phase precipitates in the 100Y and 100Zr samples, so the radial distribution functions for the 100Y and 100Zr reflect the structural environments of dopant sites in alumina grain boundaries, and to a much smaller extent in the bulk lattice.

Quantitative fitting of the first shell of the EXAFS data of the 100Y and 100Zr samples gives the average coordination number and the average NN cation-oxygen bond length around the largely grain boundary segregated Y and Zr, and those results are summarized in Table II. The grain boundary segregated Y is coordinated on average by approximately 4 oxygens at an average distance of 2.30 Å, which is approximately equal to the average Y-O NN bond length, 2.28 Å, in cubic Y_2O_3 (Table I), but is much larger than the Al-O NN bond length, 1.91 Å, in α-Al_2O_3. However, in both Al_2O_3 and Y_2O_3, the cation is coordinated by 6 oxygens (octahedral configuration). For the 1000Y sample, fitting gives an average Y-O NN bond length of 2.36 Å, which is approximately equal to that, 2.35 Å, in YAG (Table II). The grain boundary segregated Zr is coordinated on average by 5 oxygens at an average Zr-O NN distance of 2.14 Å, which is approximately equal to the average Zr-O NN bond length, 2.16 Å, in monoclinic ZrO_2. However, this Zr-O coordination number is smaller than that of the zirconia polymorphs, for which the minimum Zr-O coordination number is 7.

(3)   Fine structural features for grain boundaries supersaturated with Y

Fig.6 includes the radial distribution function of the as-hot-pressed 100Y sample (average grain size of ~ 1.5 μm and the grain boundaries Y concentration is below the saturation concentration) and that of the 1450 °C annealed 100Y sample (an average grain size of ~ 3.8 μm for which the Y grain boundary concentration is at supersaturation). Also shown in Fig.6 is the calculated radial distribution function according to the model structure described in section II.3. For clarity, the experimentally obtained radial distribution function of the sample for which the Y grain boundary concentration is at equilibrium with YAG is omitted from Fig.6, because it is nearly identical to that of pure YAG phase. Fig.6 clearly shows that the atomic structural environment around the grain boundary segregated Y depends on the Y grain boundary concentration.

As the grain boundary Y concentration increases gradually from dilute to saturated and finally to supersaturated, the most significant feature which evolves in the radial distribution function is the Y-cation peaks, which become identifiable and which, qualitatively, follow the features of that calculated according to the model structure. Quantitative fitting of the Y-O shell reveals that accompanying the Y grain boundary

supersaturation the Y-O nearest neighbor distance shows no substantial change, while the Y-O coordination number increases. Quantitative fitting of the Y-cation shell gives an Y-cation distance of 3.31 Å. The fitted Y-cation distance is approximately equal to the average Y-Al distance when Y substitutes for Al in α-Al_2O_3 while relaxing the Y-O distance to that in Y_2O_3 and keeping the O-Al distance the same as that in α-Al_2O_3, as in the model described earlier. Those observations suggest that the Y grain boundary supersaturation leads to an increased fraction of Y occupying substitutional sites in α-Al_2O_3.

IV.   Discussion

(1).   Lattice solid solution, grain boundary segregation, and second phase precipitates

In any substitutional doping system with a tendency for dopant grain boundary segregation, if the dopant concentration is above the solid solution limit a secondary phase based on the dopant may precipitate. In this case, the EXAFS signal is expected to be a superposition of contributions from three different environments: dopant precipitated as a secondary phase, dopant segregated to the grain boundaries or other defects (such as dislocation cores), and dopant as a substitutional solute in the host lattice. Due to the different atomic configurations in these three structures, the EXAFS spectra carry information about the relative proportion of each of these three states of the dopant. Based on this, the solid solution limit of the Y as a dopant in α-Al_2O_3 can be estimated using the EXAFS $\chi(k)$.

Significant differences in the EXAFS data of 100 ppm and 1000 ppm Y_2O_3 doped materials, and the striking similarity between EXAFS data for the 1000 ppm data and the YAG data, indicate that Y has a rather low solid solubility in α-Al_2O_3. This is consistent with the microstructural evidence that there are many YAG precipitates in the 1000 ppm Y_2O_3 doped material. If most of the Y atoms are in secondary phase precipitates, their EXAFS contributions will mask those of Y atoms segregated in grain boundaries or located in bulk substitutional sites. Using EXAFS, Loudjani et al. [20] attempted to determine the local atomic structure around Y in 1 mol% Y_2O_3 doped alumina, but their fitted results were actually dominated by the YAG. Later, Loudjani et al. also studied

300 ppm Y_2O_3 doped alumina, and they obtained some information not dominated by the YAG phase [21]. They found a radial distribution function with a high Y-oxygen peak, consistent with our result for the 100Y sample. They also found a small peak attributed to Al neighbors of yttrium localized on the aluminum sites in the bulk.

The present investigation of more dilute doping, at the level of 100 ppm, and with the materials in the grain size range of less than 2 μm, avoids the uncertainties caused by secondary phase precipitates. For the 100Y and 100Zr doped alumina samples, our TEM observations also show that at least 99% of the grains are dislocation free. However, in principle, EXAFS spectra from the 100Y and 100Zr samples are still superpositions of two contributions, one from the dopant in substitutional sites of the α-Al_2O_3 lattice and another from the dopant segregated to the Al_2O_3 grain boundaries.

Absence of a significant Y-Al peak for the as-hot-pressed 100Y sample, or a Zr-Al peak for the as-hot-pressed 100Zr sample indicates that most of the Y and Zr atoms in these samples are not in bulk substitutional sites, but are grain boundary segregated, so the resulting atomic configurational parameters describe the dopant surroundings in α-Al_2O_3 grain boundaries.

(2) Grain boundary segregation sites and relaxation around the segregant

It has been proposed that the ionic size mismatch between the solute and the matrix lattice is the dominant driving force for solute grain boundary segregation [2, 4]. The Y and Zr ions are larger than the Al ions, and they show strong tendency for segregating to α-Al_2O_3 grain boundaries. Information about the sites in α-Al_2O_3 grain boundaries occupied by segregants has been sought both from experiments and from theoretical calculations [18, 21, 36]. Although the Zr and Y have different ionic sizes, the similarity in their EXAFS radial distribution functions (Fig. 5) strongly suggests that the Y and Zr have similar environments, at least within the range of the nearest and next nearest neighbors (within 3 Å). Both distribution functions show prominent cation-oxygen nearest neighbors but no well defined more distant neighbors. This implies that the Y and Zr are indeed similarly sited and mainly segregated to the alumina grain boundaries. The most plausible sites in the grain boundary of α-Al_2O_3 for the segregants Y and Zr are the substitutional Al ion sites. If Y and Zr substitute for Al ions in the

Al_2O_3 grain boundaries, relaxation of the oxygen ions around the segregants is necessary. The present results indicate that the oxygens surrounding the Y and Zr are completely relaxed to the same bond lengths as in Y_2O_3 and ZrO_2. This corresponds to the nearest-neighbor oxygen atoms around the yttrium moving outward by 19%, and to those around the zirconium moving outward by 13% with respect to the normal Al-O distance.

Calculations of cation-oxygen relaxation have been reported for both bulk and grain boundary sites. Ching et al. [37] have conducted an *ab initio* calculation in which a yttrium replaces an aluminum ion in a supercell of α-Al_2O_3 containing 120 atoms. They found that the nearest-neighbor oxygen atoms around the Y moved outward by 8%. This is less than half the relaxation indicated by the present EXAFS measurements if they are interpreted as Y substituting for Al in the grain boundary of α-Al_2O_3. Cho et al. [36] have also treated the substitution of Al by La and Yb in the basal twin boundary of α-Al_2O_3. Their results confirm that large cation-oxygen relaxation can occur for rare earth dopants in Al_2O_3 grain boundaries

A good way to view the difference between grain boundary substitutional sites and bulk lattice substitutional sites may be that in the undoped grain boundary some cation sites are locally compressed and some are locally dilated, whereas in the bulk lattice all cation sites are identical. In the grain boundary, the misfitting dopants, which have larger ionic sizes than Al, preferentially occupy the larger sites, so only small local distortions are required to obtain the ideal nearest neighbor distances, like those in the parent oxides. Larger, higher energy distortions would be required in the bulk. The grain boundary sites are energetically favored compared with the bulk substitutional sites, which makes solubility of the dopants in the grain boundaries much higher than in the Al_2O_3 bulk.

(3) Coordination numbers

The reduced cation-oxygen coordination numbers for the grain boundary segregated Y (N = 4.2) and Zr (N = 5.0) ions obtained from the EXAFS measurements are believed to be significant. We estimate uncertainties in these coordination numbers to be only ± 0.5, as shown in Table II. In the perfect lattices of α-Al_2O_3 and Y_2O_3, Al and Y each have 6 oxygen nearest neighbors, and in the polymorphs of zirconia, each Zr

has at least 7 oxygen nearest neighbors. In this section, we first discuss generally the reduced cation-oxygen coordination number for grain boundary segregated Y and Zr compared with their parent oxides and with α-Al_2O_3 . We then discuss the difference in the grain boundary cation-oxygen coordination numbers between Y and Zr.

We believe that the smaller cation-oxygen coordination numbers of the grain boundary segregated Y and Zr, compared with those in their parent oxides and in α-Al_2O_3, are related to the intrinsic structure of alumina grain boundaries [38]. Both theoretical modeling and STEM energy-loss near-edge structure (ELNES) studies of a near $\Sigma 11$ grain boundary in α-Al_2O_3 have established that in this boundary some Al ions are coordinated by only 4 O atoms [39-41]. Similar results have also been obtained by ELNES analysis of more general grain boundaries in 0.1 mol% ZrO_2 doped alumina [22]. Apparently, distortions in cation arrangements in α-Al_2O_3 grain boundaries, which optimally join together adjacent misoriented crystalline grains, are accommodated by reduced cation-oxygen coordination. The presently observed overall low oxygen coordination number around the grain boundary segregated Y and Zr seems to be consistent with these theoretical models and ELNES observations of grain boundaries in pure and doped α-Al_2O_3.

In considering the reduced cation-oxygen coordination numbers in α-Al_2O_3 grain boundaries, it may be useful to think of the grain boundary as being formed by bringing together the free surfaces of two misoriented grains. On the clean, free surfaces, Al ions will, on average, have reduced oxygen coordinations of about 4.5, consisting of three oxygen atoms shared with other Al ions within the bulk, and one or two non-bridging oxygen atoms. When the free surfaces are brought together, with rotations or displacements to accommodate the grain-to-grain misorientation, some of the Al atoms adjacent to the boundary will have a cation-oxygen coordination less than six, and some will have more than six. The undercoordinated sites may be the energetically preferred sites for Y or Zr to substitute for Al.

In α-Al_2O_3 and MgO-doped α-Al_2O_3, the thermal grooving induced grain boundary dihedral angles are ~ 110 degrees, which implies that the grain boundary energy is approximately equal to the air-exposed α-Al_2O_3 surface energy [42]. This suggests that the atom coordination in the grain boundary may be similar to that in the

free surface, which may retain its cation-oxygen under coordination. However, for a free surface, it is likely that additional oxygen is added by chemisorption from the air, typically as hydroxyls attachments. We recognize that this discussion is quite speculative. Further experimental studies, combining of HRTEM, STEM and EXAFS, together with modeling and simulation calculations, are needed to develop a detailed structural picture of dopant segregation in grain boundaries.

As we noted earlier Loudjani et al. [21] have used EXAFS to determine the oxygen coordination number around the Y in 300 ppm Y_2O_3 doped alumina. They found the nearest oxygen coordination number around the Y to be only about 2.7 (with a Y-O distance of 2.32 Å). They also noticed an additional shell of oxygen at 2.85 Å with a coordination number of 1.7. Adding those two shells together gives a total Y-O coordination number of 4.4, which is within the range we have obtained, although the second shell Y-O distance is larger than we observed.

The experimentally observed difference in the cation-oxygen coordination numbers for Y and Zr may be due to differences in the ionic sizes and valences between Y and Zr. Since Y is larger than Zr, and both are larger than Al, large local distortions or structural modifications will be required if Y or Zr replaces Al in a grain boundary, the more so for Y than for Zr. To allow relaxation of cation-oxygen nearest neighbor distances to those which are energetically favorable for the larger cations, while retaining a local cation concentration of at least 50% Al, local removal of oxygens, or introduction of oxygen vacancies, may be required. This would lead to a reduced cation-oxygen coordination number for Y and for Zr, with a larger reduction expected for the larger Y atom, as observed experimentally.

The smaller ionic size of Zr compared with Y might lead to greater substitutional solubility of Zr in the Al_2O_3 grains. This would give rise to a higher cation-oxygen coordination number for Zr. However, if there were significant substitutional solubility of Zr in the Al_2O_3 grains, second neighbor Zr-Al contributions would be expected in the Zr EXAFS distribution functions, which are not found in the present experimental results.

The larger ionic valence of Zr, +4, compared with that of Y, +3, may also play a role in Zr having a larger cation-oxygen coordination number than Y. Simply replacing an Al^{+3} ion by a Zr^{+4} ion would require a coordination of oxygen around Zr of more than

6 to maintain local charge neutrality. Similar effects may occur in the grain boundary, leading to Zr^{+4} having a larger cation-oxygen coordination than Y^{+3}.

(4)   Spatial distribution of Y and long range ordering around Y in supersaturated grain boundaries

Comparing with the dilute situation, it is apparent that Y supersaturation in grain boundaries induces longer range ordering around Y ions. This suggests that Y supersaturation in grain boundaries leads to an increased fraction of Y ions to occupy substitutional cation sites in the α-Al_2O_3 lattice. Obviously, with the increase of Y grain boundary concentration, two types of Y ions may be significantly contributing to the observed increased degree of ordering around Y beyond the nearest neighbor O. The first type is the Y ions which exist as a solute in the α-Al_2O_3 bulk lattice. With the increasing grain boundary Y concentration, that fraction of Y ions would also be expected to correspondingly increase, as described by the McLean equation [43]. The second type is the Y ions which are segregated to the grain boundaries but are in excess of the Y grain boundary saturation or equilibrium concentration. The segregation behavior suggests that the second type of contribution is dominantly responsible for the observed long range ordering. The supporting evidence for this is the following:

(1) With the increase of the dC_0, the measured grain boundary Y excess shows a linear dependence on dC_0, and the slope of which is approximately that calculated from equation (2). In deriving equation (2), the solubility of the dopant in the bulk lattice was assumed to be very low and independent of the grain boundary dopant concentration. Therefore, the approximate agreement of the linear slope of the experimentally obtained with that calculated from equation (2) suggests that with the increase of the grain size, the induced enrichment of the Y in the grain boundary will not lead to a significant increase of Y in the bulk lattice (Fig.3). Gruffel et al. have also observed, in Y doped alumina, that the grain boundary Y concentration shows a linear dependence on the average grain size [31].

(2) Based on AES study, Macune et al. [44] and Cawley et al. [45] have reported that the solubility limit of Y in α-Al_2O_3 lattice is < 10 ppm.

(3) Both experiments and theory have established that the grain boundary segregation for fine grain-sized polycrystalline material deviates from Arrhenius behavior [46, 47]. For attractive interaction of the segregant atoms in the grain boundary, the grain boundary will be preferentially saturated and the lattice solubility therefore reduced.

Based on these considerations, with the increase of Y grain boundary concentration from ~ 3 Y atoms/nm^2 to ~ 5 Y atoms/nm^2, the structural evolution around the grain boundary segregated Y ion is suggested to occur as follows: Accommodation of the crystallographic misorientation of two grains will lead to some sites in a grain boundary which are energetically favorable for incorporating an oversized dopant ions. The density of the favorable sites in a grain boundary is expected to be determined mainly by the degree of the misorientation of the two grains which confine the grain boundary. At dilute concentrations, the segregants will preferentially occupy the most favorable grain boundary sites, and filling of those favorable sites corresponds to the saturation of the grain boundary with the dopant. As the number of available Y ions increases, the Y ions enter the near-boundary regions, which contain sites energetically more favorable than those within of the bulk lattice. The Y supersaturated α-Al$_2$O$_3$ grain boundaries may be considered structurally to consist of three layers: a core region which accommodates the crystallographic misorientations of the two grains, and a near-boundary layer on each side of the grain boundary core. Y ions in these near-boundary layers are adjacent on one side to α-Al$_2$O$_3$ and on the other to the grain boundary core region.

Other phenomena related to dopant grain boundary supersaturation have also been reported. Gruffel et al. found that grain growth of Y doped alumina depends on the grain boundary Y concentration [31], with Y grain boundary saturation causing a high grain growth rate. This implies that the Y grain boundary saturation may enhance the grain boundary mediated mass transport. Consistent with this argument is the observation by Lartigue et al. that the creep strain rate shows a flat dependence on the grain size after the saturation of the grain boundary with the dopant [11]. From this, they have postulated that the Y grain boundary saturation induces a high concentration of defects in the vicinity of grain boundary. Wang et al. have observed for Nd doped α-Al$_2$O$_3$ that abnormal grain growth occurs when grain boundaries are saturated with Nd. Similar

phenomena have also been reported by Baik et al for Ca and Si doped α-Al_2O_3 [54,55]. These observations are not fully understood, particularly in light of the classical theory of solute drag which predicts that the grain boundary mobility should decrease as the grain boundary dopant concentration increases [56].

These discussions are also relevant for microstructural design of materials with properties improved by dopant grain boundary segregation. During the high temperature service of a component, a dynamical grain growth will induce an overall increase of dopant concentration in grain boundary, and this may finally lead to the supersaturation of the grain boundary with the segregants. This would likely induce instability of the materials microstructure and properties. Therefore, from the point of view of materials microstructural design, it is always desirable that a high concentration of dopant be used such that a second phase is precipitated which will absorb the dopant in excess of the grain boundary equilibrium concentration. This is consistent with the observation that creep resistance of 100 ppm Y or Nd doped alumina (no precipitates) is the same as that when the alumina is doped with Y or Nd at 1000 ppm (with YAG precipitates).

V.   Conclusions

The sequential occupation of α-Al_2O_3 grain boundaries by Y is characterised by three compositional regimes: dilute to saturated, supersaturated, and equilibrium with YAG precipitates. EXAFS data indicate at a dilute concentration that the grain boundary segregated Y and Zr ions preferentially occupy the sites in the grain boundary core region, which is characterized by a well defined dopant (Y, Zr)-O nearest neighbor coordinations, but the dopant (Y, Zr)-cation next nearest neighbor coordination is changing from site to site either within the same boundary or within different boundaries. The dopant (Y, Zr)-oxygen nearest neighbor bond length in the grain boundary, on average, is fully relaxed to that in the dopant cation parent oxides. However, the dopant (Y, Zr)-O nearest neighbor coordination number is ~ 30% smaller than that in their parent oxides. Structurally, the Y supersaturated grain boundary may be viewed as divided into three layers, a core layer within which the local structural environment around Y is dominated by short range ordering (nearest neighbor shell ordering), and two near-boundary layers within which the Y ions are in substitutional sites.

Acknowledgements

References

[1] J. D. Rittner and D. N. Seidman, Acta Mater., **45**, 3191-202(1997).

[2] C. W. Li and W. D. Kingery, pp. 368-378 in Advances in Ceramics, Vol.10, Structure and Properties of MgO and Al_2O_3 Ceramics. Edited by W. D. Kingery, American Ceramic Society, Columbus, OH, 1984.

[3] A. M. Thompson, K. K. Soni, H. M. Chan, M. P. Harmer, D. B. Williams, J. M> Chabala, and R. Levi-Setti, J. Amer. Ceram. Soc., **80**, 373-376 (1997).

[4] W. C. Johnson, Metall. Trans. A, **8A**, 1413-1422 (1977).

[5] E. D. Hondros and M. P. Seah, Inter. Met. Rev., **22**, 262-301 (1977).

[6] M. L. Gall, A. M. Huntz, B. Lesage, C. Monty, and J. Bernardini, J. Mater. Sci., **30**, 201-211 (1995).

[7] J. D. French, J. Zhao, M. P. Harmer, H. M. Chan, and G. A. Miller, J. Amer. Ceram. Soc., 77, 2857-2865 (1994).

[8] F. Wakai, T. Nagano, and T. Iga, J. Amer. Ceram. Soc., **80**, 2361-2366 (1997).

[9] J. Cho, M. P. Harmer, H. M. Chan, J. M. Rickman, and A. M. Thompson, J. Amer. Ceram. Soc., **80**, 1013-1017 (1997).

[10] S. Lartigue, C. Carry, and L. Priester, J. Phys. (Paris), **C1, 51**, 985-990 (1990).

[11] H. Yoshida, Y. Ikuhara, and T. Sakuma, J. Mater. Res., **13**, 2597-601(1998).

[12] S. Lartigue, L. Priester, F. Dupau, P. Gruffel, and C. Carry, Mater. Sci. Eng., **A164**, 211-215 (1993).

[13] J. Cho, H. M. Chan, M. P. Harmer, and J. M. Rickman, J. Amer. Ceram. Soc., **81**, 3001-3004 (1998).

[14] M. A. Gulgun, V. Putlayev, and M. Ruhle, J. Amer. Ceram. Soc., in press.

[15] Y. Li, C. M. Wang, H. M. Chan, J. M. Rickman, M. P. Harmer, J. Chabala, K. L. Gavrilov, and R. Levi-Setti, J. Am. Ceram. Soc., in press.

[16] R. F. Cook and A. G. Schrott, J. Amer. Ceram. Soc., **71**, 50-58 (1988).

[17] R. I. Taylor, J. P. Coad, and R. J. Brook, J. Amer. Ceram. Soc., **57**, 539-540 (1974).

[18] J. Bruley, J. Cho, H. M. Chan, M. P. Harmer, and J. M. Rickman, J. Am. Ceram. Soc., in press.

[19] D. R. Clarke, J. Amer. Ceram. Soc., **63**, 339-341 (1980).

[20] M. K. Loudjani, J. Roy, and A. M. Huntz, J. Amer. Ceram. Soc., **68,** 559-562 (1985).

[21] M. K. Loudjani, A. M. Huntz, and R. Cortes, J. Mater. Sci., **28,** 6466-6473 (1993).

[22] K. Kaneko, T. Gemming, I. Tanaka, and H. Mullejans, Phil. Mag. A, **77,** 1255-1272 (1998).

[23] W. D. Kaplan, H. Mullejans, M. Ruhle, J. Rodel, and N. Claussen, J. Amer. Ceram. Soc., **78,** 2841-2844 (1995).

[24] C. Tang, P. Georgopoulos, and J. B. Cohn, J. Amer. Ceram. Soc., **65,** 625-629 (1982).

[25] P. Li, I. W. Chen, and J. E. Penner-Hahn, J. Amer. Ceram. Soc., **77,** 118-128 (1994).

[26] K. L. Kavanagh, and G. S. Cargill III, Phys. Rev. B, **45,** 3323-3331 (1992).

[27] M. K. Loudjani and R. Cortes, J. Euro. Ceram. Soc., **19,** 2659-66 (1999).

[28] C. M. Wang, J. Cho, J., H. M. Chan, M. P. Harmer, and J. M. Rickman, J. Am. Ceram. Soc., submitted.

[29] C. M. Wang, G. S. Cargill III, M. P. Harmer, H. M. Chan, and J. Cho, Acta Mater., **47,** 3411-22(1999).

[30] C. M. Wang, G. S. Cargill III, H. M. Chan, and M. P. Harmer, Acta Mater., in press, 2000.

[31] P. Gruffel and C. Carry, J. Euro. Ceram. Soc., **11,** 189-99(1993).

[32] G. Cliff and G. W. Lorimer, J. Microsc., **103,** 203-16 (1975).

[33] U. Alber, H. Mullehans, and M. Ruhle, Ultramicroscopy, **69,** 105-16 (1997).

[34] J. J. Rehr, J. Mustre de Leon, S. I. Zabinsky, and R. C. Albers, J. Am. Chem. Soc., **113,** 5135-5140 (1991).

[35] B. K. Teo, EXAFS: Basic Principles and Data Analysis, Springer-Verlag, New York, 1986.

[36] J. Cho, Ph. D. Thesis, Lehigh University, 1998.

[37] W. Y. Ching, Y. N. Xu, and M. Ruhle, J. Amer. Ceram. Soc., **80,** 3199-3204 (1997).

[38] M. Exner and M. W. Finnis, Mater. Sci. Forum, **207-209,** 225-228 (1996).

[39] P. R. Kenway, J. Amer. Ceram. Soc., **77,** 349-355 (1994).

[40] T. Hoche, P. R. Kenway, H. J. Kleebe, M. Ruhle, and P. A. Morris, J. Amer. Ceram. Soc., **77,** 339-348 (1994).

[41] S. D. Mo, W. Y. Ching, and R. H. French, J. Amer. Ceram. Soc., **79,** 627-633 (1996).

[42] C. A. Handwerker, J. M. Dynys, R. M. Cannon, and R. L. Coble, J. Am. Ceram. Soc., **73,** 1371-77(1990).

[43] D. McLean, Grain Boundaries in Metals, pp.116-49, Clarendon Press, Oxford, 1957.

[44] R. C. McCune, W. T. Donlon, and R. C. Ku, J. Am. Ceram. Soc., **69,** C-196-C199 (1986).

[45] J. D. Cawley and J. W. Halloran, J. Amer. Ceram. Soc., **69,** C-195-96(1986).

[46] C. D. Terwilliger and Y. M. Chiang, Acta Metall. Mater., **43,** 319-28(1995).

[47] E. A. Colbourn, W. C. Mackrodt, and P. W. Tasker, J. Mater. Sci., **18,** 1917-24(1983).

[48]   N. Ishizawa, T. Miyata, I. Minato, F. Marumo, and S. Iwai, Acta Crystal., **B36,** 228-230 (1980).

[49]   M. Bonnet and A. Delapalme, Acta Crystal., **A31,** 264-265 (1975).

[50]   F. Euler and J. A. Bruce, Acta Crystal., **19,** 971-978 (1965).

[51]   D. K. Smith and H. W. Newkirk, Acta Crystal., **18,** 983-991 (1965).

[52]   C. J. Howard, E. H. Kisi, R. B. Roberts, and R. J. Hill, J. Amer. Ceram. Soc., **73,** 2828-2833 (1990).

[53]   R. D. Shannon, Acta Crystallogr., **A32,** 751-767 (1976).

[54]   Il-Joon Bae and S. Baik, J. Amer. Ceram. Soc., **80,** 1149-456(1997).

[55]   S. I. Bae and S. Baik, J. Amer. Ceram. Soc., **76,** 1065-67(1993).

[56]   S. J. Bennison and M. P. Harmer, pp.13-49 in Ceramic Transactions, Vol.7, Sintering of Advanced Ceramics. Edited by C. A. Handwerker, J. E. Blendell, and W. A. Kaysser. American Ceramic society, Westerville, OH, 1990.

Table and Figure Captions

Table I   Crystallographic Data for Model Compounds

Table II   Fitting Results for Doped Materials

Fig.1   Comparison of the creep behavior of 100 ppm Y or 100 ppm La doped alumina [33].

Fig.2   SEM images of Y-doped and Zr-doped Al_2O_3 samples: (a) 100 ppm Y_2O_3 doped Al_2O_3; (b) 100 ppm ZrO_2 doped Al_2O_3; and (c) 1000 ppm Y_2O_3 doped Al_2O_3. Grain boundaries are visible because of thermal grooving. In (c) some of the YAG precipitates are indicated by arrows.

Fig.3   (a) Grain boundary Y excess measured by STEM as a function of the grain size-normalized doping concentration, which shows three consecutive regions: I dilute; II supersaturated; III equilibrium. (seg. stands for segregation).

Fig.4   The STEM images and the Y EDX maps showing the Y distribution in the grain boundary which compositionally corresponds to the grain boudnary is supersaturated with Y ((a) and (b)), and the grain boudnary is in equilibrium with YAG ((c) and (d)). In the EDX mapping, the electron beam diameter is optimised to 1 nm, and the mapping area is 160 x 160 nm^2 with a total pixels number of 128 x 128.

Fig. 5   Fourier transform magnitude of the EXAFS spectra of 100Y, 100Zr, Y_2O_3, and monoclinic ZrO_2. α represents the distance shift due to the phase shift function in the Fourier transformation [29].

Fig.6   The radial distribution functions around Y for Y segregated to α-Al_2O_3 grain boundary at a concentration of both dilute and supersaturation, as well as that calculated according to the model structure. It reveals that Y grain boundary supersaturation induces an obviously identifiable Y-cation peak and which follows the features of that when the Y substitute Al while relaxing all the Y-O distance to that in Y_2O_3 [30].

Table I   **Crystallographic Data for the Model Compounds**

Compound	Structure	Cation-oxygen bond length (Å)	Coordination number	Ref.
Al_2O_3	Rhombohedral	3x1.852; 3x1.972		48
		average: 6x1.912	6	
Y_2O_3	Cubic	6x2.239; 6x2.289		
		6x2.273; 6x2.333		
		average: 6x2.284	6	49
$Y_3Al_5O_{12}$	Cubic	4x2.289; 4x2.412		
		average: 8x2.351	8	50
ZrO_2	Monoclinic	1x2.051; 1x2.057; 1x2.151; 1x2.162;		
		1x2.189; 1x2.220; 1x2.284		
		average: 7x2.159	7	51, 52

Ionic radii(Å): O^{2-}(6):1.40; Al^{3+}(6):0.51; Y^{3+}(6):0.90; Zr^{4+}(7):0.78, in each case the coordination number is given in parentheses [53].

Table II   **Fitting Results for The Doped Materials** [#]

	100 Y	100Zr	1000Y
	Y-O	Zr-O	Y-O
Mean radial distance(Å): R	2.30 ± 0.01	2.14 ± 0.01	2.36 ± 0.01
Coordination number: N	4.2 ± 0.5	5.0 ± 0.5	7.5 ± 0.7
Distance dispersion $(Å^2):\sigma^2$	0.009 ± 0.001	0.010 ± 0.001	0.008 ± 0.0008

[#] The uncertainties in fitted parameters correspond to 10% increase in mean square difference between experimental and model $k^3\chi(k)$ functions, when the other parameters are allowed to vary.
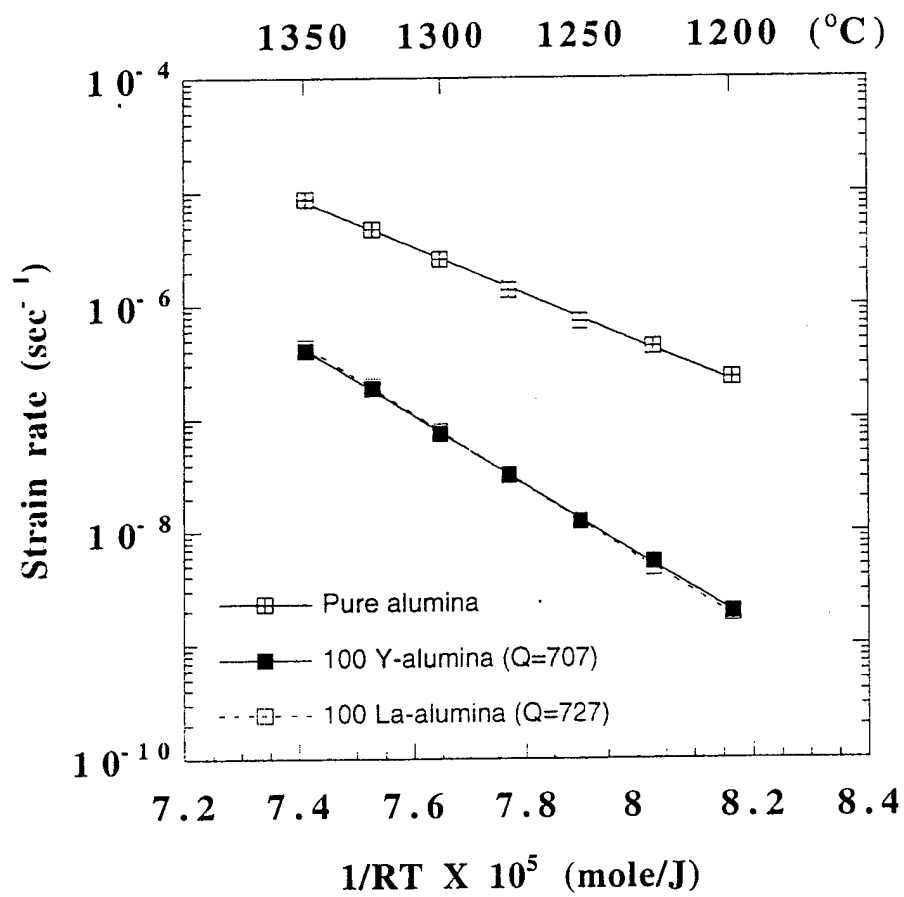
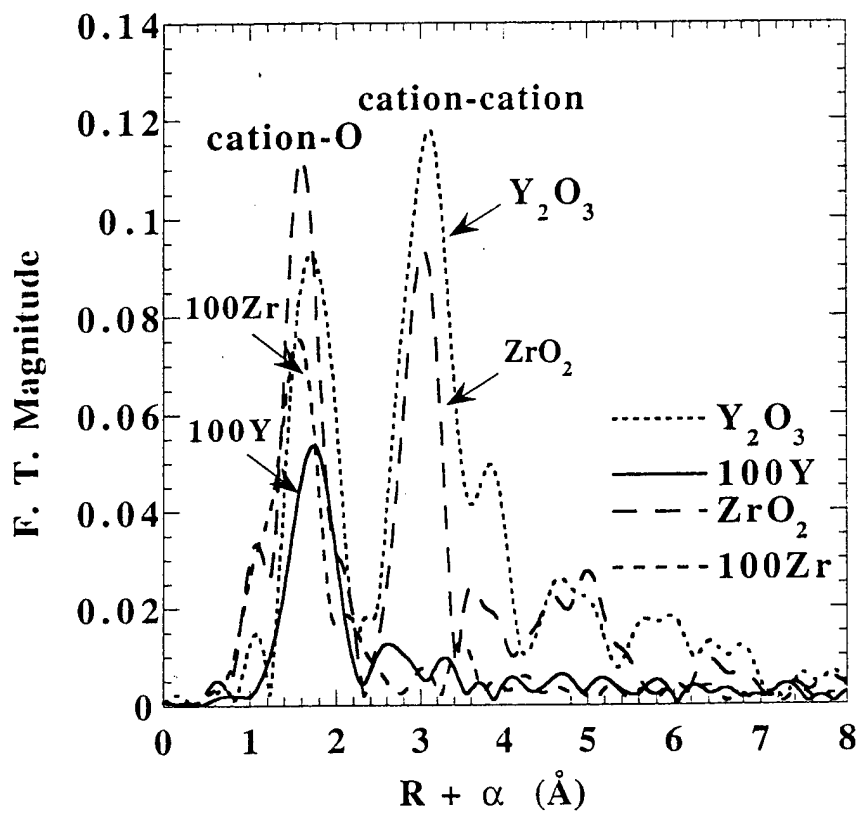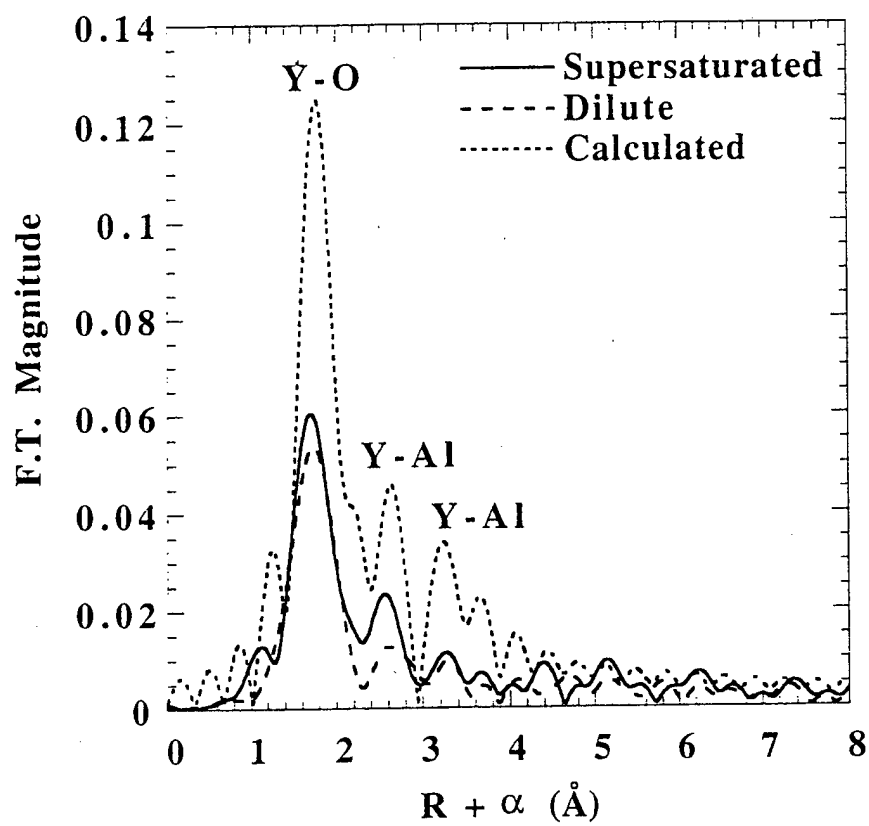Fig.1
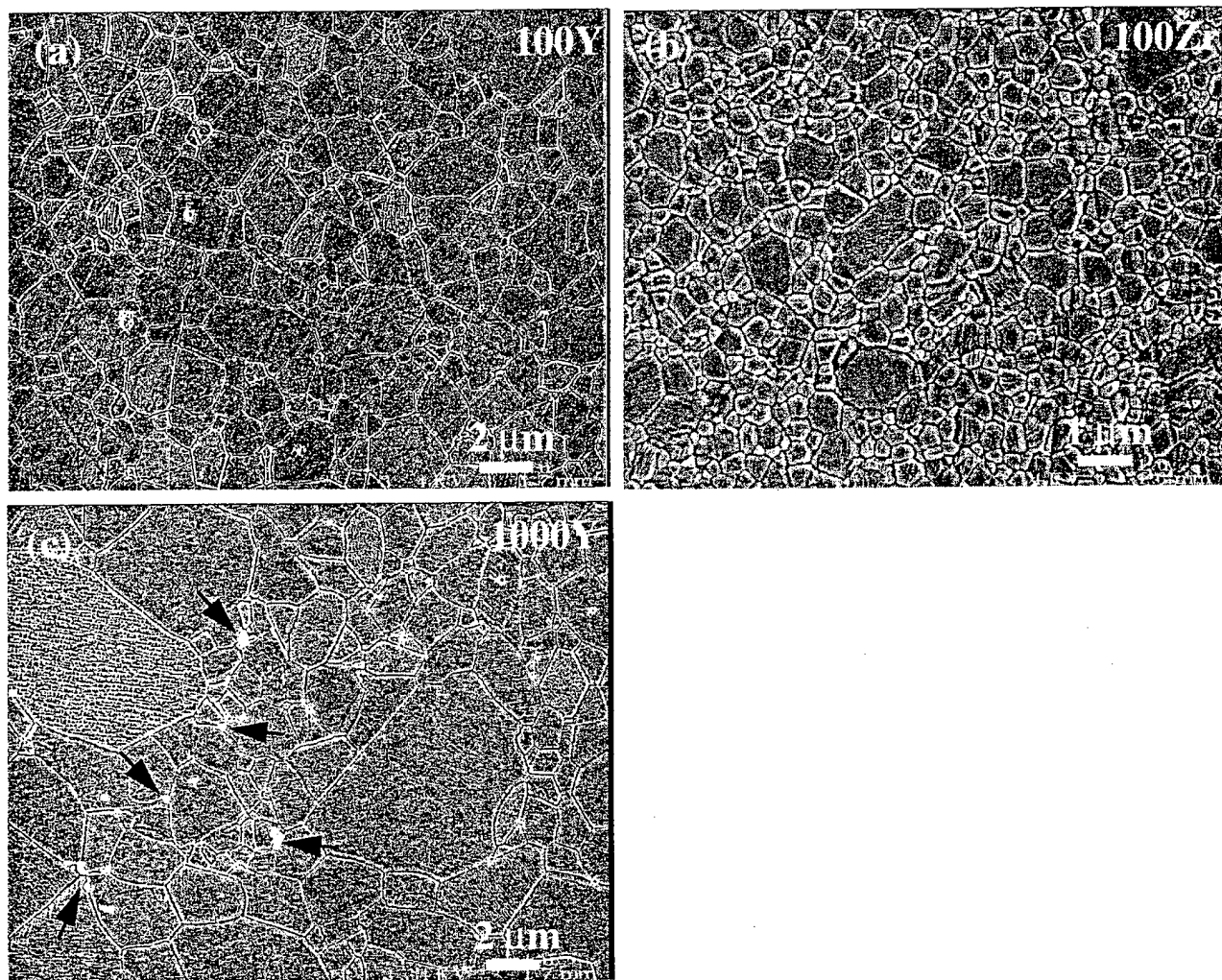
Fig.2
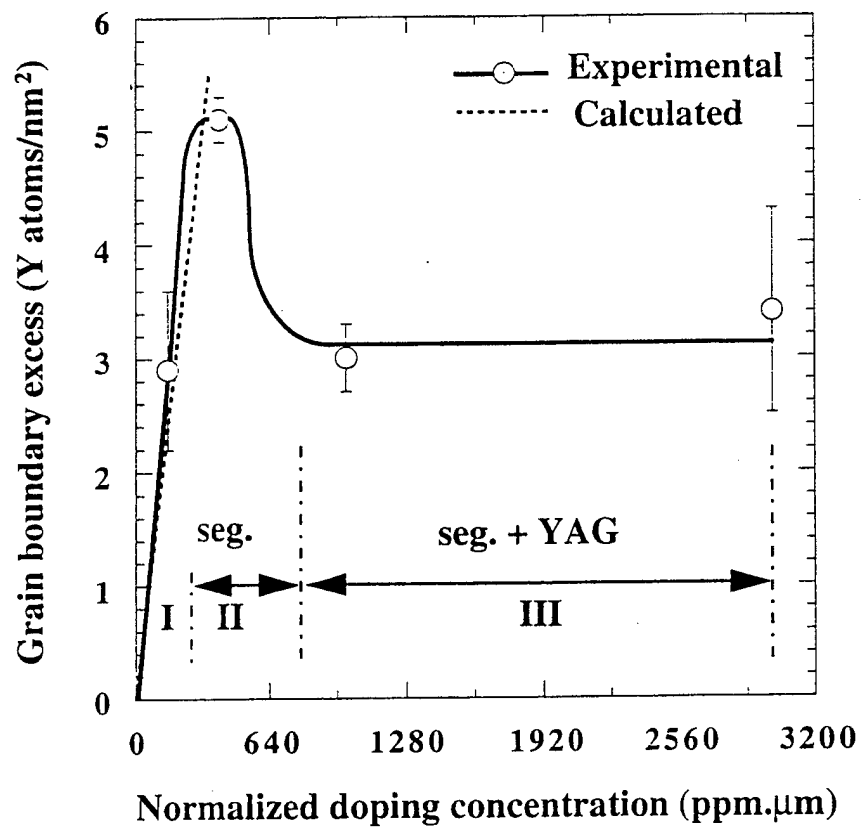
Fig.3
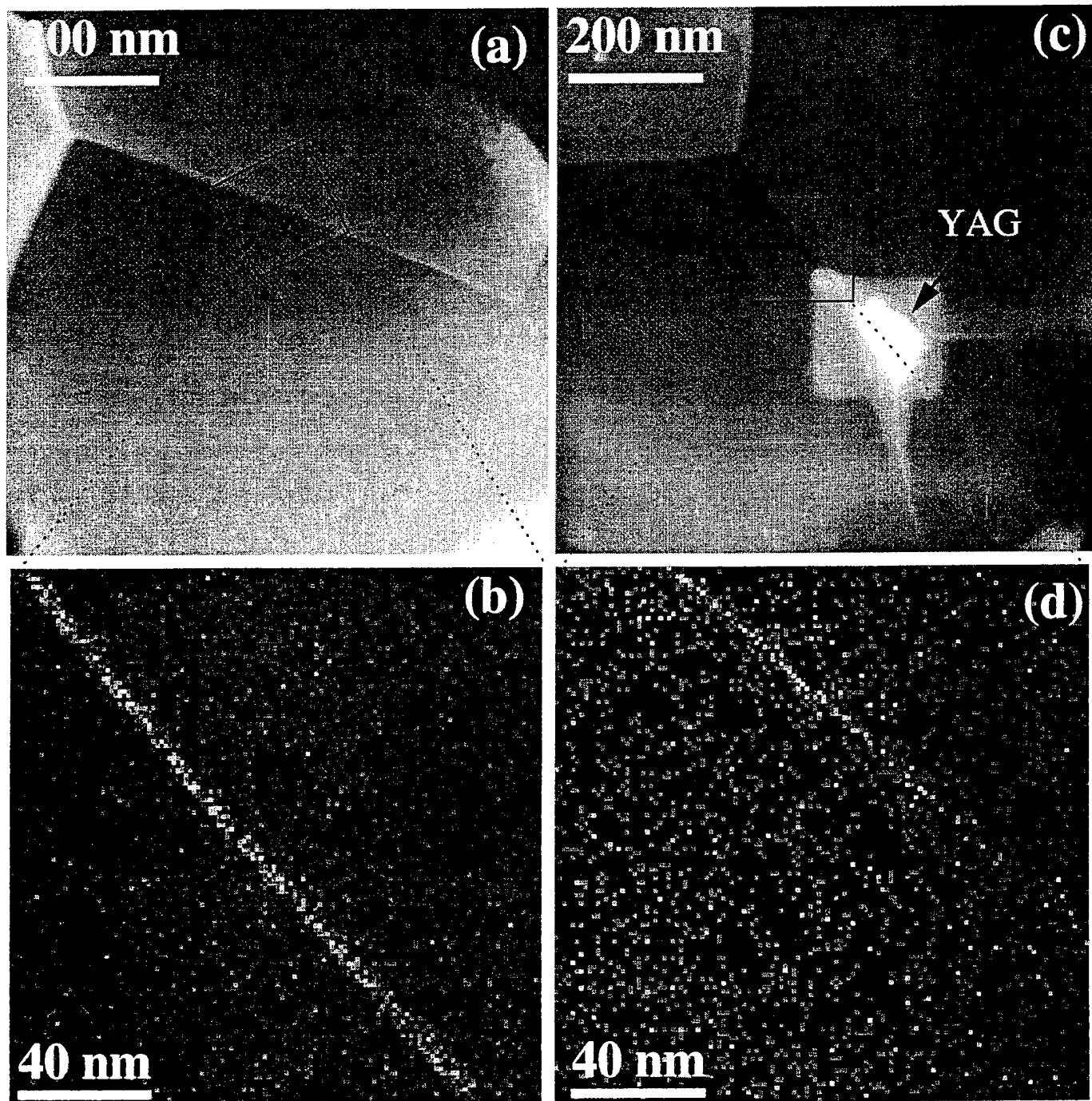
Fig.4

Fig.5

Fig.6

3.7   Influence of Dopant Concentration on Creep Properties of Nd_2O_3 Doped Alumina

By

C. M. Wang, J. Cho, H. M. Chan, M. P. Harmer, and J. M. Rickman

INFLUENCE OF DOPANT CONCENTRATION ON CREEP PROPERTIES OF Nd$_2$O$_3$ DOPED ALUMINA

Chong-Min Wang[*], Junghyun Cho[*], Helen M. Chan[*], Martin P. Harmer[*], and Jeffrey M. Rickman

Materials Research Center, Lehigh University

Bethlehem, PA 18015

Abstract

The microstructural features and tensile creep behavior of Al$_2$O$_3$ doped with Nd$_2$O$_3$ at levels ranging from 100 to 1000 ppm (Nd/Al atomic ratio) have been systematically investigated. Compositional mapping using both high resolution STEM (scanning transmission electron microscopy) and SIMS (secondary ion mass spectroscopy) revealed that for all the compositions studied, the Nd^{3+} ions were strongly segregated to the alumina grain boundaries. Microstructural observations revealed that the solubility of Nd$_2$O$_3$ was between 100 and 350 ppm. Tensile creep tests were carried out over a range of temperatures (1200 °C - 1350 °C) and stresses (20 - 75 MPa). Evaluation of both the stress (n) and grain size (p) exponents was carried out. In selected experiments, controlled grain growth anneals were used to enable creep testing of samples of the same average grain size, but different Nd concentration. It was found that independent of dopant level, the Nd additions resulted in a reduction of the creep rate by 2 - 3 orders of magnitude, compared to undoped alumina. The value of the apparent creep activation energy was observed to increase with increasing dopant concentration, and then saturate at dopant levels exceeding the solubility limit. Overall, the results of the present study are consistent with a creep inhibition mechanism whereby oversized segregant ions reduce grain boundary diffusivity by a site-blocking mechanism.

---

[*]   Member, American Ceramic Society

I. Introduction

In recent years, a series of studies has emerged which have established the beneficial role of rare-earth dopant ions on the creep behavior of alumina [1-7]. Thus work by Lartigue _et al._ [1] and Robertson _et al._ [8] showed a reduction in the creep rate of magnesia-doped alumina with the addition of Y, by factors of 5 and 15, respectively. The study of Cho _et al._ [4] demonstrated a more dramatic effect, whereby doping with Y or La resulted in improvements in the steady state strain rate of 2 - 3 orders of magnitude (versus undoped alumina). In related work, Wakai _et al._ [9, 10] have observed that the addition of Zr to alumina (at levels both above and below the solubility limit) reduces the creep rate by a factor of 15.

More recently, Li _et al._ [7] have reported the additional benefit that can derive from co-doping with ions of disparate sizes. These workers showed that for Nd/Zr codoped alumina, the enhancement in creep resistance was greater than was achieved by doping with either Nd or Zr alone. The study of Li _et al._ also highlighted the influence of ionic size on the creep rate; thus doping with Sc^{3+} (0.74 Å) or Zr^{4+} (0.72 Å), whilst still beneficial, was markedly less effective than doping with either La^{3+} (1.03 Å) or Y^{3+} (0.90 Å). Although previous work has suggested that the creep inhibition is primarily a solid solution effect [7, 11], the influence of dopant concentration on creep behavior has not been systematically studied. The objective of the present study, therefore, was to address this issue with regard to Nd doping. In particular, it was hoped that any changes in behavior for the different solute levels would lend further insight to the creep mechanism.

II.   Experimental

(1) Specimen Preparation

The starting materials were ultra pure α-Al_2O_3 powder (AKP-53, 99.995%, mean particle size of 0.35 μm and specific surface area of 12.7 m^2/g, Sumitomo Chemical America, New York) and neodymium nitrate of semiconductor grade. Alumina samples with the following nominal Nd_2O_3 dopant levels were prepared: 100, 350 and 1000 ppm (Nd/Al atomic ratio). Details of the

powder processing and doping procedures have been described elsewhere [4, 7]. Dense billets (> 99.5 %) were obtained by hot-pressing in a graphite die of 76.2 mm in diameter at 50 MPa for 30 min. in vacuum. The hot-pressing temperatures (which were tailored to achieve microstructures with comparable average grain sizes for the different compositions) were as follows: pure alumina (1350 °C), 100 ppm (1425 °C), 350 ppm Nd and 1000 ppm Nd (1450 °C).

(2) Creep testing

Dogbone tensile specimens were machined from the hot-pressed billets according to specifications described by French and Wiederhorn [12]. The specimen gauge lengths were defined by two SiC flags attached to the specimen, and measured using a laser extensometer (LaserMike Inc., Dayton OH) to an accuracy of 1 μm. For each specimen, possible flag slippage was monitored by measuring the projected flag thickness both before and after the creep test. If the change in projected flag thickness was more than 20 μm, the creep data were disregarded.

Previous work [4] had shown that a pre-annealing of the creep specimens while under a slight load (5 MPa) significantly reduced the extent of primary creep. The microstructure was examined both prior to and after the pre-annealing treatment, and no change in grain size was detected. Therefore, prior to creep testing, all the samples were annealed at 1250 °C for 24 hours under an applied stress of 5 MPa. Tensile creep tests were performed in air whereby the sample was subjected to a constant load using either a lever arm or hydraulic testing machine (Applied Test Systems, Butler, PA). Testing was carried out in the temperature range of 1200 °C - 1350 °C, with applied stresses ranging from 20 to 75 MPa. Three types of creep test were performed: (i) standard stress rupture test at 1275 °C and 50 MPa, (ii) a temperature-step test, in which the stress was nominally kept constant, but the temperature was altered periodically, (iii) a stress-step test, in which the temperature was held constant, but the stress was varied. The latter two types of test enable the measurement of the strain rate, under a given set of test conditions, two to three times per specimen. For the range of stress and temperatures studied, no dependence of the steady state strain rate on strain history was observed.

The values of the stress exponent (n) and inverse grain size exponent (p) as defined by the following constitutive equation were also evaluated.

$$\dot{\varepsilon} = A(\frac{\sigma^n}{d^p})exp(-\frac{Q}{RT}) \tag{1}$$

where $\dot{\varepsilon}$ is the strain rate, d is the grain size, σ is the applied stress, A is a constant of proportionality determined by the slowest diffusive species along the fastest diffusion path, Q is the activation energy, R is the gas constant, and T is the absolute temperature. In order to obtain the stress exponent (n), stress-step testing was used to evaluate the steady state strain rate at different stresses (at constant temperature and grain size). To evaluate the grain size exponent (*p*), the as-hot-pressed materials were annealed at 1450 °C and 1500 °C for different times to obtain a range of grain sizes for each composition; the specimens were subsequently tested at 1275 °C, under a constant tensile loading of 50 MPa until rupture.

Two distinct approaches were adopted to assess the dependence of creep resistance on the grain boundary dopant concentration. In the first case, samples of the different dopant compositions were annealed to the same average grain size (2.4 ± 0.2 μm), and stress-rupture tests were conducted at 1275 °C under an applied stress of 50 MPa. In the second case, the creep behavior of samples with different grain sizes and dopant levels was normalized to the same grain size using an experimentally determined value of the grain size exponent (p).

(3) Microstructure analysis and compositional mapping

The microstructures of specimens both before and after creep testing were evaluated by polishing to a 1 μm diamond finish and thermally etching at 1400 °C for 1 h. Grain size was determined from SEM micrographs using the linear intercept method. The distribution of the Nd dopant ions was characterized both by imaging secondary-ion mass spectrometry (SIMS) (carried out at U. Chicago) and analytical electron microscopy (AEM). Details of the SIMS procedure have been given elsewhere [6]. In the case of the AEM, thin foils of both as-hot-pressed and

deformed materials were prepared by standard techniques, including ultrasonic cutting, thinning, and dimpling to a foil thickness of 120 µm, followed by ion beam milling to perforation. A thin layer of carbon was evaporated on the specimen to eliminate charging. Compositional mapping of the dopant distribution was carried out on a dedicated STEM (VG Microscopes, Model 603, West Sussex, UK) operating at 300 keV, fitted with a windowless Si(Li) detector (Links Systems, Boston, MA). The probe size was of the order of 0.6 nm, yielding an areal resolution of ~ 1 nm^2.

III.   Results

(1) Microstructure and Nd segregation behavior

SEM micrographs of the polished and thermally etched surfaces of the as-hot-pressed samples are shown in Figure 1. The grains of the 100 ppm doped material are equiaxed, and exhibit a uniform size distribution, with an average grain size of ~ 1.5 µm (see Fig. 1 (a)). No second phase precipitates were observed for this composition, either in the SEM or the TEM. In contrast, Nd-rich precipitates were occasionally observed at grain boundary triple points in the 350 ppm Nd doped material. The grain structure also differed from the 100 ppm specimen in that interspersed in a background of fine (d ~ 1.5 µm) grains, were larger grains of up to 10 µm in size (Fig. 1(b)). From the micrographs, it was estimated that the large abnormal grains made up ~ 3 % (by volume) of the structure. The microstructure of the 1000 ppm doped material was the most inhomogeneous of the three compositions, exhibiting essentially a bimodal grain size distribution, with clusters of fine and coarse grain size regions. For this dopant level, numerous second phase particles were visible, which were preferentially situated in the fine grain size regions (Fig. 1(c) and (d)). Fig.2 shows SIMS maps of the Nd distribution in the as-hot-pressed materials; the regions of brighter contrast correspond to a locally higher Nd content. It is clear from the maps that Nd^{3+} ions are strongly segregated to the grain boundaries. The marked segregation behavior, even at the 100 ppm dopant level, confirms the very low solubility of Nd in the alumina lattice.

TEM observation revealed that the microstructures of the crept materials were characterized by the occasional dislocation array, and two distinct forms of cavity (Fig.3 and

Fig.4). The first of these comprised intragranular pores which often exhibited a faceted morphology (Fig.3(a), Fig.4(a)). Comparison of the deformed and undeformed materials established that these intragranular pores were residual pores following densification. The other type of cavity tended to be triangular in shape, and located primarily at grain boundary triple junctions (Fig.3(b)). For the 1000 ppm sample (which essentially exhibited a bimodal grain size), these cavities occurred preferentially at the interface between large abnormal grains, and surrounding small grains. Similar cavitation features have also been reported by Chokshi and Porter in crept alumina codoped with 250 ppm MgO and 250 ppm ZrO_2, and possessing a bimodal grain size distribution [14]. A theoretical explanation for this cavitation phenomenon has been developed by Dalgleish et al. [15] and Chokshi et al. [14], predicting that a localized doubling of the effective stress at the coarse-grained clusters, therefore inducing cavitations in these regions. Dedicated STEM analysis of dopant distribution confirmed the SIMS findings, namely that Nd is mainly segregated to grain boundaries (see Fig. 5). No evidence, however, was obtained for segregation of Nd ions to dislocation cores.

(2) Creep behavior

The stress rupture tests revealed that independent of dopant level, the general features of the creep deformation behavior were similar, with well-defined primary, steady-state, and tertiary deformation stages. Typically for the 100 ppm doped material, the creep rupture strain was ~ 15%, for the 350 ppm doped material, it was ~ 8%, and for the 1000 ppm doped, it was ~ 3%.

The strain rate data (at a constant tensile stress of 50 MPa) for the doped compositions are shown in Fig. 6; corresponding data for undoped alumina [4] are included for reference. The apparent activation energy for tensile creep was derived from the slope of the curves, and is plotted as a function of dopant concentration in Fig.7. For comparison, values of the activation energy obtained by densification experiments on the same powder compositions are also plotted (Note that these latter experiments will be discussed in more detail in a separate paper [13]). It can be seen that there is reasonable agreement between the two sets of data, and both suggest a

trend whereby the activation energy first increases with increasing Nd content, and then saturates at a Nd dopant level around 350 - 400 ppm.

The effect of the stress on the steady-state strain rate is shown in Figure 8(a); the value of the stress exponent n was determined to be 2.1, 1.8 and 2.4 for the 100, 350 and 1000 ppm doped compositions, respectively. Hence for the range of stress tested (20 - 75 MPa), the stress exponent falls around 2 for all three dopant concentrations. This result is consistent with studies on other dopant systems obtained by the present group [2, 4, 7, 16], and work on undoped alumina by Robertson *et al.* [8]. As described earlier, the grain size exponent was determined by creep testing samples of different starting grain size at constant stress (50 MPa) and temperature (1275 °C). Unfortunately, in the case of the 1000 ppm specimen, annealing treatments did not provide a sufficient increase in the average grain size to enable the evaluation of the grain size exponent. For the 100 ppm and 350 ppm doped samples, however, the value of the grain size exponent was found to be 3.4 and 3.7 respectively (Fig. 8(b)). It should be noted that in the evaluation of the grain size exponent we use the average grain size acquired by the linear intercept method. In the case of the 350 ppm Nd doped alumina sample, there exists some grains which have a rather large grain size (> 10 μm). Consequently, one may question the validity of the linear intercept method for obtaining the average grain size, and therefore the grain size exponent, p, in the present context. However, upon compiling the grain size distribution for the 350 ppm Nd-doped sample (Fig. 9), it was evident that these outliers in the distribution comprise less than 3 vol% and are spatially isolated in the system. Thus, this small proportion of large grains are not expected to influence the strain rate of the material significantly. Detailed discussion of the effect of grain size distribution on the creep strain rate will be discussed in a separate paper.

The effect of Nd dopant concentration on the creep behavior was evaluated by two distinct methods. Figure 10 shows the results of one of these approaches, in which creep data for the as hot-pressed 100 ppm and 350 ppm samples were corrected to the grain size of the 1000 ppm sample using the grain size exponent determined previously. Using this approach, the creep data of the doped materials form a band which is distinct from that of the undoped alumina.

On closer observation, it can also be seen that the slope of the creep curves for the doped compositions reflect the difference in activation energy discussed earlier, hence there is a crossover in the behavior at ~ 1275 °C. Thus depending on the creep temperature, the higher dopant level may be more or less beneficial in terms of the strain rate. In the second approach, the steady state strain rate was compared for specimens of different dopant compositions which had been annealed to achieve similar average grain sizes (2.4 ± 0.2 μm). Figure 11 shows that the degree of improvement in creep resistance is essentially independent of dopant composition. It is recognized, however, that (coincidentally) the conditions tested (50 MPa, 1275 °C) correspond to the region of the 'cross-over' of the strain rate curves (see Fig. 10), hence any dispersion in the strain rates is minimized. Nonetheless, the two sets of data are entirely consistent, and taken as a whole, they show that the Nd dopant concentration (over the range of 100 – 1000 ppm) does not have a strong effect on the degree of creep inhibition.

IV.   Discussion

The present work demonstrates that singly doping alumina with Nd lowers the tensile creep rate by 2 - 3 orders of magnitude. The influence of Nd is thus consistent with that of Y and La [4]; a result not altogether unexpected, given that the ionic radius of Nd (0.98 Å) is intermediate between that of Y (0.90 Å) and La (1.03 Å). This study, was the first however, in which the Nd dopant concentration was systematically studied. The results showed that the creep behavior, when normalized to account for grain size, is practically independent of the Nd content. Since the dopant levels studied spanned the solubility limit, this confirms that the creep inhibition mechanism is primarily a solid solution effect. The relative insensitivity of the creep behavior to dopant concentration is interesting, and would seem to point to a saturation of Nd^{3+} ions at the grain boundary, and hence an upper limit to their effectiveness as obstacles to grain boundary diffusion. The situation is more complex, however, because the present study also shows that the apparent activation energy (derived from both creep and densification experiments) increases with increasing dopant level. One could speculate that the increase in the overall Nd content correlates with an increase in the grain boundary concentration, and that interaction between the Nd occupied sites causes an initial increase in the activation energy. At

the grain boundary saturation level, however, no further increases would occur. Evidence to support this general picture is provided by ongoing AEM and EXAFS (extended X-ray absorption fine structure) studies [17, 18], which suggest that the local atomic environment of grain boundary segregated Y ions changes with Y concentration. Similarly, in the Al_2O_3-ZrO_2 composite system, Wang and Raj found that the apparent activation energy of alumina during sintering increased initially with increasing ZrO_2 content (up to 5 vol% of ZrO_2), after which the apparent activation energy reached a saturation value [19]. It should be noted, however, that the trend of increasing activation energy with dopant level is in contrast to the work of Cho [16], who reported that in the case of La doping, the activation energies for 100 ppm and 500 ppm samples were approximately the same (776 and 800 kJ/mol, respectively). For Y-doped alumina, however, Cho [16] observed that the activation energy was lower for a 1000 ppm doped sample than a 100 ppm sample (685 versus 832 kJ/mol). The reason(s) for this discrepancy are not well understood.

As put forward previously, it is believed that site-blocking of rapid grain boundary diffusive paths is the most logical explanation for the observed creep inhibition. The evidence supporting this mechanism (versus for example, interface control) has been discussed in previous work [11]. One compelling argument is that for the range of grain size, and stress and temperature conditions studied, it is widely accepted that grain boundary diffusion is the rate controlling step for alumina [20]. Furthermore, densification studies on doped aluminas have confirmed grain boundary diffusion to be rate controlling [21], and the present study has shown that the values of the activation energy determined from creep and densification experiments are very comparable. Finally, OIM (orientation image mapping) studies do not reveal a significant difference between either the grain boundary misorientation distribution, or the proportion of CSL (coincident site lattice) boundaries in Nd doped alumina versus undoped [22]. This would rule out, therefore, any possible role of the dopant ions in promoting particular boundaries with creep resistant properties. It is acknowledged, however, that the measured values of the grain size (p ~ 3-4) and stress exponent (n ~ 2), although once more consistent with previous work, cannot be reconciled with any generally accepted creep mechanism [20, 23-25].

In addition to its influence on the creep properties, the Nd dopant level also had a marked effect on the alumina grain structure. The study showed that with Nd concentrations in excess of the solubility limit, there was an increased tendency for abnormal grain growth. It should be emphasized that this phenomenon is not processing related, but rather due to the effect of grain boundary solute levels on the grain boundary mobility. Recent STEM and grain growth studies suggest that the onset of abnormal grain growth corresponds to a *supersaturation* of the solute at the alumina grain boundary; these results are reported in a separate paper [26].

V.   Conclusions

Doping Al_2O_3 with 100 ppm Nd_2O_3 (which is below the solubility limit) reduces the tensile creep rate by two to three orders of magnitude. Dopant levels in excess of the solubility limit (350 ppm, 1000 ppm) did not result in further substantial improvements in the creep, thus confirming that the beneficial influence of Nd is primarily a solid solution effect. The apparent creep activation energy was observed to increase with Nd content, and then saturate at $\sim$ 950 kJ/mol for Nd concentrations greater than the solubility limit. This trend was confirmed by activation energies derived from sintering experiments. The increase in activation energy (relative to undoped alumina) is probably attributed to site-blocking by the oversized Nd^{3+} ions, which segregate to the alumina grain boundaries. It is tentatively suggested that with increasing Nd concentration, the subsequent saturation in the activation energy corresponds to a greater likelihood of interaction between adjacent Nd occupied sites. Given that the grain structures were markedly less homogeneous in the case of the 350 and 1000 ppm dopant concentrations, the saturation in the creep benefit suggests an optimum dopant level where the grain boundary dopant concentration just exceeds the solubility limit. The results of the present study are completely consistent with creep studies carried out on other rare-earth dopant systems (Y, La), and once more suggest a site-blocking mechanism whereby the oversized dopant ions impede grain boundary diffusion.

Acknowledgments

References

[1]   S. Lartigue, C. Carry, and L. Priester, "Grain Boundaries in High Temperature Deformation of Yttria and Magnesia Co-doped Alumina," J. Phys.(Paris), C1-51, 985-90(1990).

[2]   J. D. French, J. Zhao, M. P. Harmer, H. M. Chan, and G. A. Miller, "Creep of Duplex Microstructure," J. Am. Ceram. Soc., 77, 2857-65(1994).

[3]   S. Korinek and F. Dupau, "Grain Boundary Behavior in Superplastic Mg-Doped Alumina with Yttria Co-doping," Acta Metall. Mater., 42, 293-302(1994).

[4]   J. Cho, M. P. Harmer, H. M. Chan, J. M. Rickman, and A. M. Thompson, "Effect of Yttrium and Lanthanum on The Tensile Creep Behavior of Aluminum Oxide," J. Am. Ceram. Soc., 80, 1013-17(1997).

[5]   A. M. Thompson, H. M. Chan, and M. P. Harmer, "Tensile Creep of Alumina-Silicon Carbide Nanocomposites," J. Am. Ceram. Soc., 80, 2221-28(1997).

[6]   A. M. Thompson, K. K. Soni, H. M. Chan, M. P. Harmer, D. B. Williams, J. M. Chabala and R. L. Setti, "Dopant Distribution in Rare-Earth-Doped Alumina," J. Am. Ceram. Soc., 80, 373-76(1997).

[7]   Y. Z. Li, C. M. Wang, H. M. Chan, J. M. Rickman, M. P. Harmer, J. M. Chabala, K. L. Gavrilov, and R. Lavi-Setti, "Codoping of Alumina to Enhance Creep," J. Am. Ceram. Soc., 82, 1497-504(1999).

[8]   A. J. Robertson, D. S. Wilkinson, and C. H. Caceres, "Creep and Creep Fracture in Hot-Pressed Alumina," J. Am. Ceram. Soc., 74, 9150-21(1991).

[9] F. Wakai, T. Nagano, and T. Iga, "Hardening in Creep of Alumina by Zirconium Segregation at the Grain Boundary," J. Am. Ceram. Soc., 80, 2361-66(1997).

[10] F. Wakai, T. Iga, and T. Nagano, "Effect of Dispersion of ZrO_2 Particles on Creep of Fine-Grained Alumina," J. Ceram. Soc. Jpn, 96, 1206-209(1988).

[11] J. Cho, C. M. Wang, H. M. Chan, M. P. Harmer, and J. M. Rickman, "Role of SegregationDopants on the Improved Creep Resistance of Aluminum Oxide," Acta Mater., 47, 4197-207(1999).

[12] J. D. French and S. M. Wiederhorn, "Tensile Specimens from Ceramic Components," J. Am. Ceram. Soc., 79, 550-52(1996).

[13] C. M. Wang, H. M. Chan, M. P. Harmer, and J. Rickman, "Densification Behavior and Microstructural Features of Alumina Doped with Different Level of Nd_2O_3," Submitted to J. Am. Ceram. Soc..

[14] A. H. Chokshi and J. R. Porter, "Cavity Development During Creep Deformaiton in Alumina with a Bimodal Grain Size Distribution," J. Am. Ceram. Soc., 70, 197-202(1987).

[15] B. J. Dalgleish, S. M. Johnson, and A. G. Evans, "High-Temperature Failure of Polycrystalline Alumina: I, Crack Nucleation," J. Am. Ceram. Soc., 67, 741-50(1984).

[16] J. Cho, Role of Rare-Earth Dopant on the Improved Creep Properties of Aluminum Oxide, Ph. D. Thesis, Lehigh University, 1998.

[17] C. M. Wang, G. S. Cargill III, M. P. Harmer, H. M. Chan, and J. Cho , "Atomic Structural Environment around Grain Boundary Segregated Y and Zr in Creep Resistance Alumina," Acta Mater., 47, 3411-22(1999).

[18] C. M. Wang, G. S. Cargill III, H. M. Chan, and M. P. Harmer, "Structural Features of Y-Saturated and Supersaturated Grain Boundaries in Alumina," Acta Mater., 48, 2579-91(2000).

[19] J. Wang and R. Raj, "Activation Energy for the Sintering of Two-Phase Alumina/Zirconia Ceramics," J. Am. Ceram. Soc., 74, 1959-63(1991).

[20] R. M. Cannon and R. L. Coble, "Review of Diffusional Creep of Al_2O_3," pp 61-100 in Deformation of Ceramic Materials, Edited by R. C. Bradt and R. E. Tressler, Plenum, New York, 1975.

[21] J. Fang, A. M. Thompson, M. P. Harmer, and H. M. Chan, "Effect of Y and La on The Sintering Behavior of Ultra-High-Purity Al_2O_3," J. Am. Ceram. Soc., 80, 2005-12(1997).

[22]   J. Cho, C. M. Wang, H. M. Chan, M. P. Harmer, and J. M. Rickman, "A Study of Grain Boundary Structure in Rare-Earth Doped Alumina Using EBKD Technique," submitted to J. Mater. Res..

[23]   P. A. Lessing and R. S. Gordon, "Creep of Polycrystalline Alumina, Pure and Doped with Transition Metal Impurities," J. Mater. Sci., 12, 2291-2302(1977).

[24]   F. R. N. Nabarro, "Deformation of Crystals by Motion of Single Ions, in Report of a Conference on The Strength of Solids," p231, Phys. Soc., London(1948).

[25]   C. Herring, "Diffusional Viscosity of A Polycrystalline Solid," J. Appl. Phys., 21, 437-41(1950).

[26]   C. M. Wang, H. M. Chan, M. P. Harmer, and J. M. Rickman , unpublished research.

FIGURE CAPTIONS

Fig.1   SEM micrographs showing the microstructures of the as-hot-pressed Nd-doped aluminas. (a) 100 ppm, (b) 350 ppm, (c) and (d) 1000 ppm, note secondary phase precipitates (arrowed).

Fig.2   SIMS map showing the Nd distribution in the as hot-pressed materials: (a) 100 ppm, (b) 350 ppm, and (c) 1000 ppm.

Fig.3   TEM micrographs of the 350 ppm Nd doped material deformed at temperatures 1200 °C - 1350 °C and a stress of 50 MPa for an accumulated strain of ~ 7%: (a) residual intragranular pores (arrowed); (b) deformation induced cavities within fine grain size regions (black arrows), and at the boundary between coarse and fine grain size clusters (white arrows).

Fig. 4   TEM micrographs show faceting of the residual intragranular pore (arrowed) (a) and dislocation arrays which have a Burgers vector 1/3<11.0> (b).

Fig. 5   Annular aperture dark field STEM image (A) and EDX map of Nd distribution.

Fig. 6   Strain rate as a function of temperature for different Nd dopant levels (50 MPa applied stress).

Fig.7   Apparent activation energy (measured both by creep and sintering experiments) as a function of Nd-doping content.

Fig. 8(a) Strain rate as a function of stress (tested at 1275 °C).

Fig. 8(b) Strain rate as a function of grain size (50 MPa, 1275 °C).

Fig. 9   The grain size distribution of 350 ppm Nd-doped alumina (as-hot-pressed).

Fig. 10   Strain rate as a function of temperature (50 MPa applied stress). For all of the compositions, the data was normalized to a grain size of 2.4 μm according to the measured grain size exponent.

Fig.11   Strain rate as a function of Nd_2O_3 doping level (50 MPa at 1275 °C). All specimens were pre-annealed to achieve a grain size of ~ 2.4 ± 0.2 μm.
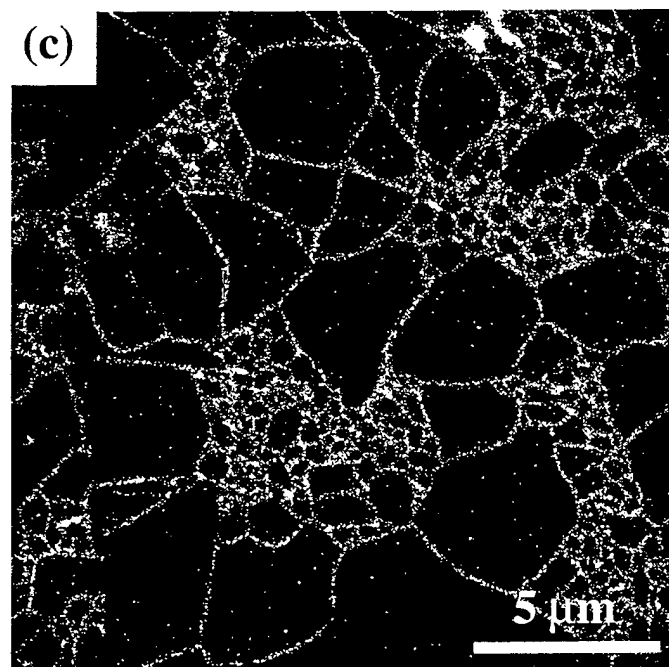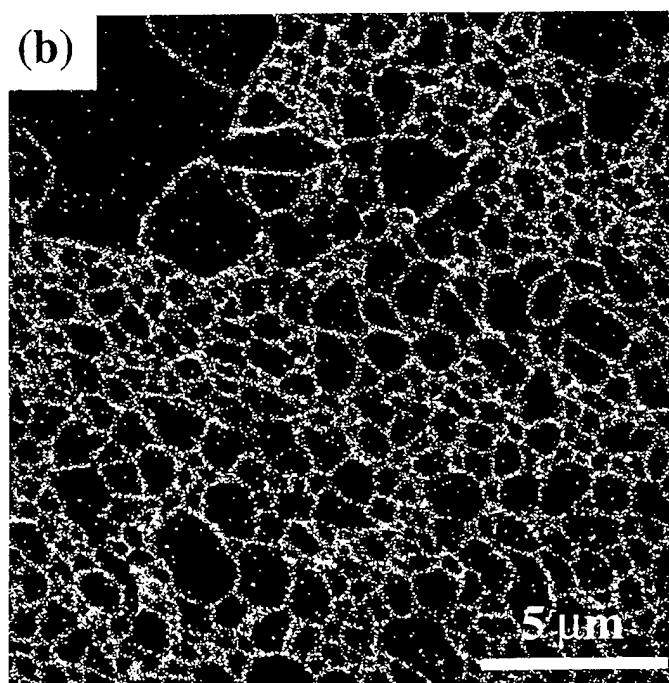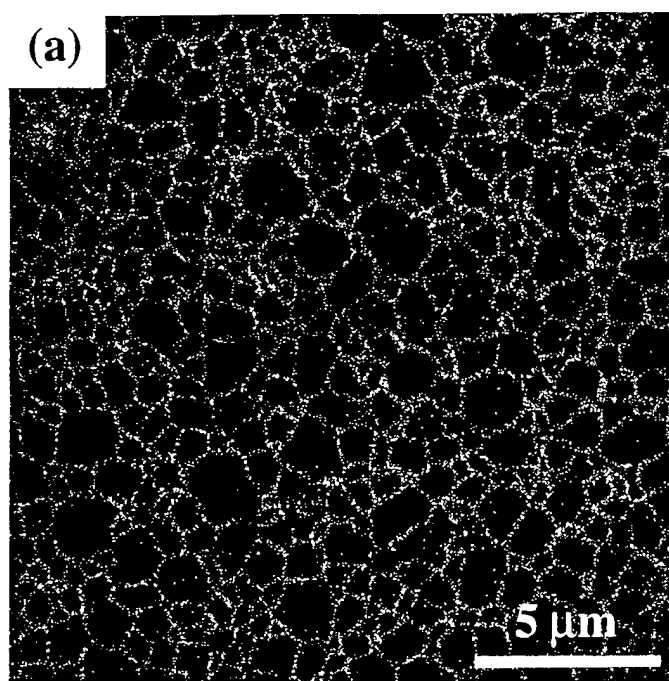
Fig.1

(a)

5 µm

(b)

5 µm

(c)
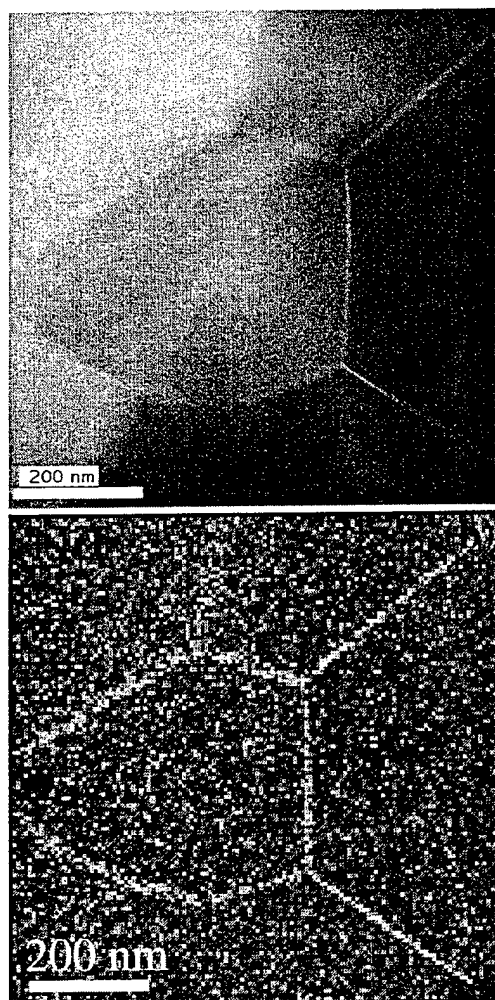
5 µm

Fig.2

(a)

2 μm

(b)
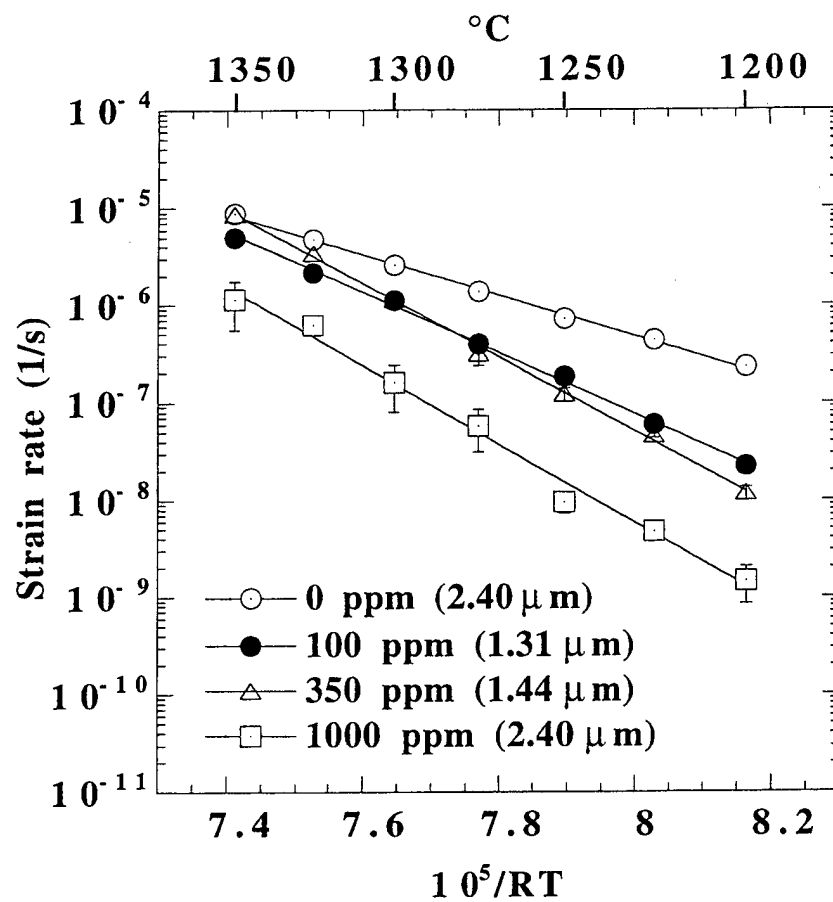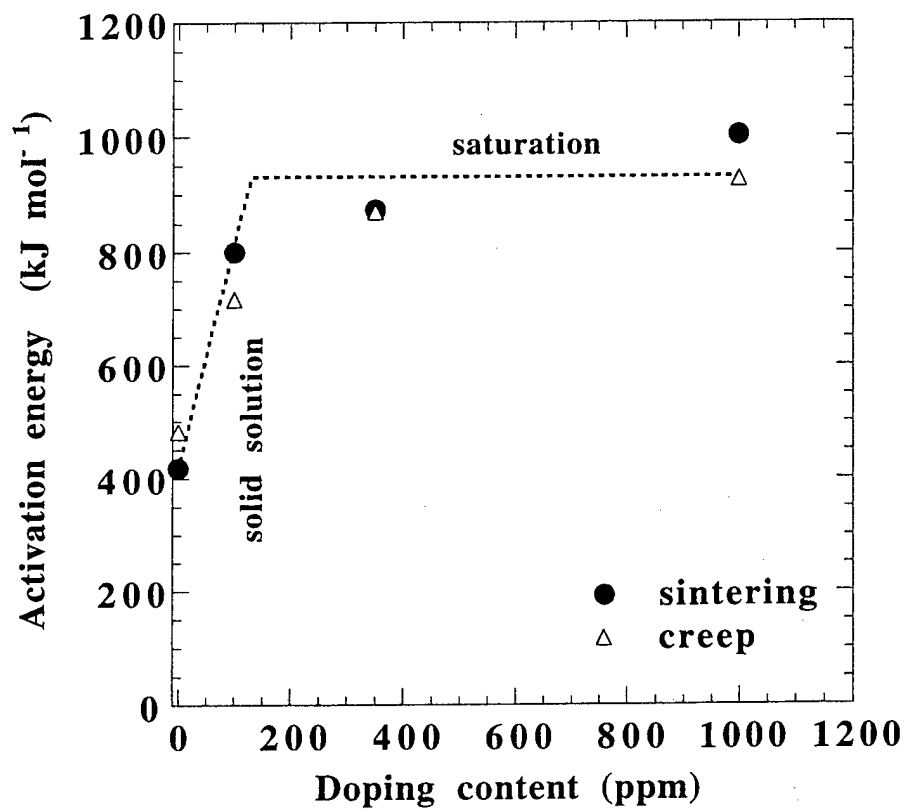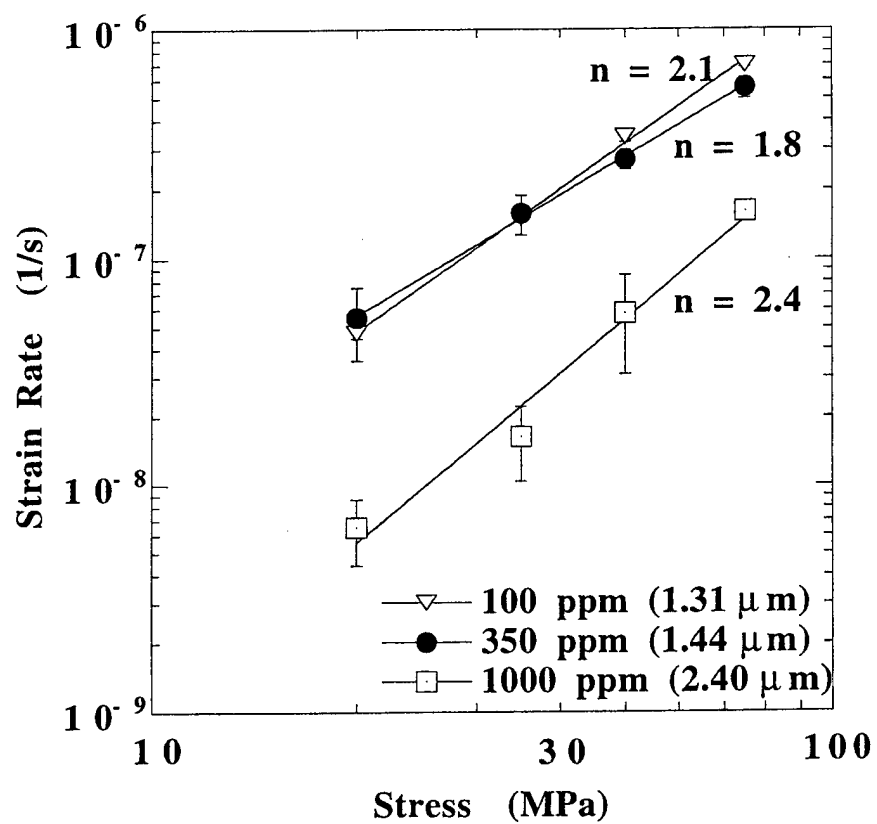
2 μm

Fig.3

(a)

1 μm

(b)

[11$\bar{2}$0]

[1$\bar{2}$10]
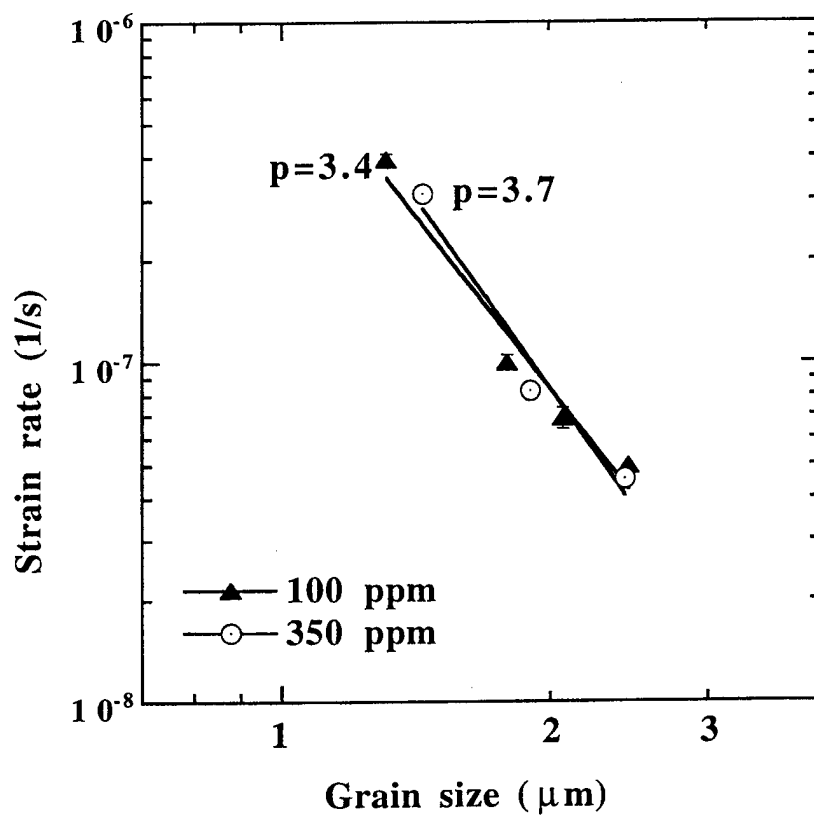
1 μm
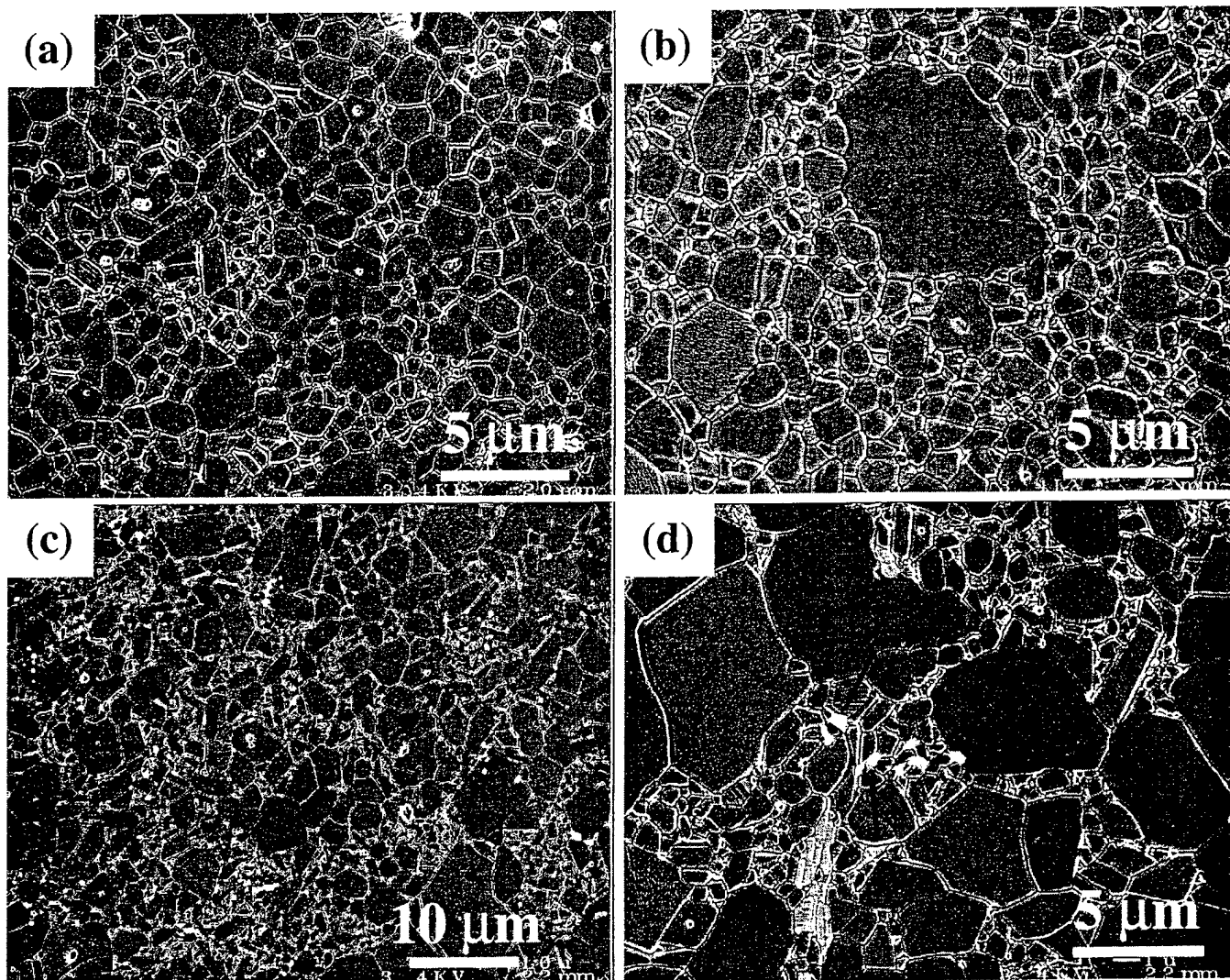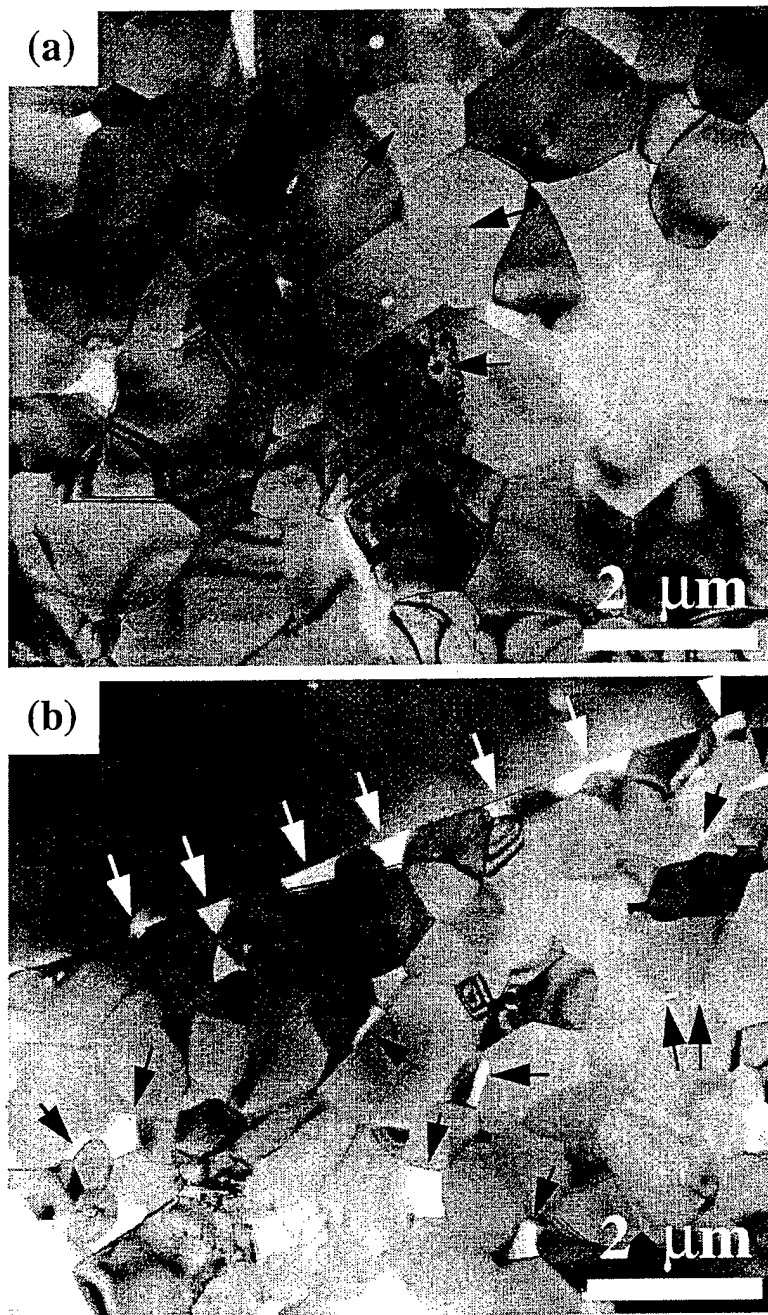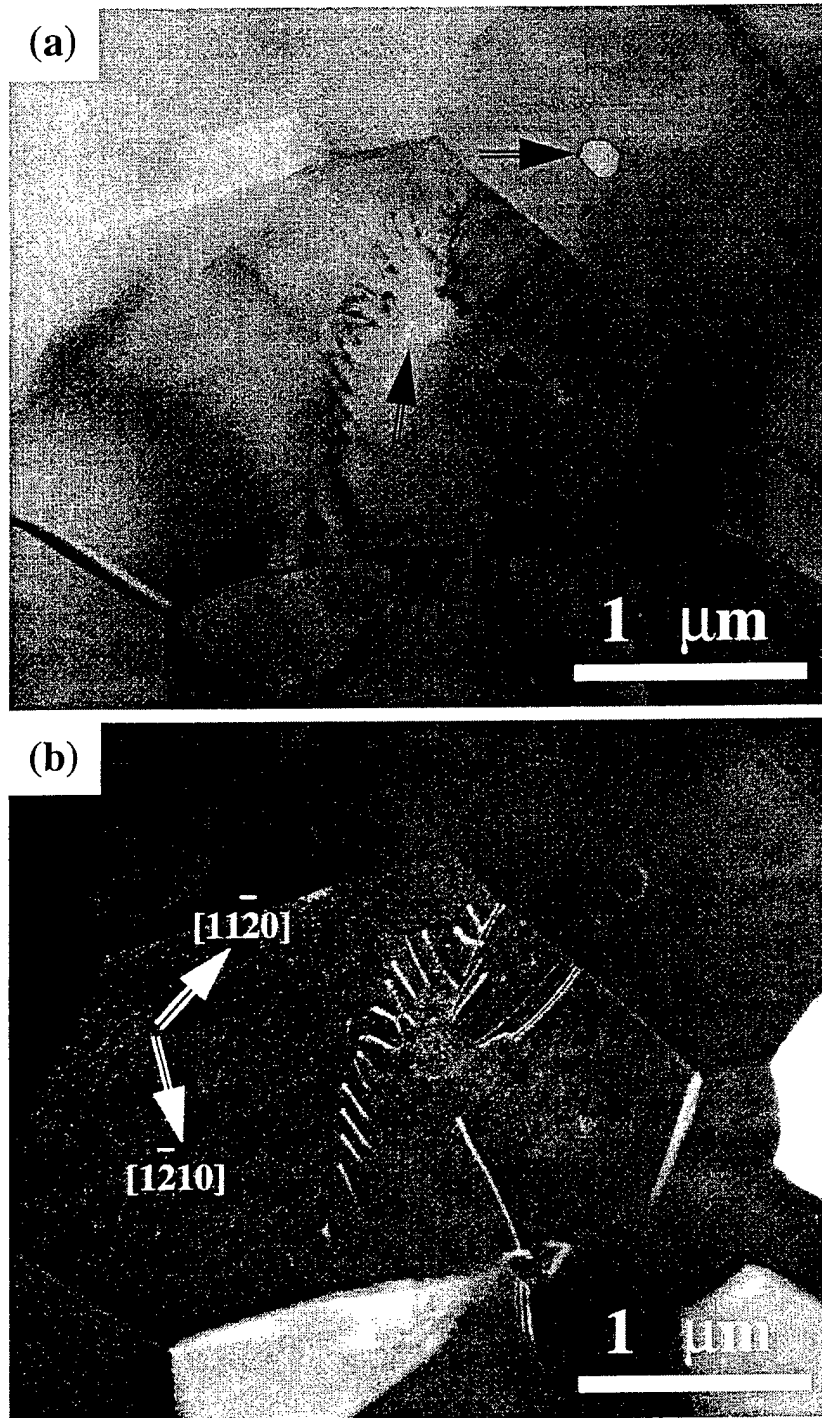
Fig.4

Fig.5

Fig.6

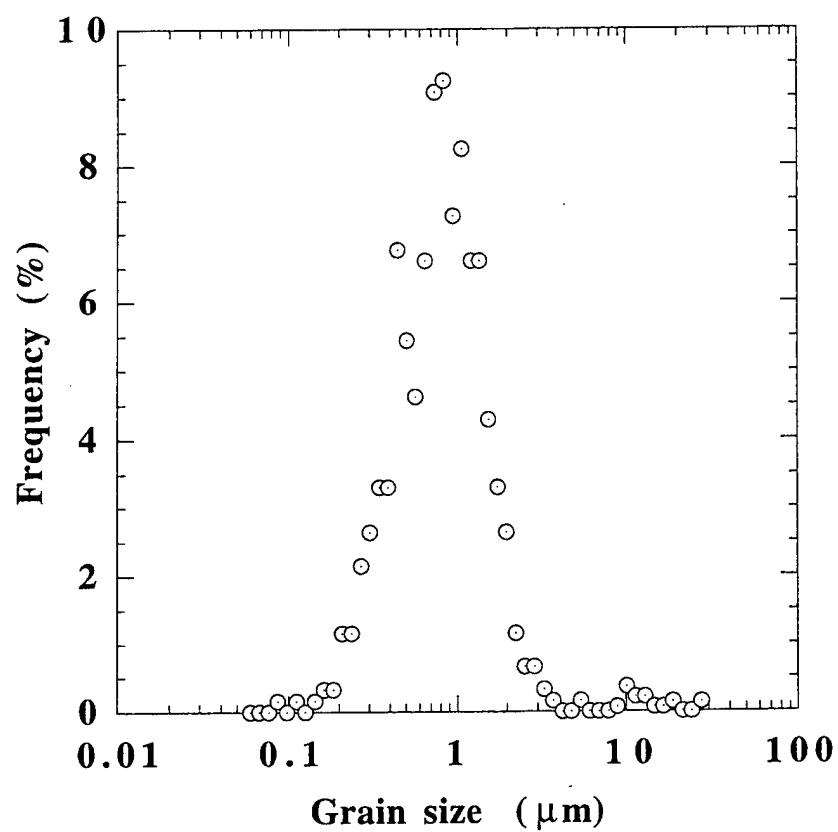Fig.7
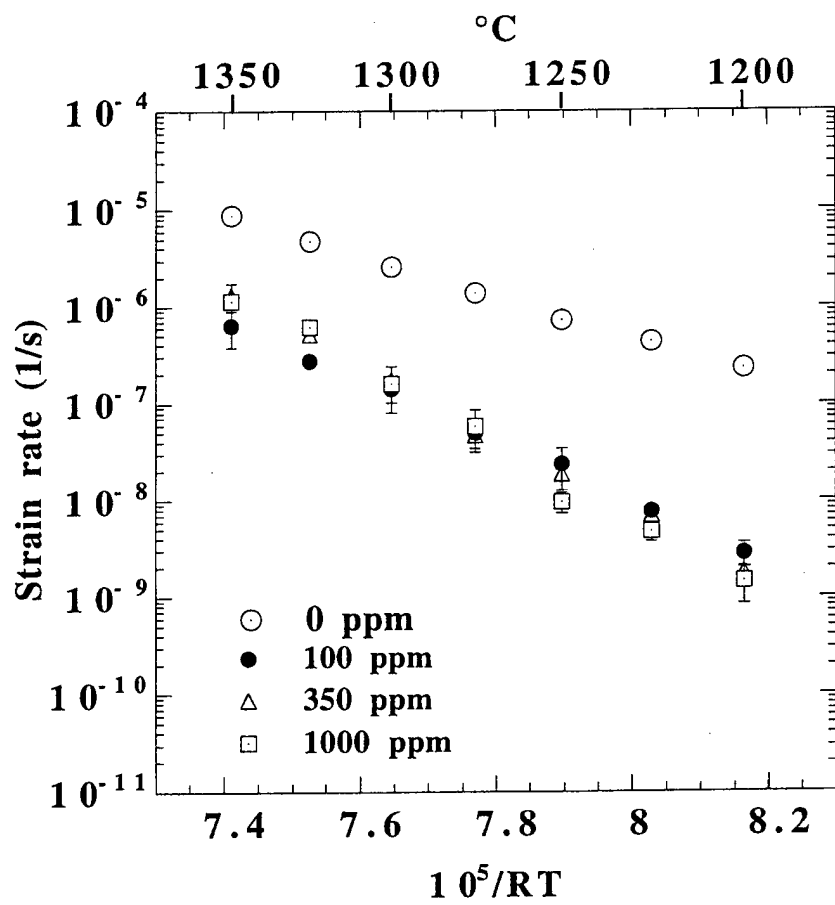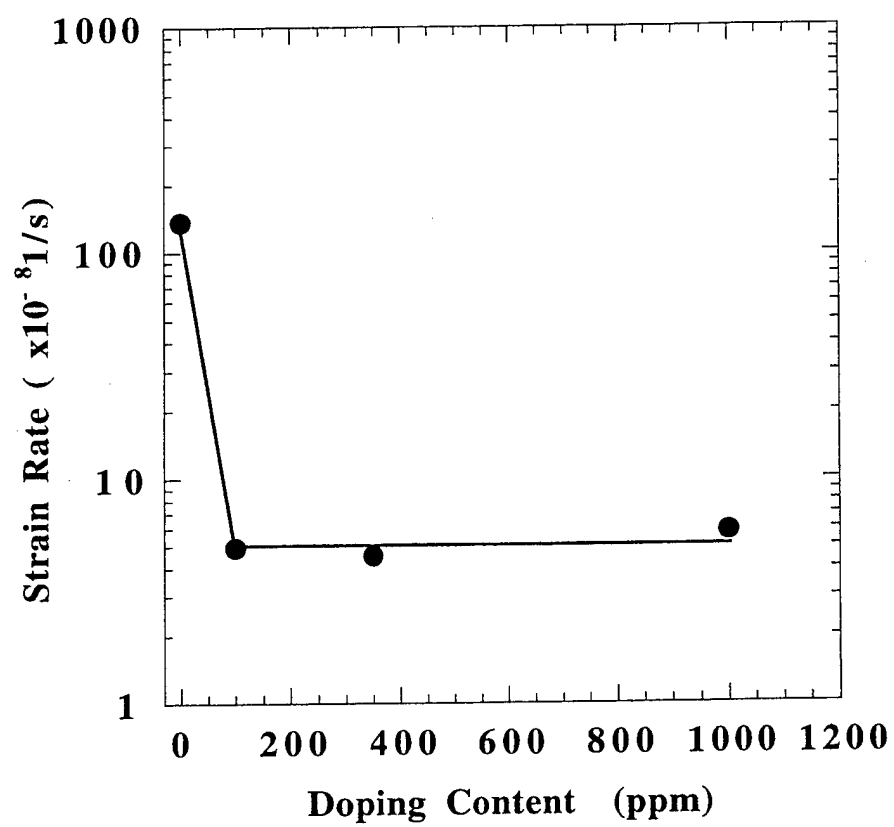
Fig.8(a)

Fig.8(b)

Fig.9

Fig.10

Fig.11

4. PERSONNEL

Faculty:

Prof. Martin P. Harmer, Principal Investigator
Prof. Helen M. Chan, Co-Principal Investigator
Prof. Jeffrey M. Rickman, Co-Principal Investigator

Post-Doctoral Research Associate/Research Engineer:

C. M. Wang
J. Cho

Graduate Students

Michael Drahus

5. PUBLICATIONS

1)   C. M. Wang, G. S. Cargill III, M. P. Harmer, H. M. Chan, and J. Cho, "Atomic Structural Environment of Grain Boundary Segregated Y and Zr in Creep Resistant Alumina from EXAFS," **Acta Mater., 47, 3411-22 (1999).**

2)   C. M. Wang, G. S. Cargill III, H. M. Chan, and M. P. Harmer, "Structural Features of Y-Saturated and Supersaturated Grain Boundaries in Alumina," **Acta Mater., 48, 2579-91 (2000).**

3)   J. Cho, C. M. Wang, H. M. Chan, J. M. Rickman, and M. P. Harmer, "Role of Segregating Dopants on the Improved Creep Resistance of Aluminum Oxide," **Acta Mater., 47, 4197-207 (1999).**

4)   J. Cho, J. M. Rickman, H. M. Chan, and M. P. Harmer, "Modeling of Grain-Boundary Segregation Behavior in Aluminum Oxide," **J. Amer. Ceram. Soc., 83, 344-52 (2000).**

5)   J. Bruley, J. Cho, H. M. Chan, M. P. Harmer, and J. M. Rickman, "STEM Analysis of Grain Boundaries in Creep Resistant Y- and La-Doped Alumina Microstructure," **J. Amer. Ceram. Soc., 82, 2865-70 (1999).**

6)   C. M. Wang, G. S. Cargill III, H. M. Chan, and M. P. Harmer, "Structure of Y and Zr Segregated Grain Boundaries in Alumina," **Interface Sci., 8, 243-55 (2000).**

7)   C. M. Wang, J. Cho, H. M. Chan, M. P. Harmer, and J. M. Rickman, "Influence of Dopant Concentration on Creep Properties of Nd_2O_3 Doped Alumina," **J. Amer. Ceram. Soc., in press.**

6. INTERACTIONS/TRANSITIONS

PRESENTATIONS

1) M. P. Harmer, "Controlled Abnormal Grain Growth for Solid State Crystal Conversion," invited presentation on Solid State Studies in Ceramics Gordon Research Conference, Meriden, NH 2000.

2) C. M. Wang, H. M. Chan, M. P. Harmer, J. M. Rickman, and G. S. Cargill III, "Dopant Grain Boundary Segregation Behavior and Atomic Structural Environment around the Dopant," presentation on Solid State Studies in Ceramics Gordon Research Conference, Meriden, NH 2000.

3) C. M. Wang, H. M. Chan, M. P. Harmer, and J. M. Rickman, "Creep Behavior of Y/Fe Codoped Alumina," Presented at the 102nd annual meeting of the American Ceramic Society, Paper Number: BS-029-00, St. Louis, Missouri, April 30 - May 3, 2000.

4) M. P. Harmer, H. M. Chan, J. M. Rickman, and C. M. Wang, "Grain Boundary Chemistry and Creep Resistance of Alumina," Presented at the annual review meeting of the Air Force Office of Scientific Research, St. Louis, Missouri, April 30-May 3, 2000.

5) C. M. Wang, H. M. Chan, M. P. Harmer, J. M. Rickman, and G. S. Cargill III, "Dopant Grain Boundary Supersaturation and Creep Resistance in Y- and Zr-Doped Alumina," Presented at the 102nd annual meeting of the American Ceramic Society, Paper Number: BS5P-002-00, St. Louis, Missouri, April 30 - May 3, 2000.

6) J. M. Rickman, "Coarse-Grained Free Energy for a Lennard-Jones System," Presented at the Spring APS meeting, 2000.

7) J. M. Rickman, "Stress Measures in Defected System," Presented at the Spring SIAM meeting, 2000.

INDUSTRIAL APPLICATIONS

Based on the Lehigh group's research on doped alumina creep properties, the doping strategy has been adopted by 3M company in improving the creep resistance of alumina fiber. A new type of creep resistant alumina fiber doped with Y and Zr is currently marketed by 3M.

7. HONORS/AWARDS

C. M. Wang, H. M. Chan, J. M. Rickman, M. P. Harmer, and G. S. Cargill III received the **1ˢᵗ Place Award of American Ceramic Society** for **Ceramographic Competition** of the 101ˢᵗ annual meeting. The poster is entitled "Structural Features of Y Saturated and Supersaturated Grain Boundaries in α-Al_2O_3"

Helen M. Chan was awarded the New Jersey Zinc Professorship at Lehigh University

Jeffrey M. Rickman was awarded the Class of '61 Professorship at Lehigh University